

ACTA MATERIALIA TRANSYLVANICA

ANYAGTUDOMÁNYI KÖZLEMÉNYEK



2. ÉVF.
2019. 2.

ACTA MATERIALIA TRANSYLVANICA

Anyagtudományi Közlemények

2. évfolyam, 2019. 2. szám



ERDÉLYI MÚZEUM-EGYESÜLET
Kolozsvár
2019

A folyóirat megjelenését támogatta a Magyar Tudományos Akadémia, a Bethlen Gábor Alapkezelő Zrt. és az EME Műszaki Tudományok Szakosztálya / The publication of this magazine was supported by the Hungarian Academy of Sciences, by the Bethlen Gábor Fund and by the TMS – Department of Engineering Sciences



Főszerkesztő / Editor-in-Chief: Bitay Enikő

Nemzetközi Tanácsadó testület / International Editorial Advisory Board:

Prof. Biró László Péter, MTA Energiatudományi Kutatóközpont, Budapest, Magyarország
 Prof. emer. B. Nagy János, University of Namur, Namur, Belgium
 Prof. Czifágy Tibor, Budapesti Műszaki és Gazdaságtudományi Egyetem, Budapest, Magyarország
 Prof. Diószegi Attila, Jönköping University, Jönköping, Svédország
 Dobránszky János, MTA–BME Kompozittechnológiai Kutatócsoport, Budapest, Magyarország
 Prof. Dusza János, Institute of Materials Research of Slovak Academy of Sciences, Kassa, Szlovákia
 Prof. Gyenge Csaba, Technical University of Cluj-Napoca, Kolozsvár, Románia
 Prof. emer. Gyulai József, Budapesti Műszaki és Gazdaságtudományi Egyetem, Budapest, Magyarország
 Prof. Kaptay György, Miskolci Egyetem, Miskolc, Magyarország
 Dr. Kolozsváry Zoltán, Plasmaterm Rt., Marosvásárhely, Románia
 Prof. Mertinger Valéria, Miskolci Egyetem, Miskolc, Magyarország
 Prof. Porkoláb Miklós, Massachusetts Institute of Technology, Cambridge, MA, USA
 Prof. Réger Mihály, Óbudai Egyetem, Budapest, Magyarország
 Prof. emer. Réti Tamás, Óbudai Egyetem, Budapest, Magyarország
 Prof. emer. Roósz András, Miskolci Egyetem, Miskolc, Magyarország
 Dr. Spenik Sándor, Ungvári Nemzeti Egyetem, Ungvár, Ukrajna
 Prof. Zsoldos Ibolya, Széchenyi István Egyetem, Győr, Magyarország

Lapszámszerkesztők / Editorial Board:

Dobránszky János, MTA–BME Kompozittechnológiai Kutatócsoport, Budapest, Magyarország
 Csavdári Alexandra, Babeş–Bolyai Tudományegyetem, Kolozsvár, Románia
 Gergely Attila, Sapientia Erdélyi Magyar Tudományegyetem, Marosvásárhely, Románia
 Kovács Tünde, Óbudai Egyetem, Budapest, Magyarország

Kiadó / Publisher: Erdélyi Múzeum-Egyesület

Felélős kiadó / Responsible publisher: Biró Annamária

Olvasószerkesztő / Proofreader: Szenkovic Enikő (magyar), David Speight (English)

Műszaki szerkesztő / DTP: Szilágyi Júlia

Szerkesztőségi titkár / Editorial secretary: Kisfaludi-Bak Zsombor

Borítótér / Cover: Kőnczey Elemér

Nyomdai munkálatok / Printed at: F&F International kft., Gyergyószentmiklós

Copyright © a szerzők / the authors, EME/ TMS 2019

ISSN 2601-1883, ISSN-L 2601-1883

DOI: 10.33924/amt-2019-02

Online elérhető / online available at: <https://eda.eme.ro/handle/10598/30356>

A folyóirat honlapja: <https://www.eme.ro/publication-hu/acta-mat/mat-main.htm>

The journal website: <https://www.eme.ro/publication/acta-mat/mat-main.htm>

Acta Materialia Transylvanica. Anyagtudományi Közlemények az Erdélyi Múzeum-Egyesület (EME) Műszaki Tudományok Szakosztályának folyóirata, amely az anyagtudományok területéről közöl tudományos közleményeket: szakcikkeket, összefoglalókat (szemléket), tanulmányokat. A folyóirat célja összképet adni kiemelten a Kárpát-medencei kutatási irányokról, tudományos eredményeiről, s ezt széles körben terjeszteni is. A folyóirat az EME felváltalt céljaihoz híven a magyar szaknyelv ápolását is támogatja, így a nyomtatott folyóirat magyar nyelven jelenik meg, mely az Erdélyi digitális adattárban elérhető (<https://eda.eme.ro/handle/10598/30356>). A széles körű nemzetközi terjesztés érdekében a folyóirat teljes angol nyelvű változatát is közzétesszük.

Acta Materialia Transylvanica – Material Sciences Publications – is a journal of the Technical Sciences Department of the Transylvanian Museum Society, publishing scientific papers, issues, reviews and studies in the field of material sciences. Its mission is to provide and disseminate a comprehensive picture focusing on research trends and scientific results in the Carpathian basin. In accordance with the general mission of the Transylvanian Museum Society it aims to support specialized literature in Hungarian. The printed version of the journal is published in Hungarian and is available in the Transylvanian Digital Database (<https://eda.eme.ro/handle/10598/30356>). However, we would like to spread it internationally, therefore the full content of the journal will also be available in English.

Tartalom / Content

BIRÓ László Péter, KERTÉSZ Krisztián, PISZTER Gábor, HORVÁTH Zsolt Endre, BÁLINT Zsolt	69
<i>Anyagtudósok kalandozása a biológiában: A lepkék szárnyainak szerkezeti színei</i>	
<i>Roaming of Materials Scientists in Biology: Structural Colours of Butterfly Wings</i>	
ASZTALOS Lilla, HORICSÁNYI Krisztina	73
<i>Hatóanyag-kibocsátó koszorúérsztentek bevonatának vizsgálata</i>	
<i>Examination of Coating of Drug-Eluting Coronary Stents</i>	
BITAY Enikő, MÁRTON László, TALPAS János	79
<i>A csikmadarasi vasgyártásból visszamaradt leletek anyagszerkezeti vizsgálata</i>	
<i>Microstructural Characterisation of Archeologic Finds Discovered at the Ironworks in Mádárás</i>	
FÁBIÁN Enikő Réka, TÓTH László, HUSZÁK Csenge	87
<i>A hőkezelés hatása a szerszámacélok szövetszerkezetére és kopási viselkedésére</i>	
<i>Examination of Heat Treatment on the Microstructure and Wear of Tool Steels</i>	
HALÁSZ Gergely, FÁBIÁN Enikő Réka, KUTI János	93
<i>Auszténites korrózióálló acélok lézersugaras vágása</i>	
<i>Laser Cutting of Austenitic Corrosion-Resisting Steels</i>	
HORVÁTH Richárd, STADLER Róbert Gábor, ANDRÁSFALVY Kristóf	99
<i>Szénszállal erősített műanyag marásának vizsgálata</i>	
<i>Investigation of Milling of Carbon Fiber Reinforced Plastic</i>	
KOVÁCS Tünde Anna, NYIKES Zoltán, FIGULI Lucia	105
<i>Kompozit anyag fejlesztése dinamikus igénybevételre</i>	
<i>Development of a Composite Material for Impact Load</i>	
LEVELES Borbála, KEMÉNY Alexandra, KATONA Bálint	110
<i>Edzett üveg dinamikus és nagy hőmérsékletű, kvázisztatikus vizsgálata</i>	
<i>Dynamic and high temperature quasi-static examination of tempered glass</i>	

MESZLÉNYI György, BITAY Enikő	115
<i>A fókuszált lézernyaláb keresztmetszeti jellemzőinek szerepe az impulzusos üzemű lézeres vágásnál</i>	
<i>Role of the Features of Focused Laser Beam in Pulsed Laser Cutting</i>	
UZONYI Sándor.....	121
<i>Additív gyártás alkalmazása a kovácsszerszám-javításban</i>	
<i>Application of Additive Manufacturing for the Repair of Forging Dies</i>	

Roaming of Materials Scientists in Biology: Structural Colours of Butterfly Wings

László P. BIRÓ¹, Krisztián KERTÉSZ¹, Gábor PISZTER¹, Zsolt E. HORVÁTH¹, Zsolt BÁLINT²

¹ *Institute of Technical Physics and Materials Science, Centre for Energy Research, Hungarian Academy of Sciences, Budapest, Hungary, biro.laszlo@energia.mta.hu*

² *Hungarian Natural History Museum, Budapest, Hungary, balint.zsolt@nhmus.hu*

Abstract

The photonic nanoarchitectures occurring in the wing scales of Lycaenid butterflies were investigated by scanning electron microscopy (SEM), transmission electron microscopy (TEM) and UV-VIS spectroscopy. We found that the males of all the nine investigated species possess photonic nanoarchitectures built according to the same general “plan”, but each species exhibits species-specific features which results in species-specific colours reproduced generation by generation with a high degree of accuracy.

Keywords: *butterfly wing scales, photonic nanoarchitecture, electron microscopy, UV-Vis spectroscopy.*

1. Introduction to photonic nanoarchitectures

1.1. As seen from physics

Physics discovered about thirty years ago that it is possible for light waves to produce forbidden bands as is well-known for semiconductors [1, 2]. To achieve this, we have to produce a composite from two transparent media with sufficiently different refractive indexes, in such a way that the local value of the refractive index changes in a periodic way in space, and on a scale comparable with the wavelength of the radiation that is not able to propagate in the composite. This last condition dictates that in the case of visible light, the composite in fact has to be a nanocomposite, in other words the changing of the refractive index takes place, on scale of the order of 100 nm. If taken strictly the above conditions define a photonic crystal, in which the light falling within the forbidden gap will not be able to propagate in any direction, therefore it will be reflected from the surface of the photonic crystal. If we relax the condition of a perfectly ordered structure, the photonic band gap will still be present, its spectral position will be also conserved, its width decrease and the complete band gap may transform into a partial band gap [3].

1.2. As seen from biology

Around 50 million years ago, biological evolution gave rise to the possibilities of photonic nanoarchitectures [4]. Since then various organisms have used this colour generation method to accomplish various biological functions. The most well-known examples can be found between beetles and butterflies [5]. In the case of butterflies, the blue and green colours are of structural origins, in other words they originate from photonic nanoarchitectures. The blue colour and its various shades are particularly well suited, for example, in front of a green background to make coloured objects conspicuous [6]. The males of the Lycaenid butterflies living in such types of habitat have their dorsal colours in various hues of blue, while the dorsal colour of the females is pigment (melanin) generated brown. This allows the wings of the females to absorb heat from solar radiation in a more efficient way [7], which is very useful for the development of their eggs.

1.3. As seen from materials science

As we examine the nanoarchitectures generating structural (physical) colour, the first factor we have to emphasize is the sufficient contrast in the magnitude of refractive index between the two transparent media. The larger this contrast,

the easier it is to produce the photonic band gap, if the two components alternate with each other with an adequate periodicity. For butterflies – the insects in the focus of this paper – the two components are chitin $n_1 = 1.56$ and air $n_2 = 1$. Chitin is a biopolymer, a polysaccharide, with a chemical formula and properties very close to cellulose, the material used for paper manufacturing.

From the discussion above it follows that chitin and air have to be “mixed” with each other on a 100 nm scale if we want the resulting nanocomposite to generate colour.

Of course, this mixing can be carried out in various ways: a) resulting in a length scale much larger than 100 nm in a perfectly periodic mixing, which is called a photonic crystal [8]; b) a photonic polycrystal built of micron sized grains, each of which individually constitutes a photonic crystal [8]; c) a so-called photonic amorphous, which exhibits only a short range order between its building elements, for example in the distance of the first neighbours [9]. This last case is presented in Figure 1.

One may well note in Figure 1. that the scales are arranged in regular rows, resembling the arrangement of the tiles on a roof. Their characteristic size is $100 \times 50 \mu\text{m}^2$, their shape is like a flattened sac with a thickness of $1 \mu\text{m}$. This is the volume which is filled by the photonic nanoarchitecture.



Figure 1. Photograph of the dorsal wing surface of a male *Polyommatus icarus* (left); scanning electron microscopy image of the scales on the wing membrane (right upper); scanning electron micrograph of the nanoarchitecture filling the volume of the blue coloured scale (right lower).

2. Sexual signalling colour

Between the Lycaenids and especially between the Blues, sexual dimorphism, when the male and the female have very different appearance, is very frequent. The dorsal wing surface of the males usually has a blue colouration, which can be attributed to structural colour (Figure 2. [6]), while the dorsal wing surface of the females is brown coloured, due to the presence of melanin. The ventral wing surfaces of both sexes have an identical complex pattern of dots generated by pigment coloured scales. The pattern is species-characteristic, but there are many similarities between the patterns of different species.

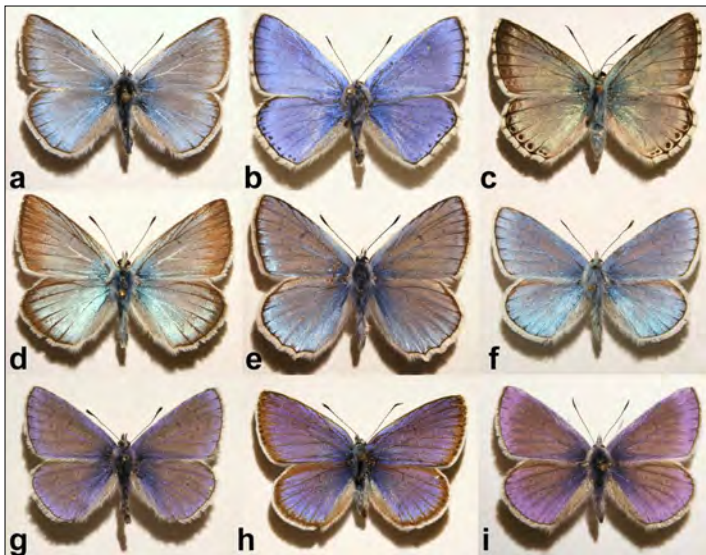


Figure 2. Males of nine closely related Lycaenid species, living in the same habitat. Photographs taken under artificial illumination. a) *Polyommatus amandus*; b) *Polyommatus bellargus*; c) *Polyommatus coridon*; d) *Polyommatus damon*; e) *Polyommatus daphnis*; f) *Polyommatus dorylas*; g) *Polyommatus icarus*; h) *Polyommatus semiargus*; i) *Polyommatus thersites*.

3. The nanoarchitectures generating the colours

The species-specific sexual signaling colours are generated by nanoarchitectures built according to the same “ground plan”, but which have enough species-specific characteristics to generate specific colours. Due to their characteristic sizes the structural details of these nanoarchitectures can be revealed only by electron microscopic methods (Figure 3). The surface structure of individual scales is revealed by scanning electron microscopy (SEM), while the cross-sectional details of the scale structure can be revealed by transmission electron microscopy (TEM) (Figure 4). To be able to use this last method, one has to incorporate the pieces of wings in special resin and to cut slices of 70 nm thickness with a diamond ultramicrotome knife.

The TEM images (Figure 4) show that all the nanostructures are built from the alternation of chitin (dark in the TEM) and air regions (light in the TEM). The differences are found in the number of layers and in the order/disorder characterizing the individual layers. In the interpretation of the TEM images one has to keep in mind that the images are taken from slices only 70 nm thick. Therefore, features exceeding this size may not be completely present in the image.

One may well observe in the SEM images (Figure 3) that all the scales have similar structural features: all have a system of longitudinal ridges interlinked by cross-ribs, and below the network of these, one finds a perforated layer.

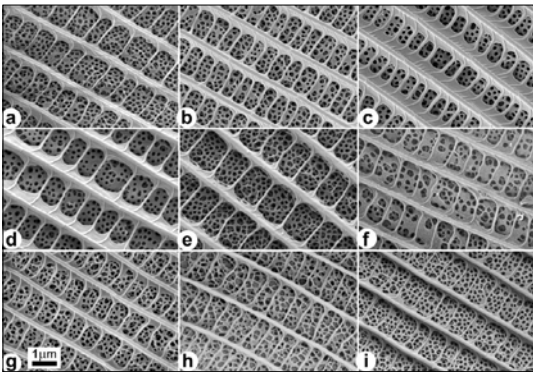


Figure 3. SEM micrographs of the scale surface of the males of the nine butterfly species presented in Figure 2. a) *Polyommatus amandus*; b) *Polyommatus bellargus*; c) *Polyommatus coridon*; d) *Polyommatus damon*; e) *Polyommatus daphnis*; f) *Polyommatus dorylas*; g) *Polyommatus icarus*; h) *Polyommatus semiargus*; i) *Polyommatus thersites*. The scale bar given in the micrograph in the lower left corner is valid for all the micrographs.

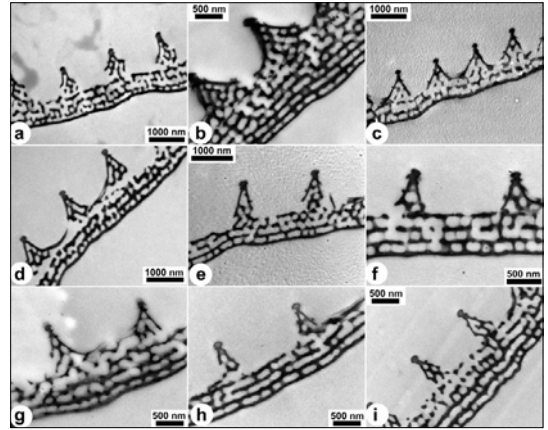


Figure 4. TEM micrographs of the cross-sectional scale structure for the males of the nine butterfly species presented in Figure 2. Dark regions correspond to chitin, while the light areas represent voids filled with air. a) *Polyommatus amandus*; b) *Polyommatus bellargus*; c) *Polyommatus coridon*; d) *Polyommatus damon*; e) *Polyommatus daphnis*; f) *Polyommatus dorylas*; g) *Polyommatus icarus*; h) *Polyommatus semiargus*; i) *Polyommatus thersites*.

4. Spectral characterization of the colours

To characterize the light reflected by the wing of the investigated butterflies we used a modular fiber optic spectrophotometer. The results are shown in Figure 5.

It can be observed in Figure 5. that all the spectra have distinct characteristic features. Because of this an artificial neural network based software is able to identify the butterfly species on the basis of the wing reflectance of the males with an accuracy of 96% [6].

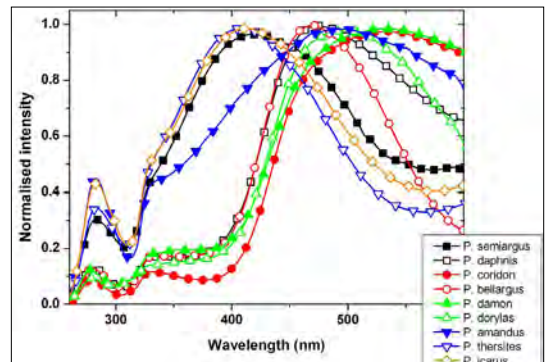


Figure 5. Reflectance of the dorsal wing surface of the males of the nine investigated butterfly species. To facilitate the comparison of the spectra all curves have been normalized to 1

5. Conclusions

We have shown that the blue and green colours of butterflies are of structural origin. These colours are generated by nanocomposites built from the spatially periodic arrangement of two transparent materials with different refractive indexes: chitin and air, which generate a photonic band gap. The photonic nanoarchitecture is found in the volume of the wing scales. The scales cover the wing membrane in a regular arrangement.

The colours generated in this way are species specific and play an important role in sexual communication. Because of this they are reproduced with a high degree of precision from generation to generation [10].

Acknowledgment

The work was supported by OTKA grants 111741 and 115724.

References

- [1] Yablonoitch E.: *Inhibited Spontaneous Emission in Solid-State Physics and Electronics*. Physical Review Letters, 58. (1987) 2059–2062. <https://doi.org/10.1103/PhysRevLett.58.2059>
- [2] John S.: *Strong localization of photons in certain disordered dielectric superlattices*. Physical Review Letters, 58. (1987) 2486–2489. <https://doi.org/10.1103/PhysRevLett.58.2486>
- [3] Edagawa K., Kanoko S., Notomi M.: *Photonic Amorphous Diamond Structure with a 3D Photonic Band Gap*. Physical Review Letters, 100. (2008) 013901. <http://doi.org/10.1103/PhysRevLett.100.013901>
- [4] McNamara M. E., Briggs D. E. G., Orr J. P., Wedmann S., Noh H., Cao H.: *Fossilized Biophotonic Nanostructures Reveal the Original Colors of 47-Million-Year-Old Moths*. PLoS Biology, 9. (2011) e1001200. <https://doi.org/10.1371/journal.pbio.1001200>
- [5] Biró L. P., Vigneron J. P.: *Photonic nanoarchitectures in butterflies and beetles: valuable sources for bioinspiration*. Laser and Photonic Review, 5. (2011) 27–51. <https://doi.org/10.1002/lpor.200900018>
- [6] Bálint Z., Kertész K., Piszter G., Vértesy Z., Biró L. P.: *The well-tuned blues: the role of structural colours as optical signals in the species recognition of a local butterfly fauna (Lepidoptera: Lycaenidae: Polyommatainae)*. Journal of the Royal Society. Interface, 9. (2012) 1745–1756. <https://doi.org/10.1098/rsif.2011.0854>
- [7] Biró L. P., Bálint Zs., Kertész K., Vértesy Z., Márk G. I., Horváth Z. E., Balázs J., Méhn D., Kiricsi I., Lousse V., Vigneron J.-P.: *Role of photonic-crystal-type structures in the thermal regulation of a Lycaenid butterfly sister species pair*. Physical Review E, 67. (2003) 021907. <https://doi.org/10.1103/PhysRevE.67.021907>
- [8] Kertész K., Bálint Z., Vértesy Z., Márk G. I., Lousse V., Vigneron J.-P., Rassart M., Biró L. P.: *Gleaming and dull surface textures from photonic-crystal-type nanostructures in the butterfly Cyanophrys remus*. Physical Review E, 74. (2006) 021922-1–021922-15. <https://doi.org/10.1103/PhysRevE.74.021922>
- [9] Kertész K., Molnár G., Vértesy Z., Kóos A. A., Horváth Z. E., Márk G. I., Tapasztó L., Bálint Zs., Tamáska I., Deparis O., Vigneron J.-P., Biró L. P.: *Photonic band gap materials in butterfly scales: A possible source of “blueprints”*. Materials Science and Engineering B, 149. (2008) 259–265. <https://doi.org/10.1016/j.mseb.2007.10.013>
- [10] Kertész K., Piszter G., Bálint Z., Biró L. P.: *Biogeographical patterns in the structural blue of male Polyommatus icarus butterflies*. Scientific Reports, 9. (2019) 2338. <https://doi.org/10.1038/s41598-019-38827-w>

Examination of Drug-eluting Coatings of Coronary Artery Stents

Lilla ASZTALOS¹, Krisztina HORICSÁNYI²

¹ *Budapest University of Technology and Economy, Faculty of Mechanical Engineering, Department of Materials Science & Engineering, Budapest, Hungary, lilla@eik.bme.hu*

² *Budapest University of Technology and Economy, Faculty of Mechanical Engineering, Department of Mechatronics, Optics and Mechanical Engineering Informatics Budapest, Hungary, horicsanyi.krisztina@gmail.com*

Abstract

Drug-eluting stents provide a solution for treating restenosis in arteries expanded by using conventional bare metal stents, but there are a small number of publications on the processes of coating damage established due to the various effects that occur during the life cycle of the stent. In the current research damage to the coating was investigated along with the effects of damage on the corrosion resistance of the stent in multiple ways. This research investigates not only traditional drug eluting stents with polymer matrix, but also the new generation of polymer-free types.

Keywords: *coronary stent, drug eluting stent, coating, corrosion.*

1. Drug Eluting Stents

At the beginning of the 2000's the so-called drug eluting stents (DES) were introduced, and were used to reduce neointimal proliferation – the primary cause of in-stent-restinosis – to 5-10%. While optimizing the architecture and mechanical properties of bare metal stents (BMS) has also led to a reduction in restenosis, the use of drug eluting stents has not been neglected [1].

Techniques for applying the active agent to the stent surface can be divided into three groups: (a) applying the active agent directly to the metal surface, (b) applying the active agent to the surface pores of the metal stent, (c) bonding the active agent to a polymer and bringing the polymer-drug mixture on the implant surface [1, 2]. Not only can there be a coating on the surface of the stents which releases the drug, but there are also non-drug coated stents. The firsts are called active stents, the seconds are called passive coatings [3]. The main advantage of passive stent coatings is that they make the metal device “invisible” to the surrounding tissue. Passive coatings should ensure optimal interaction with blood and arterial wall [4]. Method (c) is the most widely used coat-

ing technique today, however, in order to eliminate longterm problems due to nondegradable polymers and slow drug dissolution, drug-free stents produced by method (a) are appearing in more and more manufacturers [5].

The main requirements for stent coatings are proper adhesion and release, but also the basic material of the carrier polymer itself, the quality of the coating surface, etc. are important. Previous research at the Department of Materials Science and Engineering of the Budapest University of Technology and Economics has dealt with studying commercially available coated stents and the development of polyurethane based coatings [6, 7]. Over the years, coating-specific research has introduced a number of previously untested types of coating, as well as types with biodegradable polymers and the already mentioned polymer free types [8, 9]. In our previous research, we investigated the coating damage of platinum-chromium-alloyed steel stents containing polyvinylidene fluoride-cohexafluoropropylene (hereinafter PVDF-HFP) containing the active compound everolimus [10], however, a wider variety of base materials and coating types are observed

in our current study. Corrosion measurements were also performed on coronary stents [11], and the Department of General and Physical Chemistry at the University of Pécs has supported us in rethinking and evaluating the measurements.

2. Our research

2.1. Examination of coating failures

The coating of drug eluting stents is examined using an electron microscope. So far, however, for scanning electron microscopic examination, the stents have to be fixed to the sample holder with a special double-sided adhesive tape. The problem with the method is that we have to take out the stent from the microscope chamber, remove it from the adhesive tape, and then fix it again after moving it, if we want to change the position of the sample. This process is time-consuming due to vacuuming and the adhesive tape can damage the coating each time the stent is removed.

To overcome this problem, we have developed a clamping and moving device that allows the stent to be rotated without opening the chamber so that the coating of the stent can be examined along its mantle. A prototype was prepared from the designed device (Figure 1). The stent rotator was designed for the chamber of the Zeiss EVO MA 10 type electron microscope on the Department of Materials Science and Engineering of the Budapest University of Technology and Economics. The prototype device fits into the chamber of the electron microscope (Figure 2), the stepper motor for axis movement is mounted on an Arduino free software open source electronics development platform, with a Raspberry Pi programmed single card computer, and this system can be controlled via WiFi, and the network control can function even if the chamber is closed and vacuumed. The development goals of the prototype device include further size reduction and the design of a housing for the electronic components.

In addition to the previously studied PVDF-HFP-coated, platinum-chromium-alloyed steel stents, we also investigated amorphous silicon-carbide-coated, cobalt-chromium-alloyed steel stents, as well as drug-release coated stents without polymeric binding layer.

The amorphous silicon carbide coating, like the PVDF-HFP coating, was broken at several sites already after the expansion in water, the damages was located typically in the curved sections of the struts (Figure 3). Compared to the two coating types, the PVDF-HFP coating was less damaged.

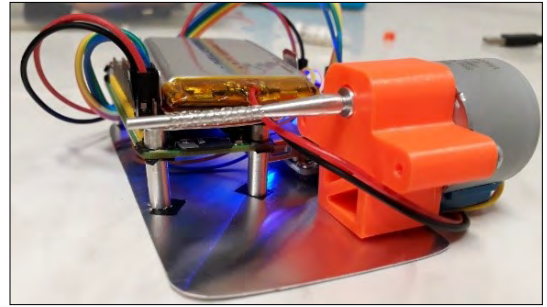


Figure 1. Prototype of the stent clamping and rotating device



Figure 2. Placement of stent clamping and rotating prototype in the chamber of a Zeiss EVO MA 10 scanning electron microscope

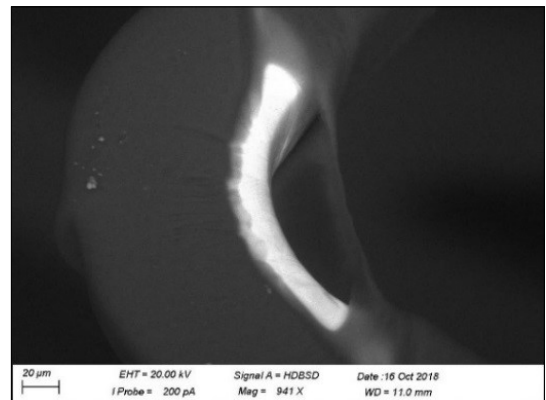


Figure 3. Damage on a strut of an amorphous silicon carbide coated drug eluting cobalt-chromium stent after expansion

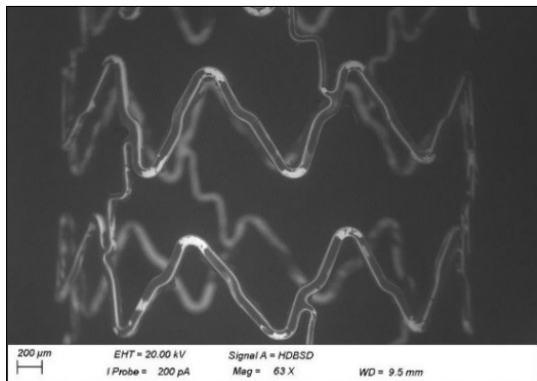


Figure 4. Electron microscopic image of two rings of a polymer-free drug eluting stent after expansion

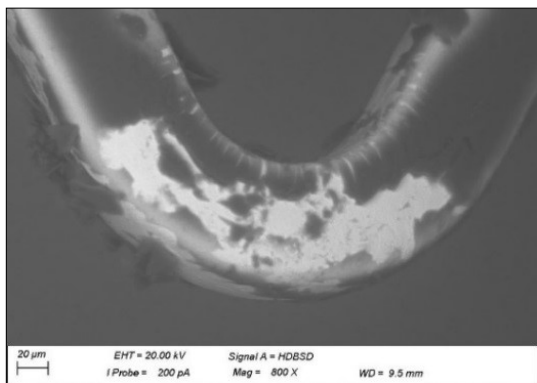


Figure 5. A large crack and peeling of the coating can be observed at the peaks of the strut curves on the examined polymer-free drug eluting stent after expansion

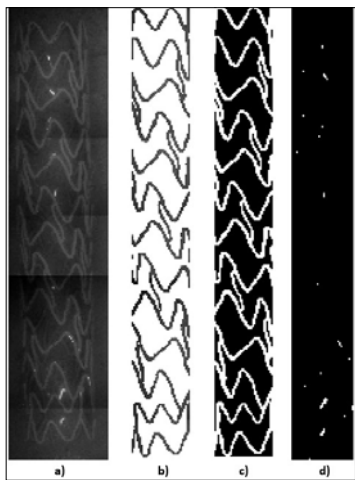


Figure 6. Steps of the image processing process: a) Composition of the electron microscope images. b) Circumcision of the stent. c) Binarization and complementation of the image. d) Location of coating damage on stent surface.

A much greater degree of damage can be observed for polymer-free coated drug eluting stents. This is partly due to the fact that some parts of the coating were dissolved from the stent surface prior to dilation in the fluid medium (water), and the coating thickness is also much smaller on these types (Figure 4 and 5).

2.2. Rating system for classification of coating damage

Based on the above, it can be concluded that the damage to stent coatings is mainly manifested in the separation from the metal surface. Based on this, for an objective evaluation system, we need to examine how much of the coating's total surface area has been removed from the metal. In order to be able to compare stents of different sizes, it is advisable to form a measure based on the ratio of damaged surface to total surface but at least on a given projection.

With the scanning electron microscope, we cannot take a picture at such a low magnification that the entire length of the stent can be seen in a single image, so we photograph the stent in sections and compose the stent using an image editing program.

By backscattered electron detection, coating defects can be well distinguished, since the intact polymer coating is darker and the metal base at the damaged sections appears lighter in the images (Figures 3–5). This can be exploited to determine the amount of damage to the stent surface using appropriate software. For image analysis, we first cut a stent from the rest of the image with a MATLAB code so that the dark background does not cause any problems with image analysis. The images are binarized and pixels of different darkness are calculated to give a measure of the ratio of the damaged surface to the observed projection. The image processing steps are shown in Figure 6. The illustrations were made prior to the availability of the stent clamping and rotating device. By developing this device, it will be possible to determine the extent of coating damage over the entire outer surface of the stent.

2.3. Corrosion test: measurement of open circuit potential

Using open circuit potential (OCP) the thermodynamic tendency of a material to undergo electrochemical oxidation can be characterized. During the OCP measurement, no current is applied to the working electrode, so the development of a so-called equilibrium or open circuit potential

can be recorded between the metal and the electrolyte solution. The change in open circuit potential as a function of time may indicate:

- oxidation, in which case the open circuit potential shows a decreasing tendency;
- for the formation of a passive oxide layer, in which case the OCP shows an increasing tendency; as well as
- inhibitor, the potential is constant [12].

The advantage of the measurement method is that it is independent of the size of the specimens, so stents of different diameters and lengths are easier to compare than by other electrochemical measurements. Determining the size of stent surfaces is also a complex process, so it is worthwhile to prioritize methods that exclude this factor. OCP measurements should be performed in standard 2-electrode cells. Phosphate buffer solution (PBS) was used for the electrolyte measurement in a composition as follows: 800 g H₂O 8 g NaCl; 0.2 g KCl; 1.44 g Na₂HPO₄; 0.24 g KH₂PO₄, with a pH value set for 7.4. The reference electrode was a Hg/Hg₂Cl₂ standard calomel electrode. During the measurements, the electrolyte temperature was maintained at 37±1°C and stirred at low speed (80rpm). The measurement layout is shown in Figure 7. Marked in the picture:

1. Potentiostat (Biologic SP-150);
2. Heated magnetic stirrer (IKA RCT basic)
3. Working electrode
4. Reference electrode
5. Holder

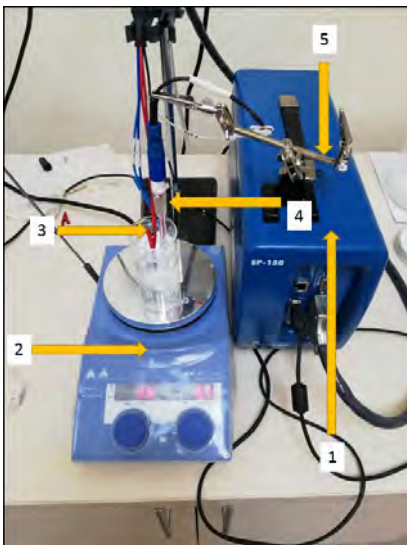


Figure 7. The two electrode cell and its parts used for the open circuit potential measurements

The main characteristics of the stents examined during the measurements: base material, coating material, expansion pressure (EP), manufacturer (Man.) are summarized in Table 1, and we will refer to each specimen marked as in the table below.

Table 1. Summary table of stents tested. For expansion pressure (EP), MP is the maximum allowable pressure, and NP is the nominal pressure. These pressure values are the values specified by the manufacturers and vary by stent type.

Mark	Material	Coating	EP	Man.
S1	X2CrNi-Mo18-15-3	No	MP	A
S2	X2CrNi-Mo18-15-3	No	NP	A
S3	Co-Cr-W-Ni	No	MP	B
S4	Co-Cr-W-Ni	No	NP	B
S5	Co-Cr-W-Ni	Amorphous SiC	MP	C
S6	Co-Cr-W-Ni	Amorphous SiC	NP	C
S7	Co-Cr-W-Ni	No	NP	D
S8	Co-Cr-W-Ni	Polymer free drug eluting stent	NP	D
S9	Fe-Pt-Cr	No	NP	E
S10	Fe-Pt-Cr	PVDF-HFP	NP	E

The OCP values of the above listed stents after a measurement time of 3600 seconds as well as the changes in the OCP are presented in Table 2.

Table 2. Open circuit potential values measured at the end of the 3600-second measurement time, as well as changes in OCP from baseline

Stent	OCP after 3600 seconds	Change in potential value
S1	0.0439	0.1167
S2	0.0424	0.1158
S3	-0.2097	-0.0348
S4	-0.1051	-1.0767
S5	-0.2953	-0.7531
S6	-0.2496	-0.0242
S7	-0.2256	0.1157
S8	-0.2188	0.1344
S9	0.1242	0.0680
S10	0.2173	0.0522

The austenitic stainless steel (X2CrNiMo18-15-3) stents have a positive open circuit potential value and an increasing tendency.

In the case of cobalt-chromium alloys (Co-Cr-W-Ni alloy) the OCP measurement showed a decreasing tendency in 4 cases and an increasing tendency in two cases. **Table 1** shows that the stents made from the similar cobalt-chromium alloy are manufactured by different manufacturers. In the case of bare metal stents, based on material composition results, it was found that although each stent conforms to the material composition according to ISO 5832-5 for the base material, the tungsten content of the stents showing a decreasing tendency is at the upper limit permitted by the standard (16%), for the samples, which showed an increasing OCP this alloy content was close to the lower limit (14%). Scanning electron microscopic images of the stents S3, S4 also show that the tungsten particles are at the edge of the grain (Figure 8), while in the case of S7, the distribution is homogeneous, the grain boundaries are not sharply drawn by tungsten (Figure 9).

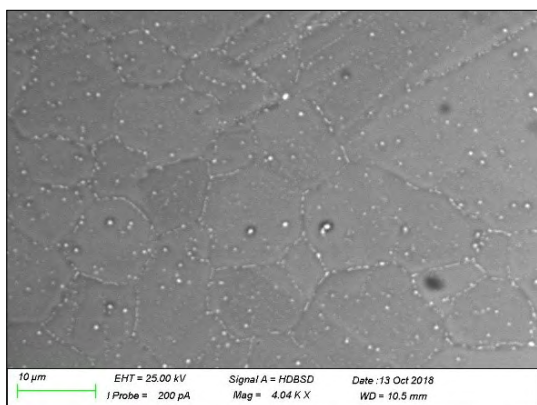


Figure 8. Electron microscopic image of S3 stent detail before corrosion tests, tungsten particles along the grain boundaries

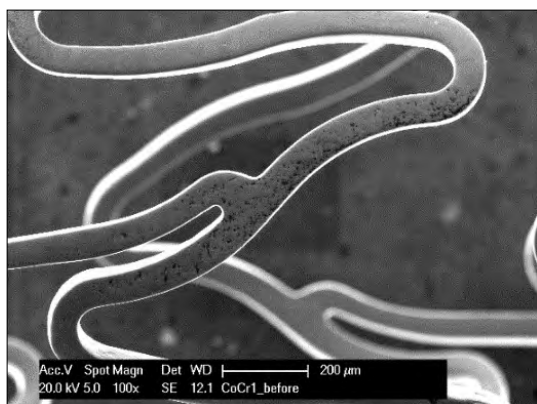


Figure 10. Electron microscopic image of a detail of the stent S3 before corrosion testing

Figures 10. and **11.** show that the surface of stent has much more discontinuities than S7, which may result from different surface treatments used by the manufacturers. A more uneven stent surface can adversely affect the corrosion characteristics. However, the potential value is negative in all 6 investigated cases for the Co-Cr-W-Ni alloy, so the corrosion resistance of this alloy type is weaker than that of the other two alloy types, regardless of the tendency.

Increasing the expansion pressure did not show a clear tendency for any alloy.

The open-circuit potential of the polymer coated Fe-Pt-Cr stent is the highest of the 10 examined stents, followed by the uncoated Fe-Pt-Cr and then the uncoated austenitic stainless steel stents. The polymer free drug eluting coating did not significantly affect the value of the open circuit potential, the primary reason being that some of the coating was dissolved during the measurement

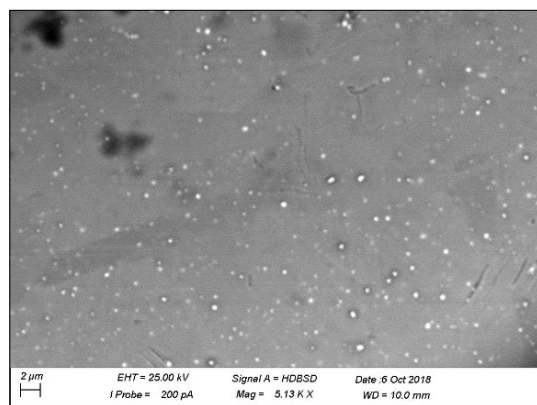


Figure 9. Electron microscopic image of S7 stent detail before corrosion tests, tungsten grain distribution more homogeneous than in case of the S3 stent showed in Figure 8

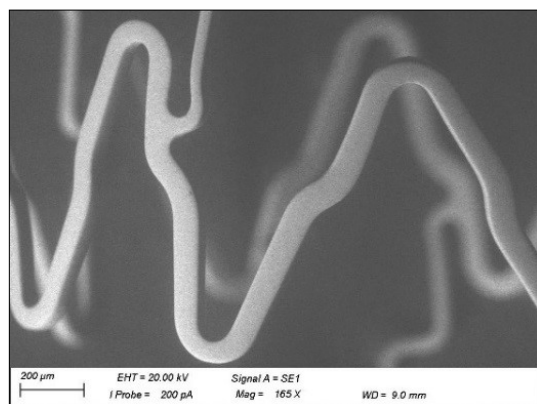


Figure 11. Electron microscopic image of a detail of the stent S7 before corrosion testing

and therefore did not exhibit an insulating effect such as the PVDF-HFP coating of the Fe-Pt-Cr stents or amorphous silicon carbide coating in the case of the S5 and S6 samples.

3. Summary

The primary purpose of this study was to develop a method of testing the coating damage of polymer-free and polymer-matrixed drug eluting coated stents in such a way that fixing and removal of the tested devices from the holder does not damage the test piece. To this end, we have created a prototype of a device that allows the stents to be fixed and rotated within the electron microscope chamber so that neither the specimen nor the coating on it is damaged during or after the test. We also created a method for evaluating the electron microscopic images thus prepared, which quantifies the extent of coating damage on the stents tested using MATLAB.

In the second half of our research, open circuit corrosion tests were performed to investigate the effects of coatings on corrosion properties. Based on our measurements, it can be concluded that the resistance of the polymer-matrix drug eluting coated stents to corrosion is better than that of uncoated stents, but the polymer-free coating did not have a significant effect on corrosion resistance. Our results provide a good basis for our new research focusing on coating development.

Acknowledgement

Supported by the ÚNKP-18-3-II New National Excellence Program of the Ministry of Human Capacities. A special thanks to Adam Meisel, student of mechanical engineering, for his help in the development of the stent clamping and rotating device. I owe a debt of gratitude to the staff of the Department of General and Physical Chemistry of the University of Pécs for providing me the measuring equipment.

References

- [1] Mani G., et al.: *Coronary stents: A materials perspective*. *Biomaterials*, 28. (2006) 1689–1710. <https://doi.org/10.1016/j.biomaterials.2006.11.042>
- [2] Wienke H., et al.: *Stent coating with titanium-nitride-oxide for reduction of neointimal hyperplasia*. *Circulation*, (2001) 928–933. <https://doi.org/10.1161/hc3401.093146>
- [3] Bognár E. et al.: *Investigation of Drug Eluting Stents*. *Materials Science Forum*, 589. (2008) 361–366. <https://doi.org/10.4028/www.scientific.net/MSF.589.361>
- [4] Bognár E. et al.: *Investigation of Coated Coronary Stents*. *Materials Science Forum*, 537–538. (2007) 307–314. <https://doi.org/10.4028/www.scientific.net/MSF.537-538.307>
- [5] Hausleiter J. et al.: *Prevention of restenosis by a novel drug-eluting stent system with a dose-adjustable, polymer-free, on-site stent coating*. *European Heart Journal*, 26/15. (2005) 1475–1481. <https://doi.org/10.1093/eurheartj/ehi405>
- [6] Selley T. L. et al.: *Development of adhesion test for coated medical device*. *Biomechanica Hungarica*, (2013) 303–310. <https://doi.org/10.1093/eurheartj/ehi405>
- [7] Ginzstler J. et al.: *Development and Manufacturing of Coronary Stents in Hungary*. *Materials Science Forum*, 537–538. (2007) 631–638. <https://doi.org/10.4028/www.scientific.net/MSF.537-538.631>
- [8] Khan W. et al.: *Drug eluting stents: Developments and current status*. *Journal of Controlled Release*, 161/2. (2012) 703–712. <https://doi.org/10.1016/j.jconrel.2012.02.010>
- [9] Park J. K. et al.: *Development of a novel drug-eluting stent consisting of an abluminal and luminal coating layer dual therapy system*. *RSC Advances*, 5. (2015) 40700–40707. <https://doi.org/10.1039/C5RA04270D>
- [10] Horicsányi K. et al.: *Effect of Expansion Pressure on the Drug Eluting Coating of Coronary Stents*. *Acta Materialia Transylvanica*, 1/1. (2018) 37–40. <https://doi.org/10.2478/amt-2018-0012>
- [11] Asztalos L. et al.: *Kobalt-króm ötvözet alapanyagú sztentek korróziós tulajdonságainak vizsgálata*. *Műszaki tudományos közlemények*, 7. (2017) 79–82. <https://doi.org/10.33895/mtk-2017.07.12>
- [12] Jiménez Y. S. et al.: *Interpretation of open circuit potential of two titanium alloys for a long time immersion in physiological fluid*. *Bulletin of the Transilvania University of Brasov, Series I: Engineering Sciences*, 2/51. (2009) 197–204.

Microstructural Characterisation of Archeologic Finds Discovered at the Ironworks in Mădăraş

Enikő BITAY¹, László MÁRTON², János TALPAS³

¹ Sapientia Hungarian University of Transylvania, Faculty of Technical and Human Sciences, Târgu-Mureş, Romania, ebitay@ms.sapientia.ro

² Transylvanian Museum Society, Departement of Technical Sciences, Cluj, Romania, martonlb@yahoo.com

³ Babeş-Bolyai University, Cluj, Romania, talpasjanos@gmail.com

Abstract

In the middle of the 16th century the ironworks of Mădăraş was one of the important centres of iron production. During its one and a half century lifespan its output provided a significant part of Transylvania's iron supply. While it operated it used up the entire raw material extracted in the iron ore mines of the Felcsik basin. This study presents the reconstructed ground-plan of the ironworks, its layout on the shores of the Mădăraş creek, and the chemical composition and microstructure of the samples discovered during exploration of the location by means of XRF analysis, EDS analysis and metallography. The analysis of the pig iron, the steel and the slag although performed on individual samples, still provides a good approach regarding the products of the ironworks, their chemical composition and microstructural characteristics.

Keywords: *ironworks, microstructure, metallography, spectrometry, use of waterpower, melting, smithy.*

1. Introduction

Documents from the time of the Principate of Transylvania contain a considerable amount of information about the mining, production and manufacturing of iron, at and around the already known as well as the more recently discovered iron sources in the Szekely land [1], [2]. In the middle of the 16th century one of the centres of Transylvanian iron production, [3] the Mădăraş ironworks was already producing iron [4], [5]. During its lifespan of one and a half centuries its output contributed significantly to Transylvania's iron demands. Besides the fact that it was profitable, it was important also because inhabitants from ten settlements of the Csikszék jurisdiction were employed there and therefore enjoyed tax exemption, moreover, quite a few of the employees from the Ciuc, Gheorgheni and Caşin areas received the minor nobiliar title of „lófő” (an exclusive rank among the Szekelys) from Transylvanian prince Báthory Zsigmond [6].

In those times it was already known that in the Mădăraş area of Harghita county there was

iron ore. It is a characteristic of the Mădăraş ironworks that basically the entire product of the mines from the upper Ciuc basin was melted there. In 1659 the Mădăraş ironworks began to decay fast and an inventory document from 1703 already tells about its deplorable condition. At that time it was rented for a mere 40 forints, when the market price of an ox was around 10-14 forints. In 1722 when it was rented again the contract doesn't even mention iron production, the object of the contract was only the land and the still functioning sawmill.

The ironworks functioned continuously between 1567 and 1725. Its demise was attributed to lack of iron ore which in fact is only one of the many shortcomings: The most important was without a doubt the owners' bad management.

2. The ironworks and its products

In the Mădăraş ironworks both the equipment and the production processes was at that time considered state of the art. The ideal conditions were provided by the large and constant water discharge of the fast flowing Mădăraş creek. Close to

the ironworks there was a beech forest that provided plenty of beech wood as the raw material for charcoal burning, the iron quarry was also close by as was the limestone which is important in slag forming. The ironworks could function continuously from April to November, that is, the entire frost-free period of the year.

In 1673 there were 137 employees only one of whom was an iron stone seeker – today we would call him a Geologist. Two judges of the ironworks coordinated the activity of the miners, the melters, the smiths, the cobblers who made blowers, the smiths who sharpened pickaxes, the iron beaters and the cart handlers. It was probably a well organized venture. The quantity of the produced iron reached 19 tons a year. Comparing that with the five ironworks of Hunedoara we see that the combined yield of those only exceeded that of the Mădăraş ironworks by 118 kg a week.

The product was at the disposal of the prince's court. It was sent to Iernut, Gurghiu, Dumbrăveni or Făgăraş for further processing. In Mădăraş iron rods, cannon balls, horseshoes, horseshoe nails and agricultural tools were made. Looking back 280 years from the present, the truth is that as a consequence of nature's transformative powers

and of human negligence, today only professionals can realize the true size of this once thriving ironworks. Based on an inventory made in 1677 a ground plan was realized that is the first one to present a probable picture of what it must have looked like (**Figure 1**).

According to the ground plan the ironworks was on the right shore of the Mădăraş creek. From the creek a mill race ran into a water reservoir which still can be found today (C in **Figure 1**.) the purpose of which was to provide a constant water discharge under a constant pressure to the three water wheels. The propulsion of a fourth water wheel was provided by the Mădăraş creek itself. There were two iron melting stoves (3 and 7) the outputs of which was taken for further processing to the smithies (4 and 6).

On the site the iron stone sifter and roaster (2) the iron ore was prepared for processing, melting. The building marked 5 was the deposit for the finished products. The coal barn (9) received the loads of the carts, the charcoal. Carts entered the site through the gate (A). Besides these, some of the buildings had multiple functions such as lodgings, leather processing workshop etc.

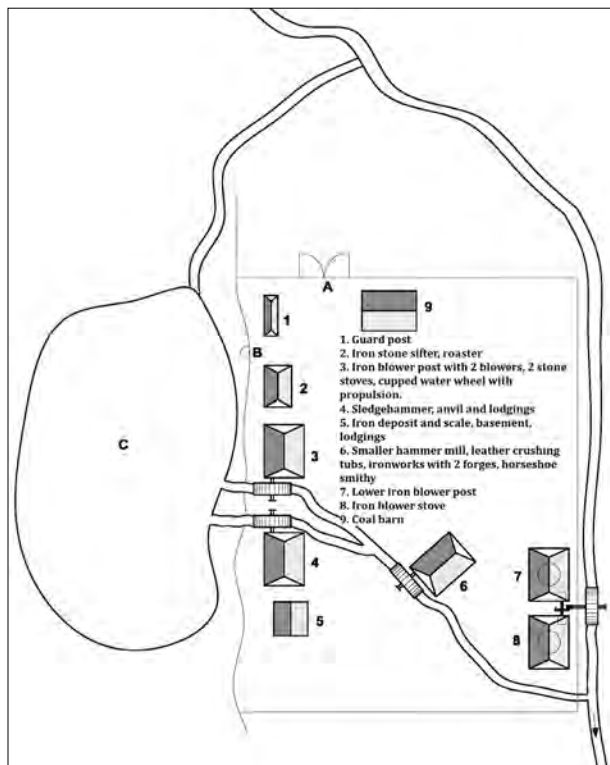


Figure 1. The ground plan of the Mădăraş ironworks

3. Analyses of the residues from the ironworks

As a result of several searches on the site different residues were found: slag, pig iron and steel residues.

From these materials we cut samples for research. The chemical analysis was done by Thermo Niton XL3T type X-ray fluorescence spectrometer (XRF), SPECTROTEST TXC25 type optical emission spectrometer (EDS) and the spectrometer of the Zeiss EVO10 scanning electron microscope. We used an iqualitrol iMet-400 and an Olympus PMG3 metallographic microscope, also a stereo-microscope (macroscope) and a scanning electron microscope to analyse the surface of the sample pieces and on metallographic samples also their inner structure. **Table 1.** shows the results of this chemical analysis

Analysing the three rows of data in **Table 1**, the following conclusions can be drawn:

- The iron content of the residues is between 38,3–74%. The only remarkable aspect of this data compared to information regarding the composition of modern iron forging residues is that the iron content of the slag is 38.3 %, which is the result of poor extraction. In the slag there is a significant quantity of rare and expensive metals, such as Zn, Ni, Sb, extracting those from the mountain of slag that was produced during the lifespan of the ironworks could be an oportune task.
- Naturally the pig iron samples contain more iron, around 32.1 %. It should be noted that the cast iron typically has a Si content of 5.8 %. There isn't much Cr and Sb but that could be a characteristic of the iron ore from Mădăraş. In the pig iron samples prepared for metallographic analysis, polished but not milled, the rosette-type distribution of graphite is clearly visible (see **Figure 2.** a-b).
- During the XRF analysis of the steel samples copper was recorded (290 ppm), while the proportion of nickel decreased (38 ppm). The pre-

sence of zinc, aluminium and tin is a sign of a complex ore, yet it is unusual that these metals survived the melting temperature of the iron. The phosphorus and sulphur content of the steel produced there is low according to the XRF analysis (the spectrometer didn't reveal any of these elements), but EDS analysis done on different points of the polishes showed clearly that the composition of the steel sample varies from point to point. There are significant quantities of pollutants and the material is roughly slaggy which is typical for the technologies of those times.

As a result of the repeated heating and beating which was typical for the iron production of the age, the initially very non-homogenous material was homogenized, graphite burned out and slags were beaten out of it and thus it became usable steel product. If we could find and analyse larger quantities of pig iron and steel, we could obtain more precise results. Maybe a more comprehensive archaeological excavation could unearth more iron residues but that is unlikely as we know that even the iron nails used for fixing the parts of the gate were contained in the inventories.

4. Microstructural analysis of the materials

4.1. Analysis of the slag

From the materials collected on location we analysed the chemical composition of the slag with EDS method focusing on the surface shown in **Figure 3.a** which is the inner fracture surface of the slag. The intensity diagram of the EDS analysis and the composition that can be defined based on the diagram is shown in **Figure 3.b**. Repeating the EDS analysis on different spots we came to the conclusion that the mass percentage of iron is consistently between 42–44%, Silicon is around 7%, manganese content is 2–3% and aluminium is also present at more than 1%. Comparing this with

Table 1. Results of the XRF analysis (%)

	Fe	Mn	Si	S	P	Cr	Ni	Cu	Zn	Mo	Al	Sb	Sn	As
Slag residues	38.3	3.2					0.0345	0.0092	0.0712			0.0077		0.0061
Pig iron residues	62.1	0.75	5.8	0.11	0.76	0.0498						0.0109		
Steel residues	74						0.0038	0.0290	0.0100	0.0020	0.0100		0.0100	

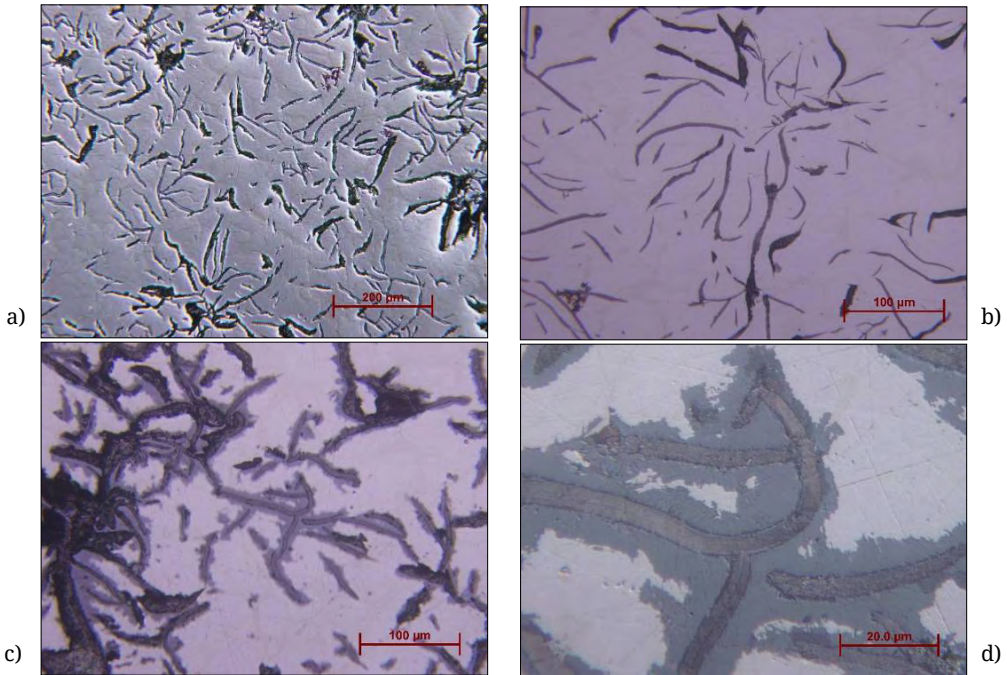


Figure 2. Microstructure of the pig iron in polished state on the inside of the sample (a-b) and in the proximity of the corroded surface (c-d)

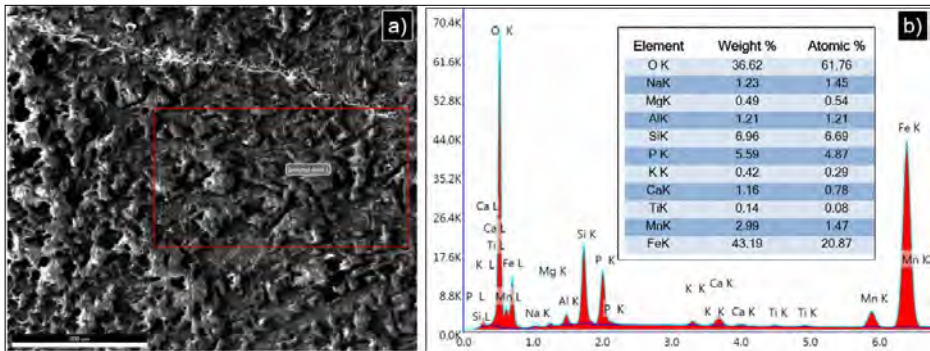


Figure 3. Detail of the fracture surface of the slag (a) and the intensity diagram and the chemical composition that resulted from the EDS analysis made on the marked area (b)

the results obtained by XRF it is striking that EDS gives a much higher phosphorus content (5–6%) which is evidence to the limitations of XRF analysis [7–10].

4.2. Analysis of pig iron

We took a sample from the found materials, we prepared a metallographic sample which was analysed by means of metallographic microscopy and scanning electron microscope in a polished state and after etching it with a 4% Nital etchant. In **Figure 2**, we can identify, based on the ISO 945-1:2019 standard, the shape, dispersion and size of

the lamellar structured graphite. The shape falls between classes I. and II., the dispersion is class B type (rosette graphite) while the size is around 3rd and 4th on the 8 degree scale. Close to the surface of the sample, along the phase boundary between ferrite and graphite the material is strongly corroded as shown in **Figure 2c-d**.

Analysis in the polished state only allows us to determine the structure of the graphite, etching is necessary in order to identify the matrix [11]. But etching can destroy the corroded parts along the borders of the graphite plates in strata close to the surface therefore determination of the chemical

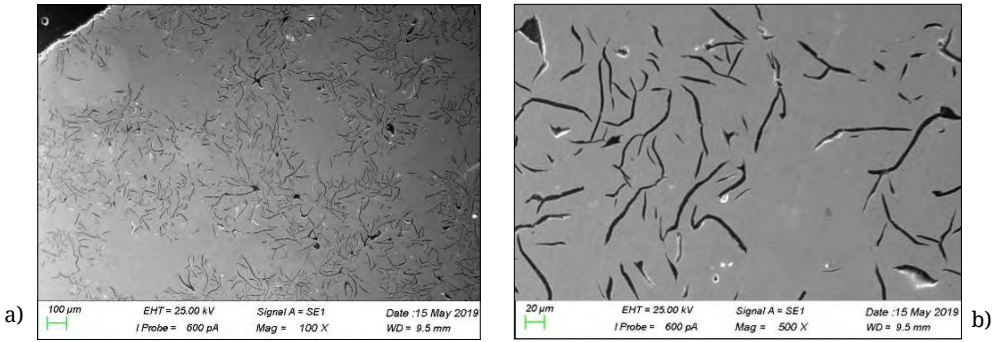


Figure 4. Microstructure of pig iron in polished state on secondary electron image

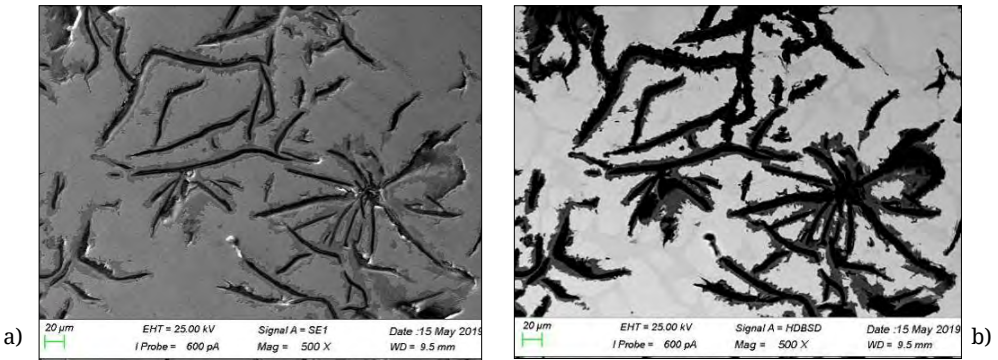


Figure 5. Microstructure of pig iron close to the surface in polished state on secondary electron image

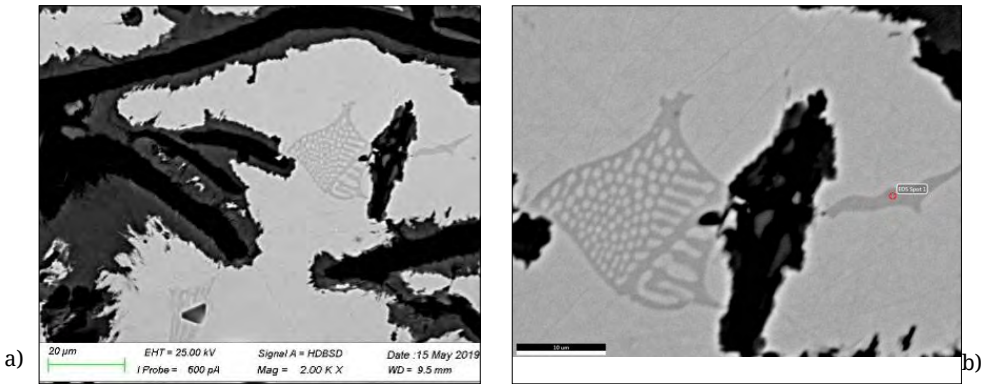


Figure 6. The part of the microstructure that contains phosphide eutectic on secondary electron image

composition of the materials in certain characteristic points by means of the scanning electron microscope EDS analyser had to be performed before etching. **Figure 4.** shows the secondary electron image of the polished sample. Analysing the entire surface shown in **Figure 4b.** the quantity of the main components – without iron and carbon – is as follows: Si = 0.77%, Mn = 1.17%, P = 1.72%.

The image of the part close to the surface is shown in **Figure 5.** On the phase borders of the graphite plates, corrosion products formed in

which EDS analysis showed atomic proportions of 43% iron and 56 % oxygen which is close to the Fe/O atomic proportion of magnetite. **Figure 6** shows a magnified detail of **Figure 5b** on which a section containing phosphide-eutectic is clearly visible. The atomic proportion of phosphorus in this eutectic is 17%, in the phosphide plate it is 25%.

Etching with Nital elevated excellently the morphological characteristics of the iron-rich elements of the microstructure. From the images

in **Figure 7**. of the molten material that is cooled down to eutectic temperature becomes austenite. The rest becomes ledeburite. Cooling must have been fairly rapid, which can be seen from the fact that the structure of the ledeburite, as well as that of the pearlite formed from austenite, is very fine.

4.3. Analysis of steel

From this sample a metallographic polish also prepared and analyzed in a polished state and after etching it with Nital. Microstructural images in **Figure 8**. show that the material of the sample suffered significant transformation after it was made into pig iron. The main characteristics of

the formed microstructure are the following:

a) Along its thickness the material is segmented into zones with very different carbon content. In the parts with low C content only the boundaries of the ferrite grains were etched while the darker segments contain more C since the composition of the material in these segments is almost entirely eutectic. In **Figure 8.e** for example, 95% of all the constitutions are pearlite, while proeutectoid ferrite is only 5%.

b) The material is very significantly sluggy, slag enclosures are dense especially in strata close to the surface. However, in this zone close to the

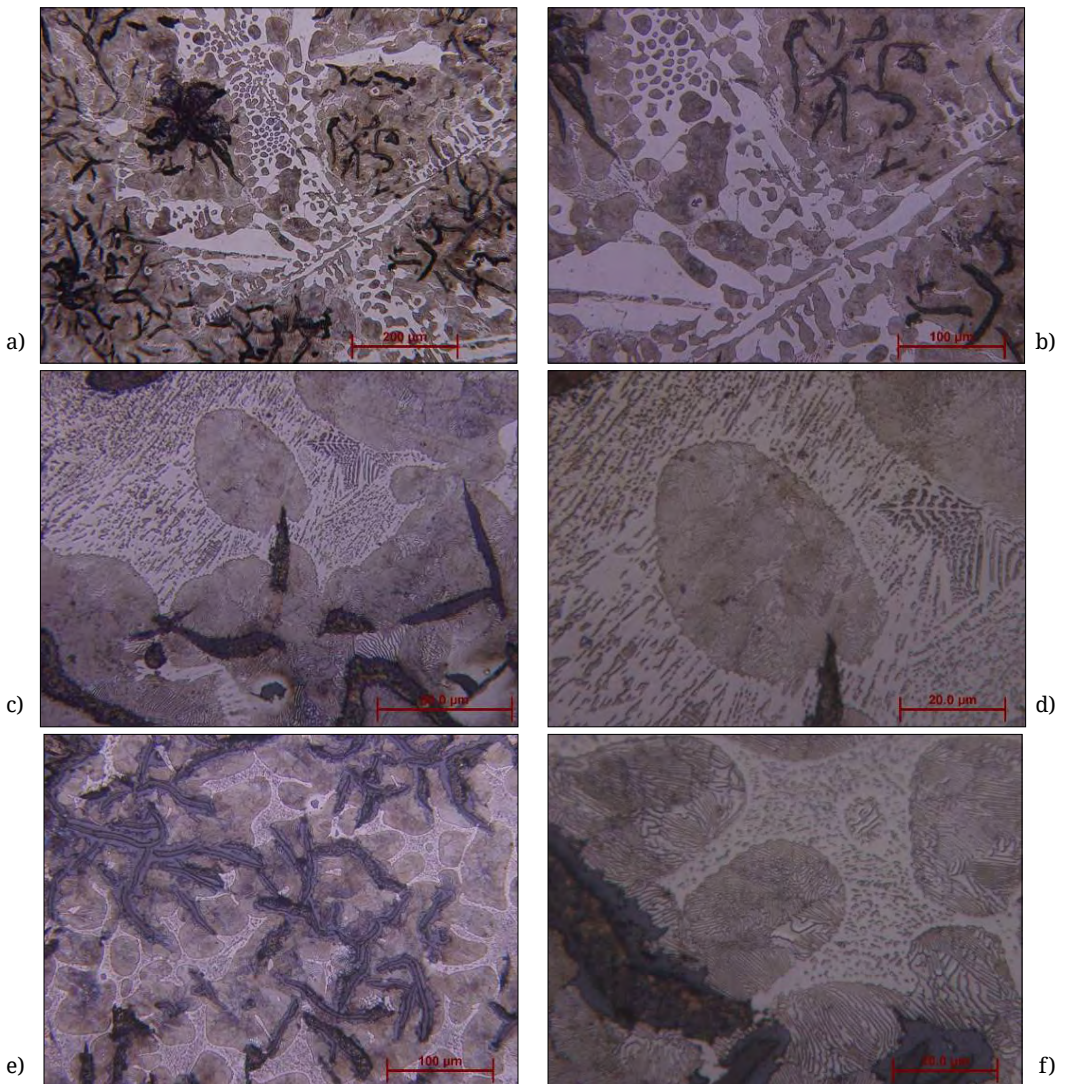


Figure 7. Microstructure of the pig iron in polished state in the inside of the sample (a-b) and in the proximity of the corroded surface (c-d).

surface C-content is lower, 0.037% according to SPECTROTEST analysis. Besides carbon, Si, Mn and Sulphur was almost completely burned out, P content is also only 0.079%. The burning of the components and the high degree of slag inclusions shows that smithing was done at very high temperatures and with lengthy annealing, and that the surface could not be properly protected from oxidizing.

c) The extent of plastic deformation caused by the smithing process was significant.

d) The final heat treatment state in the decarbonized parts corresponds to complete annealing

(Figure 8.c), while in the high C content strata of the 12 mm thick sample it corresponds to the acicular ferrite and fine plate pearlite structures that form as a result of a not too rapid cooling. In Figure 9.b the inner structure of a thick layer of slag is shown in polished (not etched) state.

5. Conclusions

This work is the first attempt at the reconstruction of the 16th century Mădăraş ironworks and the description of its products through methods of Material Science. Analysis shows that the used iron ore, the siderite wasn't the only mineral in a

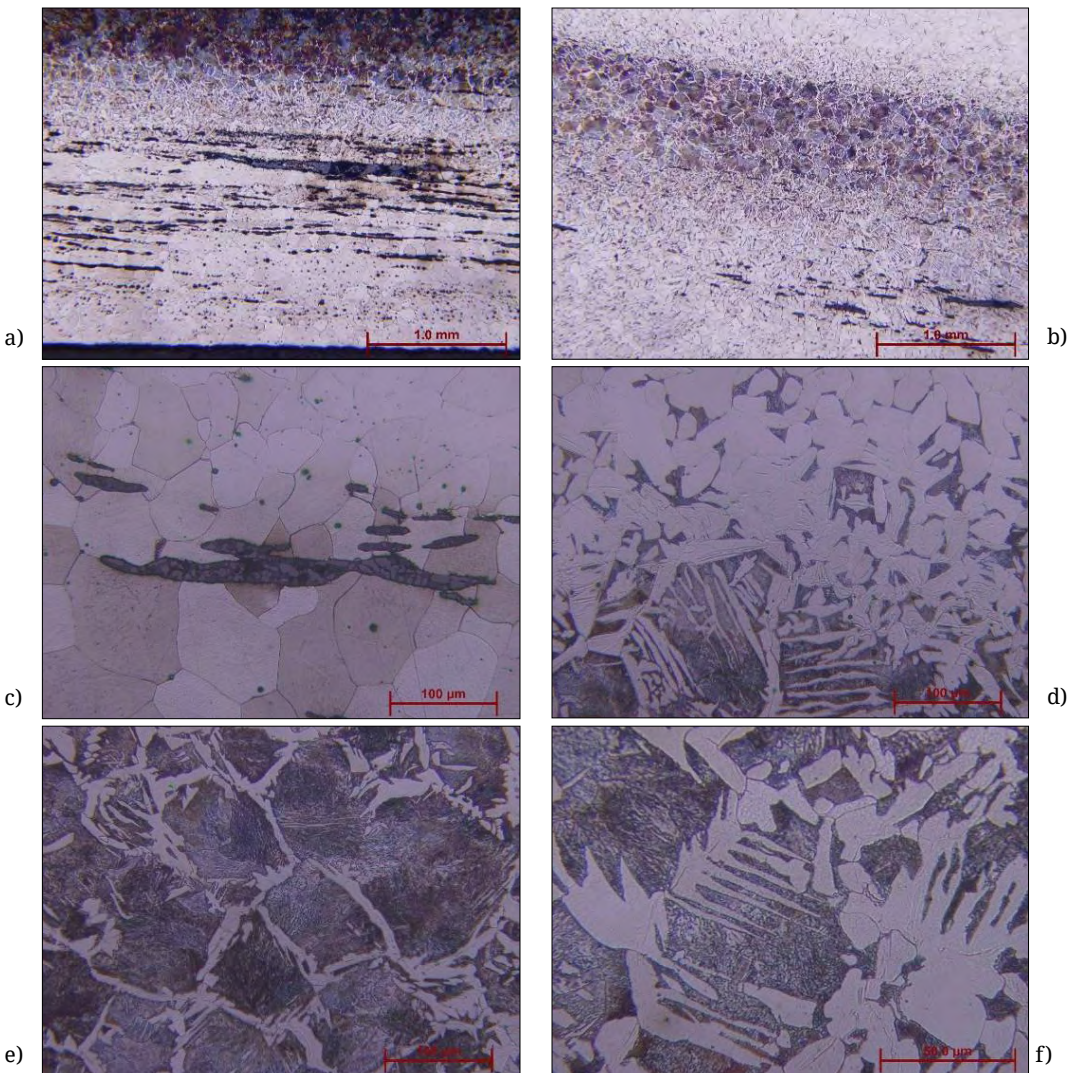


Figure 8. Microstructure of the steel sample in the individual layers formed along its thickness (etchant: Nital-4)

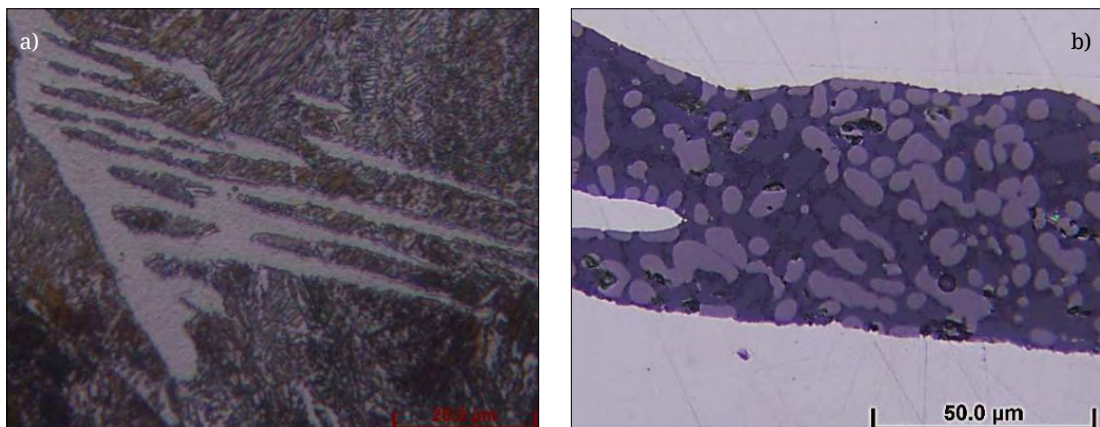


Figure 9. a) Microstructure of the steel sample in high C content layers (etchant: Nital-4), b) Microstructure of the slag enclosure in polished state

complex ore but it appeared alongside andesite tuffs, limestone, dolomite, crystallized slates etc. These are the sources of the chemical elements that make the composition of the Mădăraș iron unique.

Analysing the composition and structure of the residues shows that by modern standards, the steel products of the ironworks were characterised by significant inhomogeneity. This obviously had an influence on the mechanical properties of the products but it's very likely that the technologies of that age didn't allow for a better quality material in mass production.

During the ironworks' 170 year lifespan a significant amount of slag was accumulated containing precious elements (Zn, Ni, Sb etc.). Extracting those could be a timely task.

References

- [1] Guran M.: *Fierul*. Editura Tehnică, București, 1978.
- [2] Szakács A.: *The siderite of the neogene volcanism-related ironores in the East Carpathians (Romania)*. Mineralogy and chemical features. Romanian Journal of Mineralogy, 75/1. (1992).
- [3] Latinák Gy.: *A vajdahunyadi m. kir. vasgyár és tartozékai I–IV*. Bányászati és Kohászati Lapok, 39/2. (1906) 2–48, 73–99, 137–172, 203–242.
- [4] Jakab Gy.: *Székelyföld értelempei*. Tanulmányok Erdély földtanából. Földtani közlöny, 135/3. (2005) 459–478.
- [5] Pataki J.: *A csíki vashámor a XVII. század második felében*. Csíkszereda, 1971. 48–54.
- [6] Orbán B.: *Székelyföld leírása I*. Pest 1863, Csíkszék, 57–72.
- [7] Rousseau R. M.: *Detection limit and estimate of uncertainty of analytical XRF results*. The Rigaku Journal, 18/2. (2001) 33–47.
- [8] Kadachi A. N., Al-Eshaikh M. A.: *Limits of detection in XRF spectroscopy*. X-ray Spectrometry, 41/5. (2012) 350–354.
<https://doi.org/10.1002/xrs.2412>
- [9] Borkhodoev V. Y.: *Estimation of limits of detection and determination in X-ray fluorescence analysis by the dependence of the relative standard deviation on analyte concentration*. Journal of Analytical Chemistry, 71/9. (2016) 872–877.
<https://doi.org/10.1134/S1061934816070054>
- [10] Liss B., Levy T. E.: *Using X-Ray Fluorescence to Examine Ancient Extractive Metallurgy Practices: A Case Study from Iron Age Khirbatal-Jariya, Jordan*. Journal of Powder Metallurgy & Mining, 5/1. (2016) 1–5.
<https://doi:10.4172/2168-9806.1000140>
- [11] Renkó J. B., Kemény D. M., Nyiró J., Kovács D.: *Comparison of cooling simulations of injection moulding tools created with cutting machining and additive manufacturing*. MaterialsToday: Proceedings, 12. (2019) 462–469.
<https://doi.org/10.1016/j.matpr.2019.03.150>

Examination of Heat Treatment on the Microstructure and Wear of Tool Steels

Enikő Réka FÁBIÁN,¹ László TÓTH,² Csenge HUSZÁK³

Óbuda University, Donát Bánki Faculty of Mechanical and Security Engineering, Budapest, Hungary

¹ fabian.reka@bgk.uni-obuda.hu

² toth.laszlo@bgk.uni-obuda.hu;

³ huszak.csenge@bgk.uni-obuda.hu

Abstract

The microstructure of the investigated X153CrMoV12 grade tool steel in delivered condition consisted of spheroidal matrix and primary carbides. The primary carbides were not dissolved under austenitisation time on either 1030°C or 1070°C. The microstructure and abrasion resistance of the steel changed due to quenching from different austenitisation temperatures. After conventional quenching from the higher austenitising temperature, there is more residual austenite in the steel than at quenching from the lower austenitisation temperature, which decreased the wear resistance. As a result of quenching from 1070°C followed by a multiple tempering process around 500 to 540°C, the retained austenite content is reduced and finely dispersed carbides are precipitated in the matrix, resulting in a higher matrix hardness and an increased wear resistance. After cryogenic treatment, the residual austenite content decreases compared to the conventional process, which leads to an increase in hardness and wear resistance.

Keywords: *tool steel, austenitisation, retained austenite, precipitation, cryogenic treatment, tempering, wear resistance.*

1. Introduction

The X153CrMoV12 grade steel is commonly used by tool makers as a raw material for blanking and punching tools, woodworking tools, shear blades for cutting light-gauge material, thread rolling tools, tools for drawing, deep drawing and cold extrusion, pressing tools for the ceramics and pharmaceutical industries, cold rolls (working rolls) for multiple-roll stands, measuring instruments and gauges and small moulds for the plastics industry where excellent wear resistance is required. This steel in delivered condition is annealed, the hardness is max. 250HB. In this state the steel is relatively easy to be manufactured despite its high alloy content. The properties of the tool are achieved in the final heat treatment. There are differences in the recommendations for heat treatment, despite the fact that the X153CrMoV12 grade steel is widely used. Small dimension changes and high hardness is usu-

ally achieved after quenching from 930–960°C [1]. Using high quenching temperature (1100°C), secondary hardening appears in the material the maximum hardness result after tempering at 520–530°C. The standard [2] recommendation for austenitisation is 1020°C, and cooling in air. The standard for maximum hardness (over 62 HRC) recommends 970°C for austenitisation, air quenching followed by tempering under 200°C

Voestalpine is one of the world's leading tool steels, high-speed steels and special steels manufacturers. The company publication does not provide data on secondary hardening after the hardening process from 1030°C, but secondary hardening is expected at 520°C after hardening from 1070°C, so double tempering at this temperature is recommended before any nitration [3]. Inter-alloy recommends triple tempering at 500–550°C [4]. Cryogenic treatment is not mentioned by companies, nor by the standard, although when cooled to room temperature with this carbon con-

tent, the martensitic transformation is not completed [5]. While company data do not suggest a relationship between wear resistance and heat treatment parameters, the effects of deep cooling and tempering on mechanical and wear properties have been addressed by several researchers for similar cold forming tool steels [6–11]. The tool makers ask from the heat treatment shops only the Rockwell hardness, however, tool life, wear resistance, and toughness depend also on the heat treatment technology.

2. Test materials and methods

The chemical composition of the examined X153CrMoV12 grade steel is shown in Table 1.

Table 1. Chemical composition of the test material

C	Cr	Mo	V	Si	Mn	Fe
1.67	11.25	0.837	1.41	0.364	0.422	rest

Austenitization of the 20×40×20 mm samples was carried out at 1030°C and 1070°C, respectively, in an Ipsen VFC type vacuum furnace with 300×370×200 mm chamber size after a two-holding steps at 650°C and 900°C. Some of the samples were quenched down to 40°C conventionally, using nitrogen gas, and some samples were cryogenic treated in nitrogen to –80°C for 3 hours. The effects of simple and multiple tempering on the microstructure and wear resistance were studied for the conventional and cryogenic quenching.

The experimental samples were examined after metallographic preparation using an Olympus PMG3 light microscope (LOM) and a Jeol JSM 5310 scanning electron microscope (SEM). Primary examination was of the carbides size and distribution in the microstructure using nital. For the determination of retained austenite the Beraha'2 reagent (85 ml water, 15 ml HCl, 1 g K₂S₂O₅) proved to be the most suitable. Beraha'2 reagent colors the ferrite and martensite but not austenite and carbides. The primary carbides are clearly distinguishable from the matrix. The carbide precipitations in the matrix are spherical, and so could be distinguished from the residual austenite. The hardness of the carbides and of the matrix after different heat treatments was measured with Vickers hardness testing equipment type Buhler 1105.

For the wear resistance testing, a self-developed abrasive equipment was used [12] (Figure 1.). The used abrasive tool was a 20 mm diameter Al₂O₃ ceramic ball with polished surface. The

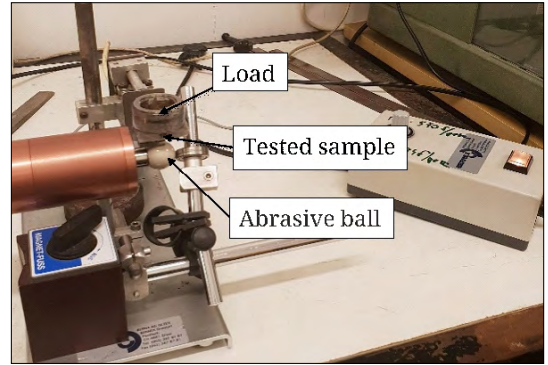


Figure 1. Abrasive equipment

loading force was provided by the sample which supported a load with 50g.

The wear factor (K) was used as a measure of wear resistance, calculated from the volume mass loss (V_v), the sliding distance (s) and the normal load (F):

$$K = \frac{V_v}{s \cdot F} \text{ (mm}^3\text{)/(m} \cdot \text{N)} \quad (1)$$

The volume mass lost is calculated from the diameter of the calotte formed during the wear (d) and the depth of the crater (h):

$$V_v = \frac{h \cdot \pi}{6} \left(\frac{3}{4}d^2 + h^2 \right), \text{ (mm}^3\text{)} \quad (2)$$

The height of the abrasive calotte is calculated by a simple relationship between the radius R of the abrasive ball and the diameter of the calotte formed during the wear test:

$$h = R - \sqrt{R^2 - \left(\frac{d}{2}\right)^2}, \text{ mm} \quad (3)$$

The sliding distance (s) depends on the time of the wear (t), on the radius of the abrasive ball (R) and its rotational speed (n) (4):

$$S = n \cdot 2 \cdot \pi \cdot R \cdot t, \text{ m} \quad (4)$$

For comparison with literature data [11–12], the speed was 570 rpm and the abrasion test time was 5 minutes.

3. Test results

The hardness of the tested X153CrMoV12 grade tool steel in delivered condition was 248 HV 1 on average and its microstructure consisted of a spheroidal matrix and primary carbides. The austenitisation temperature recommended by

Voestalpine Hungary Kft. strongly influences the microstructure and hardness of the treated material.

3.1. Effect of the austenitisation temperature

Examining the microstructure of the samples, it was found that the primary carbides did not dissolve during heating at 1070°C, as can be seen in the photos of **Figures 2.a)** and **b)**. As shown in the photos of **Figures 2.c)** and **d)**, quenching from a higher austenitization temperature resulted in more residual austenite than in the case of quenching from 1030°C. Hardness and wear resistance test results are fully consistent with the microstructure. When the sample was quenched from 1030°C, the average hardness of the matrix was 674 HV1, while for the sample quenched from 1070°C it was 648 HV1. By increasing the austenitising temperature, the wear coefficient increased from $2.46 \cdot 10^{-5} \text{ mm}^3/\text{Nm}$ to $2.94 \cdot 10^{-5} \text{ mm}^3/\text{Nm}$ due to the higher retained austenite content. The distribution of retained austenite is always uniform in the matrix. The primary carbides appearance was similar after quenching from 1030°C and 1070°C. This microstructural similarity explains the phenomenon that the Rockwell hardnesses measured after quenching are the same (**Table 2.**).

Table 2. The effect of heat treatment parameters on hardness and wear resistance

Hardening		Tempering (°C)			HRC	HV 1	K (mm ³ /Nm)
T _A (°C)	HRC	T ₁	T ₂	T ₃			
1030	62	–	–	–	62	674	$2.46 \cdot 10^{-5}$
1030	62	200	–	–	61	668	$1.56 \cdot 10^{-5}$
1070	62	–	–	–	62	648	$2.94 \cdot 10^{-5}$
1070	62	200	–	–	61	641	$1.04 \cdot 10^{-5}$
1070	61	520	–	–	60	663	$2.22 \cdot 10^{-5}$
1070	61	520	540	–	59	685	$3.00 \cdot 10^{-5}$
1070	61	520	540	500	59	748	$2.46 \cdot 10^{-5}$

3.2. Effect of tempering

The temperature and number of cycles of tempering following the quenching after austenitization at 1070°C significantly influence the microstructure, hardness and wear properties of the X152CrMoV12 steel. The amount of fine dispersed carbides in the martensite is very small (photos

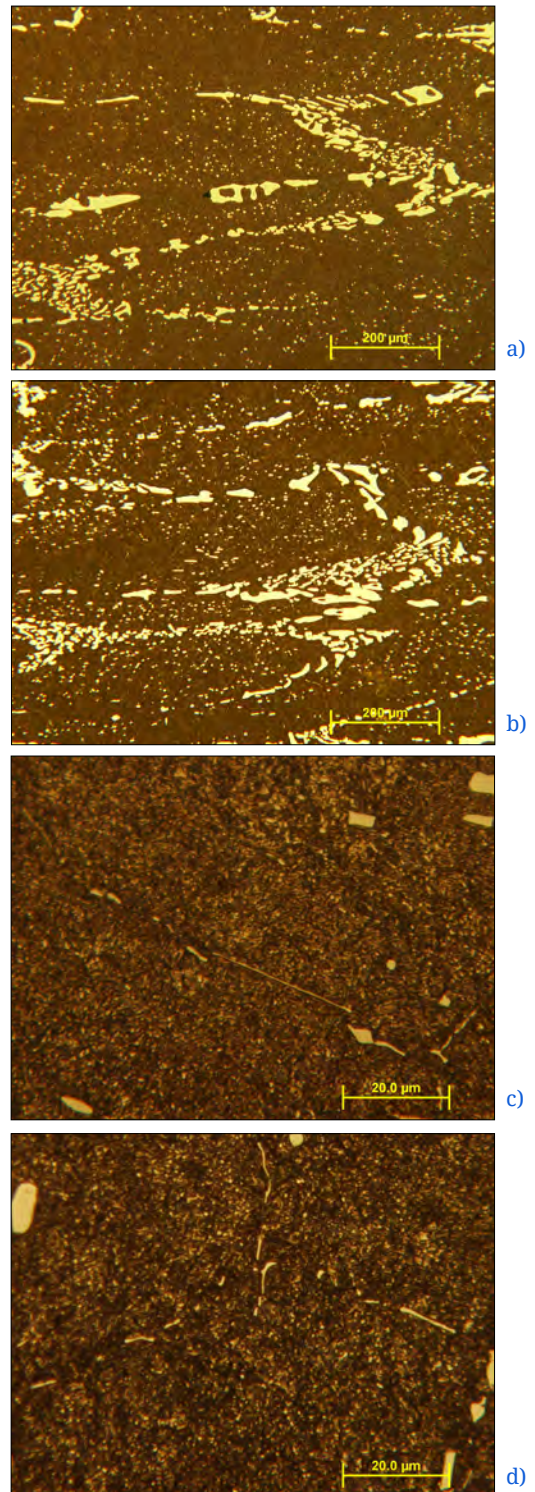


Figure 2. The effect of the hardening temperature on the microstructure; LOM image. Etching agent: Beraha-2. a) c) $T_{\text{aust}} = 1030 \text{ °C}$ b) d) $T_{\text{aust}} = 1070 \text{ °C}$

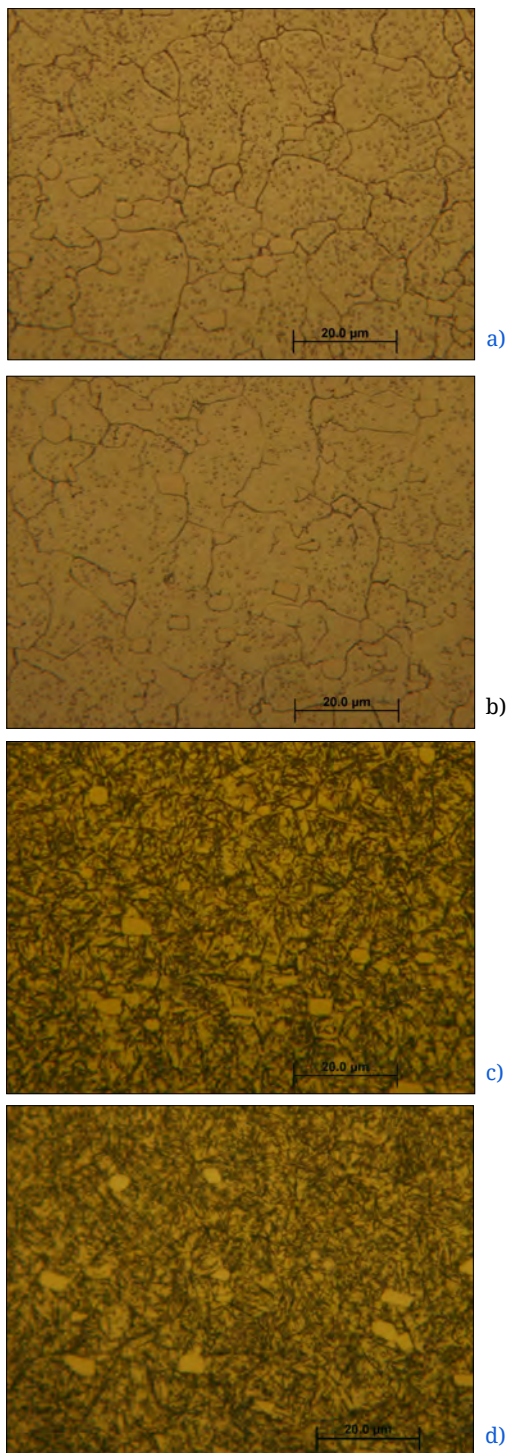


Figure 3. The effect of tempering temperature on microstructure; LOM images. $T_{Aust} = 1070\text{ }^{\circ}\text{C}$. Etching agent: 2% Nital. a) quenched, b) $T_{temper} = 200\text{ }^{\circ}\text{C}$, c) $T_{temper} = 520\text{ }^{\circ}\text{C}$, d) $T_{temper} = 520\text{ }^{\circ}\text{C} + 540\text{ }^{\circ}\text{C} + 500\text{ }^{\circ}\text{C}$

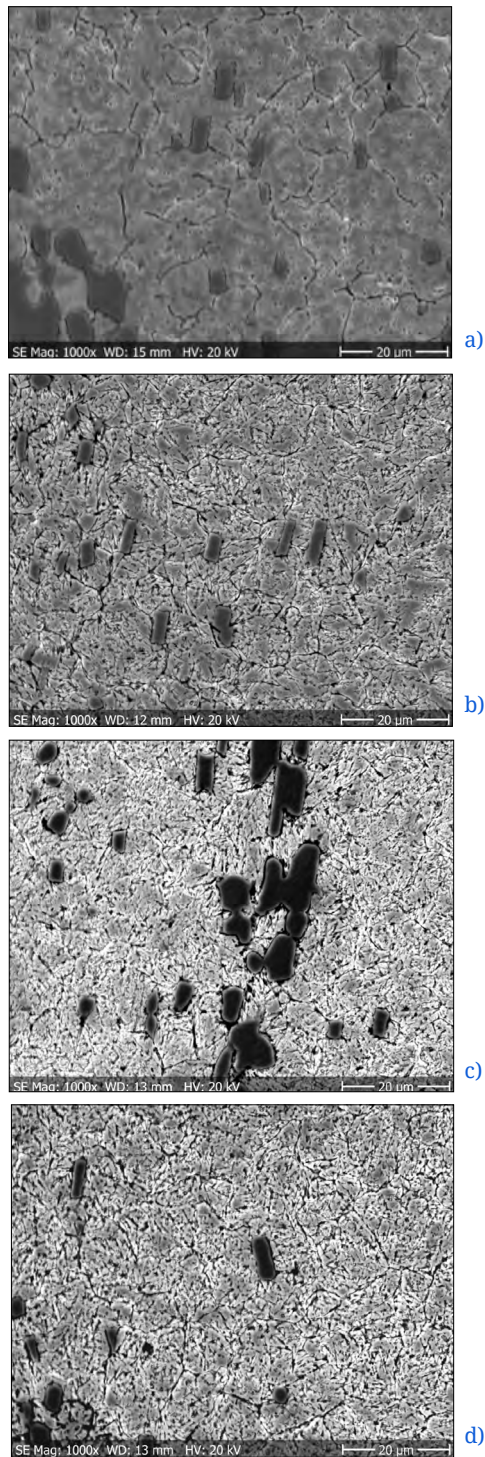


Figure 4. The effect of tempering temperature on microstructure. SEM images. Etching agent: 2% Nital. a) $T_{temper} = 200\text{ }^{\circ}\text{C}$, b) $T_{temper} = 520\text{ }^{\circ}\text{C}$, c) $T_{temper} = 520\text{ }^{\circ}\text{C} + 540\text{ }^{\circ}\text{C}$, d) $T_{temper} = 520\text{ }^{\circ}\text{C} + 540\text{ }^{\circ}\text{C} + 500\text{ }^{\circ}\text{C}$

in **Figure 3. b)**, **Figure 4. a)**) when the sample is tempered at 200 °C after quenching. After tempering at high temperature (520 °C) the result is fine dispersed carbides precipitations, but retained austenite can be detected as shown in the photos of **Figure 3. c)** and **Figure 4. b)** Multiple high-temperature tempering processes result in a higher quantity of fine, dispersed carbides in the microstructure while the residual austenite content decreases, as shown in the photos of **Figures 3. c), d)** and **4. c), d)** The characteristic of the primary carbides does not change significantly.

Changes in microstructure due to tempering at 500–550 °C increase the hardness of the matrix. Due to multiple tempering around 500–550 °C, the hardness of the matrix increased to 750 HV 1 (**Table 2.**).

3.3. The effect of cryogenic treatment

High-temperature tempering is required for tools that would be nitrided [1, 3]. Nitrided products typically require dimensional accuracy, so a large amount of residual austenite is not allowed. In our investigations it was found that the residual austenite content of the cryogenic treated workpiece is low even after a single high-temperature tempering process compared to the conventional treated sample (**Figure 5. a)**, **2. c)**). The triple high-temperature tempering process decreases the residual austenite content further (**Figure 5.**).

Due to cryogenic treatment the hardness of the matrix increase, and its positive effect on the wear factor is clearly demonstrated (**Table 3.**).

4. Conclusion

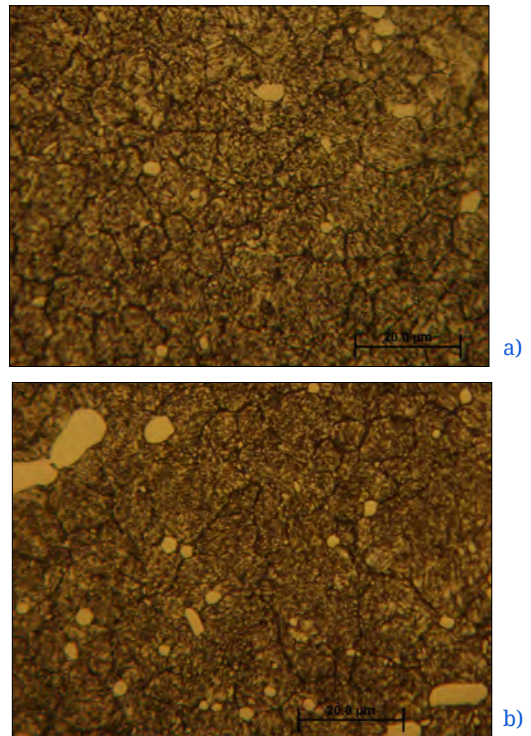
Increasing the austenitisation temperature reduces the hardness of the martensitic matrix after quenching due to the increasing amount of residual austenite. Multiple high-temperature tempering increases the hardness of the sample quenched from 1070 °C, partly due to the reduction of residual austenite content and partly due to the finely dispersed precipitates. Cryogenic treatment causes a good reduction in the amount of residual austenite and an increase in wear resistance.

Acknowledgments

The authors would like to thank the Hungarian state and the European Union for the financial support of our work in the framework of the project EFOP-3.6.1-16-2016-00010.

Table 3. The effect of deep cooling on matrix hardness and wear factor

Austenitisation (°C)	Cooling (°C)	Tempering (°C)			HV1 mátrix	Wear factor (mm ³ /N·m) K·
		T	T ₁	T ₂		
1070	20	510	–	–	663	4.29·10 ⁻⁵
1070	-80	510	–	–	746	2.66·10 ⁻⁵
1070	20	510	480	480	695	3.00·10 ⁻⁵
1070	-80	510	480	480	738	2.24·10 ⁻⁵



5. ábra. The effect of deep cooling on texture LOM images Etching: 2% nital, $T_{\text{quench}} = -80$ °C a) $T_{\text{temper}} = 510$ °C, b) $T_{\text{temper}} = 510$ °C + 480 °C + 480 °C

References

- [1] Smóling K., Czeglédi L.: *Szerszámacélok kézikönyve*. Szabvány Kiadó, Budapest, 1977. 94–95.
- [2] MSZ EN ISO 4957: 2018. *Szerszámacélok*
- [3] Voestalpine Böhler Edelstahl GmbH & Co KG: *Szerszámacélok, nemesacélok*, 45. <http://www.boehler.hu/media/productdb/downloads/K110DE.pdf> (accessed on: 2019. 01.28)
- [4] Inter Alloy Engineering Steels and Alloys: Product datasheets, Tool steel D22011 Inter-alloy Pty Ltd (accessed on: 2019. 02.15) <http://www.interalloy.com.au/our-products/tool-steel/d2-tool-steel-x153crm0v12>

- [5] Capdevila C. et al.: *Determination of Ms temperature in steels: A Bayesian Neural Network Model*. ISIJ International, 42. (2002) 894–902. <https://doi.org/10.2355/isijinternational.42.894>
- [6] Gavriljuk V. G., Theisen W., Sirosh V. V.: *Low-temperature martensitic transformation in tool steels in relation to their deep cryogenic treatment*. Acta Materiala, 61. (2013), 1705–1715. <https://doi.org/10.1016/j.actamat.2012.11.045>
- [7] Das D., Dutta A. K., Toppo V., Ray K. K.: *Effect of deep cryogenic treatment on the carbide precipitation and tribological behaviour of D2 steel*. Materials Manufacturing. Process, 22. (2007) 474–480. <https://doi.org/10.1080/10426910701235934>
- [8] Molinari A., Pellizzari M., Gialanella S., Straffelini G., Stiasny K. H.: *Effect of deep cryogenic treatment on the mechanical properties of tool steels*. Journal of Materials Processing Technology, 118. (2001) 350–355. [https://doi.org/10.1016/s0924-0136\(01\)00973-6](https://doi.org/10.1016/s0924-0136(01)00973-6)
- [9] Das D., Sarkar R., Dutta A. K., Ray K. K.: *Influence of sub-zero treatments on fracture toughness of AISI D2 steel*. Materials Science Engineering A, 528. (2010) 589–603. <https://doi.org/10.1016/j.msea.2010.09.057>
- [10] Das D., Dutta A. K., Ray K. K.: *Sub-zero treatments of AISI D2 steel: part II. Wear behaviour*. Materials Science and Engineering A, 527. (2010) 2194–2206. <https://doi.org/10.1016/j.msea.2009.10.071>
- [11] Kumar S., Nagaraj M., Khedkar N. K., Bongale A.: *Influence of deep cryogenic treatment on dry sliding wear behaviour of AISI D3 die steel*. Materials Research Express, 5/11. (2018) 116525, 1–9. <https://doi.org/10.1088/2053-1591/aadeba>
- [12] Kovács T., Dévényi L.: *Kopásvizsgálati eljárás fejlesztése*. Anyagok világa, 5/1. (2004). https://www.kfki.hu/~anyag/tartalom/2004/dec/05_KT_DL.pdf

Laser Cutting of Austenitic Corrosion-Resisting Steels

Gergely HALÁSZ,¹ Enikő Réka FÁBIÁN,² János KUTI³

Óbuda University, Budapest, Hungary

¹ gerryhalasz@gmail.com

² fabian.reka@bgk.uni-obuda.hu

³ kuti.janos@bgk.uni-obuda.hu

Abstract

Cutting of thick austenitic stainless steel sheets with a disc laser is not fully developed. In this research were investigated the surface of holes made on 3.25 mm thick stainless-steel cut with CO₂ laser beam and disk laser beam. Using optical microscope and electron microscope to examine the cutting surfaces, were observed that the cutting with the CO₂ laser result high quality surface (cutting 3,25 mm thick plates), but holes made with solid-state laser has microcracks on the inner side. These cracks are not acceptable to the customers.

Keywords: *laser cutting, austenitic steel, CO₂ laser, solid-state laser.*

1. Introduction

One of the great achievements of the 20th century was the discovery of the laser that opened new perspectives in many disciplines. The great advantage of lasers used in the material processing is that the process provides very precise, quick machining and low heat input, but all machining requires unique parameters. These parameters are for example: Power, wavelength, cutting speed, focus line distance. Many researchers have been involved in cutting with CO₂ laser. The laser cutting of austenitic stainless steels above a certain thickness is not fully developed. In recent years, the increase in the power of fiber lasers has resulted the possibility of the cutting of higher-thickness stainless steel sheet, Seon and his associates succeed in cutting a 60 mm thick sheet with a 9 kW laser, but the surface is very drossy [1]. A particular problem is the curved cutting of thick steels [2, 3]. In addition to laser power, Berkmanns and Faerber examined the effect of curvature on cut surface quality [2]. Parthiban and his associates achieved a curved surface with sufficient quality, on 2.5 mm thick on X5CrNi18-10 type material with CO₂ laser beam [3].

Kotadiya and his associates studied the effects

of the laser beam cutting parameters on surface roughness. The authors found that both laser power and gas pressure significantly affect the surface roughness using CO₂ laser source [4], but in the case of fiber laser beam, power and cutting speed are decisive for corrosion-resistant steels [5].

The quality requirements for the surface of the laser-cut holes depends on the use of the parts. The part I have tested must meet very stringent requirements, because it will be used in gas turbines. The cuts were made with CO₂ laser and solid-state laser. For the CO₂ laser, we used the company-approved reference parameters, while for the solid state laser, we used the parameters of our choice, as the proper values for the process variables are not yet worked out. In the case of CO₂ laser cutting, the surface of the cut was as specified, but with regard to solid laser cutting, the number of cracks exceeded the maximum amount of cracks specified by the customer. The aim of our research is to examine the surface of holes made during trial cuts and to evaluate the set parameters.

2. The laser

Considering the laser as radiation, it is based on stimulated emission that occurs in the laser medium when a photon strikes an already excited state atom and the incoming photon captures the excited atom's photon, and collectively moving on, the arrival going parallel to its direction. The laser beam is generated in the resonator, where the laser medium, the pump, the closing and the semipermeable mirrors are located. The laser medium may also be a solid, liquid or gas medium. The basic condition of the stimulated emission is that there should be more atoms in excited state than in non-excited state, this is called Population inversion. [6]

2.1. The CO₂ laser

One of the most common lasers used in the industry was the CO₂ laser, which was mainly used for cutting and welding. The first used high-performance industrial lasers were CO₂ lasers. The laser medium in this case is a gas mixture which flows in quartz glass tubes. To excite the gas without contact they use electrodes from outside of the tubes. The used laser gas is a gas mixture that is blended with carbon dioxide, helium and nitrogen in an appropriate proportion. The wavelength of the created laser beam/laser radiation: $\lambda = 10,6 \mu\text{m}$. [7]

2.2. The fiber laser

The fiber-laser is a very complex but powerful solid-state laser which were designed to circumvent the unfavorable excitation properties of rod lasers. It is a solid-state laser as the laser medium is a solid quartz glass contaminated with rare earth metals, in which the high-power laser beam is generated by excitation of the polluting atoms. The medium is a thin fiber which is 8–10 μm diameter, this core has the largest refractive index, surrounded by a coating with a lower refractive index. The low-power pump laser beam (diode laser) that will perform the excitation is propagates in the coating. The outer cladding, which has the smallest refractive index, ensures that the excitation laser does not get out. The excitation laser easily enters the core, but it can not get out so easily, and the laser created by the induced emission is almost impossible to get out. In this case for the laser beam mirroring they use Bragg grating instead of mirrors. This grating are placed perpendicularly to the optical axis on the two end of the core. In these bands (grid lines), the refractive index differs from the core refractive index, and the bands thickness are periodically variable. [7]

2.3. The disk laser

The disk laser uses a thin circular disk as a medium instead of a thin fiber. The excitation diode laser which guided through the laser medium in several times with mirrors, causing the population inversion, the excited laser beam then exits from the resonator and can be led by an optical cable. The quality of the laser beam produced in this way achieves the quality of the CO₂ laser and provides greater efficiency, and also has the great advantage of the fiber laser being used to transmit the beam with an optical cable. The Disk laser wavelength $\lambda \approx 1 \mu\text{m}$ which means that it is smaller than a CO₂ laser [7], and it plays an important role in heat input and has a decisive influence on the results of the sample. The parameters that we used have been adjusted to this effect.

3. Description of the experiments

The test material is austenitic stainless steel of type X5CrNi18-10. The test cuts were made on a 3.25 mm thick plate. The first reference cut is a 4 kW CO₂ laser of the Truflow 4000 type, while the other cuts were made with a TruDisk 3000 type 3 kW disk laser. The surface of the holes was first inspected visually after the cuts, and then the inner surface of the holes and the rim using a Dino-Lite Digital portable light microscope. The detailed examination of the laser-cut surfaces and possible defects were examined with a Jeol JSM 5310 scanning electron microscope (SEM).

4. Test results

First, we made images of the holes surfaces using a simple portable light microscope to provide the basis for the future studies. These images clearly show the laser beam entry / exit point, focus spot location and spattering on the edges of the cut, and the so-called "adherent slag" on the bottom edge of the hole, but the cracks in these images are not visible.

The "adherent slag", as shown in [Figure 1](#). was typically visible on the surface of the hole cut with the CO₂ laser. For these cuts, were used the reference parameters previously accepted by the company, which are used to make existing parts. The metallographic pattern shows a uniform melting zone of about 40 μm ([Figure 2.](#)), which in some cases overflowed in approximately the same degree with the direction of cutting. In contrast, the disc laser-cut pieces did not exhibit this amount of adherent slag. At first glance, the edge of the cut is rough, but the roughness of its inner surface is



Figure 1. Adherent iron-oxide on the hole surface cut with CO₂ laser (∅ 6,2 hole)

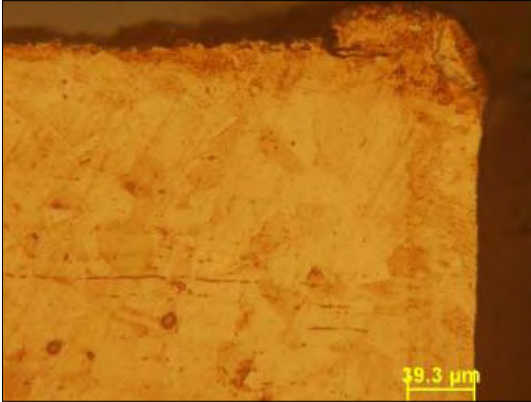


Figure 2. Near the hole surface area after CO₂ laser beam cutting. Etching material: aqua regia

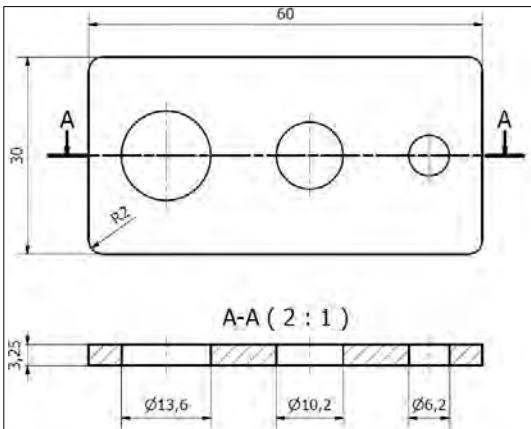


Figure 3. Cutted sample geometry



Figure 4. Hole made with Disk laser (∅ 13,6 hole)

adequate. The reference cut was followed by the cutting with a disc laser. During the test cuts, we changed the parameters by reducing the energy intake. The holes shown in **Figure 3.** were made with different speeds and power. Because of the much smaller wavelength, the heat absorbed by the material was higher when using similar parameters, so the disc laser cut was significantly faster. This is very important for productivity. On the test pieces, it can be clearly seen that the quality of the hole edge is much better, the quality of the piece during the visual inspection was far superior to the quality of the reference piece. However, some parameters also had splashes. **Figure 4.** clearly shows the surface quality of the hole, with no splashes or adherent slag is visible on it. The thickness of the melt layer is below the 60μm permissible value. This is also evidenced by the metallographic image of the hole shown in **Figure 5.** For visual inspection, both the rim and the surface of the hole are suitable. However, with reduced performance, spatter appeared on the surface. Lower power cuts resulted a significant amount of post-work removable splattering.

The cutting gas was not able to properly blow out the melt everywhere, causing spatter. The result of this shown in **Figures 6.** By changing the focus distance, a drastic reduction in hole surface quality can be seen in **Figure 7.** It can be seen that the roughness of the surface has increased, and spatter has appeared on both the hole edge and the surface of the sample.

In total, visual inspection and light microscopy show that the surface roughness of most of the holes made with a disc laser is lower than that of the holes made with CO₂ laser, but since these components will be expose to cyclic heat load, the result of light microscopy is not enough, because

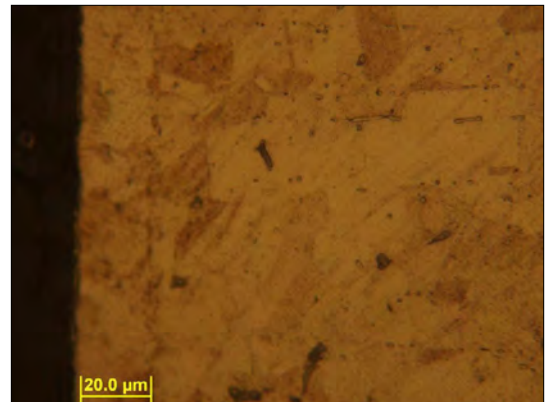


Figure 5. Melted zone of the hole cut with disc laser

the microcracks are not detectable with it, so in the following I took pictures with a much higher resolution and depth of field scanning electron microscope. The holes were cut with water jet cutting to minimize heat input. The surface of the cut holes was ready to be examined under a scanning electron microscope, which is capable of producing images of much larger magnification and resolution. High-resolution images can also detect segregation, cracks, and material defects that are not visible under a light microscope.

These pictures show that the holes made with the disc laser has a high quality on the outside



Figure 6. Spatter on the rim of the laser cut hole in the disc (\varnothing 6,2 hole)



Figure 7. The cut made with disc laser, with changed focus distance from the centerline (\varnothing 13,6 hole)

but has a small and dangerous defect. There are microcracks transverse to the surface of the hole centerline. Such defects can propagate under cyclic heat stress and can even lead to component failure. We also found cracks in the cuts made by the CO_2 laser, but they are so small and so few that they are within the tolerances specified by the customer. However, in the case of disk laser, the number of cracks is above the value accepted for a CO_2 laser, so these cuts do not correspond. **Figure 8.** clearly shows that there is a relatively large number of cracks on the surface of the remelted zone, all transversely located, often at the center of the sheet thickness.

To determine the length and width of the cracks, I took pictures at a higher magnification. **Figure 9.** clearly shows that the length of the cracks ranges from 30 to 80 μm and their width is from 2 to 4 μm .

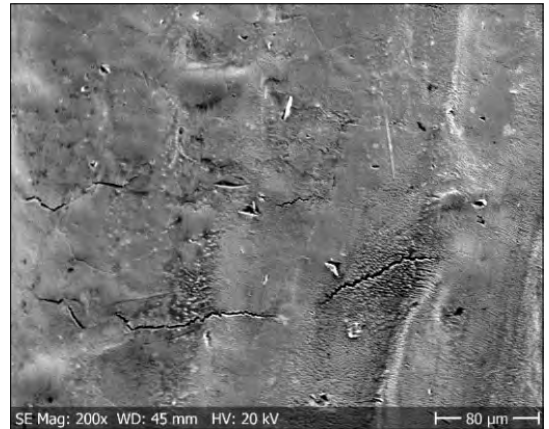


Figure 8. Cracks on the surface of the cut after cutting with disc laser (SEM recording)

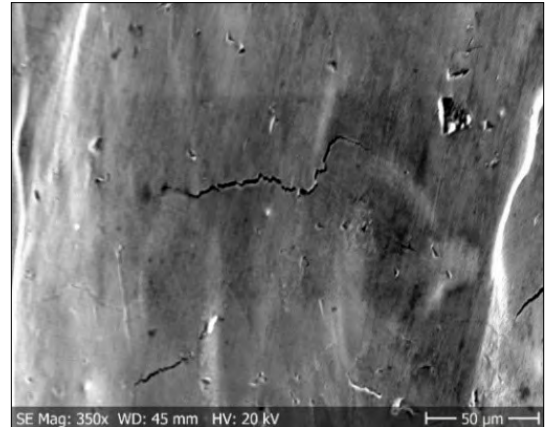


Figure 9. Cracks on the surface of the cut after cutting with Disk laser (SEM recording)

Images of the cuts examined by electron microscopy show a similar tendency, with cracks between 30 and 100 μm in length and 2–4 μm in width. However, the depth of the cracks cannot be determined from microscopic images. So far, only CO₂ laser cuts and a disc laser variable has been investigated. Further destructive material testing of the other process variables will also be performed. Based on the available data and the literature, I was able to determine the cause of the cracks.

Referring to the literature, one of the possible cause of cracks appearing on laser-cut surfaces is the formation of layers formed during the rolling of the raw material, which would explain the transverse cracks perpendicular to the holes in the bore. However, in higher magnification, it became apparent that the cracks are essentially fragmented (Figures 8. to 9.) and are not bound to a certain zone in the case of disk laser cutting, but are scattered across the entire surface of the hole so the probability of this option is low.

The second option is the so-called liquation cracking. John C. Lippold [8, 9] dealt with this topic in depth. In highly alloyed materials may can forming of different types of carbides in the partially melted zone during welding or cutting, depending on the composition of the raw material. These carbides, such as niobium carbide, titanium carbide, or chromium carbide, have a higher melting point than the material around them, so carbides are not melted in the partially melted zone they cause cracks in the melt during solidification, but neither the Nb nor Ti are present in the material we investigate, the chromium carbide precipitation may appear as the rightmost crack in Figure 8, but typically the carbide characteristic was not detected in the cracks. in Austenitic steels if the seam ferrite content it reaches 5-10% usually no cracks occur if the heat input is not too high and the surface is not concave [10], but unfortunately there is no consumables in our samples, the surface is concave, and we have high nitrogen intake which is austenite formation.

Most of the cracks on the surface of the holes were in the middle zone of the sheet thickness, so the shrinkage of the molten zone during cooling may play an important role.

5. Summary

On the basis of the examinations it can be stated that the holes made by disc laser were visually superior, the melt zone thickness was less than

40 μm in all samples, but no cracks was found during the metallographic examinations. Only scanning electron microscope shows the presence of cracks. The surface and edge of the hole made with CO₂ laser were of lesser quality, but there were no micro-cracks on the surface of the hole. Although it looks inferior in quality to visual inspection, on the surface of the hole is much less crack can be seen. Spatter and adherent slag can be eliminated with minimal post-working.

Parameter modifications can reduce heat input when using a disk laser to achieve a better surface quality, but to reduce the amount of micro-crack by the modified parameters requires additional testing. On the basis of the present studies, it has been found that components made by a CO₂ laser for industrial use can be used with the present parameters.

Acknowledgments

We would like to thank the Hungarian State and the European Union for their financial support for our work under the EFOP-3.6.1-16-2016-00010 project.

References

- [1] Seon S., Shin J. S., Oh S. J., Park H., Chung C.-M., Kim T.-S., Lee L., Lee J.: *Improvement of cutting performance for thick stainless steel plates by step-like cutting speed increase in high-power fiber laser cutting*. Optics and Laser Technology, 103. (2018) 312–317. <https://doi.org/10.1016/j.optlastec.2018.01.054>
- [2] Berkmanns J., Faerber M.: *Facts about laser cutting*. Höllriegelskreuth, Németország, 2003. 4–15. <http://www.laserdeal.com/techInfoFiles/Facts%20about%20Laser%20Cutting%20eng-1%5B1%5D.%20Drucklayout%2023.06.03.pdf> (accessed on: 2019.08.30)
- [3] Parthiban A., Chandrasekaran M., Muthuraman V., Sathish S.: *Optimization of CO₂ Laser Cutting of Stainless Steel Sheet for Curved Profile*, ICAFM, 2017. 14531–14538. <https://doi.org/10.1016/j.matpr.2018.03.042>
- [4] Kotadiya D. J., Pandya D. H.: *Parametric analysis of laser machining with response surface method on SS-304*. ICIAME, 2016. 376–382. <https://doi.org/10.1016/j.protcy.2016.03.040>
- [5] Kotadiya D. J., Kapopara J. M., Patel A. R., Dalwadi C. G., Pandya D. H.: *Parametric analysis of process parameter for Laser cutting process on SS-304*. IC-MPC, 2017. 5384–5390. <https://doi.org/10.1016/j.matpr.2017.12.124>
- [6] Buza G.: *Lézersugaras technológiák I*. Edutus Főiskola, 2012. 4–65.
- [7] Leibinger-Kammüller N.: *The Laser as a tool*. TRUMPF GmbH + Co., Ditzingen, 2007.

- [8] Lippold J. C.: *Welding Metallurgy and Weldability*. John Wiley & Sons, Inc., Ohio, 2015. 119–130.
- [9] Lippold J. C., Kotecki D. J.: *Welding Metallurgy and Weldability of Stainless Steels*. Wiley, 2014.
- [10] International Molybdenum Association: *Practical Guidelines for the Fabrication of High Performance Austenitic Stainless Steels*, I.M.O.A. Co-published with Cricda, ISBN 978-1-907470-10-3. 46
https://www.imoa.info/download_files/stainless-steel/Austenitics.pdf

Investigation of Milling of Carbon Fiber Reinforced Plastic

Richárd HORVÁTH,¹ Róbert Gábor STADLER, Kristóf ANDRÁSFALVY

Óbuda University, Donát Bánki Mechanical and Safety Engineering, Budapest, Hungary

¹ horvath.richard@bgk.uni-obuda.hu

Abstract

The use of fiber-reinforced plastics has increased significantly in the past decades. Consequently, the demand for finishing and machining of such materials has also escalated. During machining, the fiber-reinforced materials exhibit machining problems dissimilar to the problems of metals. These are fiber pull-out, fiber breakage in the cutting zone, matrix smearing and delamination. The purpose of this experiment is to investigate the characteristics of the resultant force (F_e) during the milling of carbon fiber reinforced plastic as a function of input machining parameters. For the force measurements, CFR with perpendicular (0° – 90°) fiber orientation was machined. The experimental design involved the central composite design method. To analyze and evaluate the measurements, we applied the response surface methodology.

Keywords: milling, cutting force, central composite design, RSM method.

1. Introduction

Fiber-reinforced composites belong to a new generation of engineering materials. Thanks to their excellent mechanical properties, the use of fiber-reinforced materials (e.g. glass or carbon fiber) is increasing rapidly. One of the greatest users is the aviation industry. **Figure 1.** shows the increasing amount of carbon fiber reinforced composites used in the airframes of airplanes **[1]**. Next generation airplanes will be designed to have more than 50% composites. This reduces fuel consumption and carbon dioxide emissions by 20–25% **[2]**.

The final step in producing a carbon fiber reinforced composite product may be machining. During preliminary process planning it is important to know what cutting forces will be encountered as a function of cutting parameters, and how these forces will affect the part and the tool. For this reason, the cutting of carbon fiber-reinforced plastics is a much-researched topic.

Meltem and Hasan wrote a comprehensive study on the machinability of carbon fiber reinforced polymers **[3]** in 2018. They reviewed recent publications on the traditional machining techniques of composites (turning, milling, drilling etc.). Based on the literature, they drew the following conclusions:

- increased feed rate results in greater force;
 - the least amount of delamination can be achieved with a low cutting speed and a low feed rate;
 - for the lowest average surface roughness, a high cutting speed and a low feed rate are required.
- Mathivanan et al. **[4]** examined the machinability of glass fiber reinforced (GFRP) and carbon fiber reinforced (CFRP) plastics while closed groove milling. The fibers were laid perpendicular to each other in the workpiece. In the cutting experiment (nine measurement points) they used

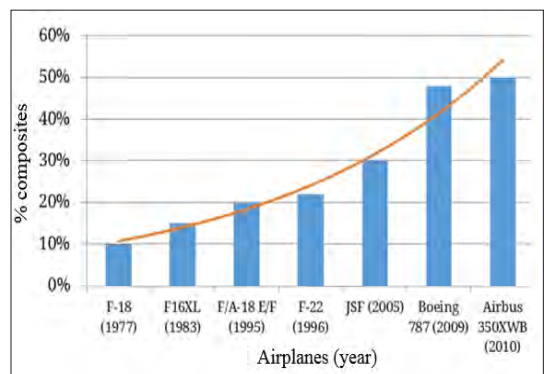


Figure 1. The proportion of composites in the airframe of airplanes

Ø 10 mm K10 hard metal milling tool, and varied cutting parameters (cutting speed and feed per tooth) on three levels. They investigated the resultant force and found that feed increased it most. They recommend low feed and high cutting speed for the cutting of such materials.

Haijin et al. [5] milled carbon fiber reinforced plastic. They measured the force and temperature during cutting. They used the central composite design method, and applied the response surface methodology (RSM) in the analysis of the results. Their input parameters were cutting speed, feed rate and depth of cut. They found that resultant force was most influenced by feed rate, while temperature is most affected by cutting speed.

Çolak and Sunar [6] milled a carbon fiber reinforced composite consisting of 32 laminated layers. They used a ϕ 10 mm PCD tool and varied cutting speed on two levels (50 m/min and 100 m/min), and feed per tooth on five levels (0.050, 0.075, 0.100, 0.125 and 0.150 mm). In the experiments, they measured all three force components and surface roughness. They found that a smaller cutting force can be achieved with higher cutting speeds and lower feed rates, while surface roughness (Ra) is impaired as feed rate is increased and cutting speed is lowered.

Yanli et al. [7] examined the force during milling and delamination as a function of fiber orientation, cutting speed and feed rate. They milled a composite reinforced by 43 layers of unidirectional carbon fiber (TC35-12K / 150) at 0, 45, 90 and 135 degrees. The thickness of the laminated composite was 6 mm and the volume fraction of the fibers was approximately 60%. They varied cutting speed and feed rate on three levels. An ϕ 8mm milling tool was used in the experiments. They analyzed how cutting force components depend on fiber orientation. They also investigated delamination in detail.

Erol Kiliçkap et al. [8] milled a composite reinforced with 16 layers of carbon fiber. The fibers were perpendicular to each other. They used two hard metal milling tools (3-tooth and 4-tooth). They used three cutting speeds (31.4, 62.8 and 94.2 m/min) and three feed rates (100, 150 and 200 mm/min), while they kept depth of cut at a constant 1.5 mm. During milling, they measured the force components, the surface roughness of the milled surfaces and delamination phenomena on the surface. They found that as feed increases, the resultant force increases too. They got better results with the tool with 4 teeth.

Geier N. and Szalay T. [9] drilled and spiral milled

a carbon fiber reinforced composite. The drill bit was a special SECO SD205A-11.138-53-12R1-C1, diamond-coated bit, while they performed milling with a TIVOLY 8236651 1000 hard metal end mill. They measured the force components during cutting, and also the milled surfaces and the surface roughness of the holes. They also examined de-lamination on the machined surfaces. They used a design of experiments and did 13 drilling and 20 milling experiments. They analyzed the results with the ANOVA method. They varied the process parameters of cutting on five levels in the case of both cutting processes. Cutting speed in drilling was 50, 65, 100, 135 and 150 m/min and feed per tooth was 0.035, 0.043, 0.064, 0.078 and 0.093 mm. During milling, cutting speed was 50, 70, 100, 130 and 150 m/min) feed was 0.020, 0.028, 0.040, 0.051 and 0.060 mm, and pitch for milling was 0.100, 0.068, 1.550, 2.410 and 3.000 mm). They determined the ideal process parameters, and also found that a hard metal milling bit produced better quality bores than a diamond-coated bit.

We milled a carbon fiber reinforced composite and measured the force components, and analyzed the resultant force. We examined the effect of cutting process parameters on the resultant force.

We built a predictive model, with which the resultant force can be estimated with adequate accuracy in preliminary process planning, as most defects and the properties of the part (e.g. delamination, dimensional inaccuracy, fiber breakage in the cutting zone, fiber pull-out, surface roughness values) greatly depend on cutting force.

2. Materials and methods

2.1. The material and tool used in the experiment

We milled a 26-layer (10 mm thick) carbon fiber reinforced composite produced by vacuum infusion. The carbon fiber was Zoltek Panex 35. Its aerial density is 400 g/m², its tensile strength is 4137 MPa, its modulus of elasticity is 242 GPa, and the diameter of the fibers is 7.2. The epoxy resin used was Araldite LY 1564, and the curing agent was Aradur 3487. Their proportion was 100 g resin/34 g curing agent.

The composite was cross-ply laminated (Figure 2.). We used a ϕ 10mm D-POWER GUF40100 end mill, which is specially designed to mill fiber-reinforced composites. A great advantage of this tool is that it reduces the moving of layers away from each other.

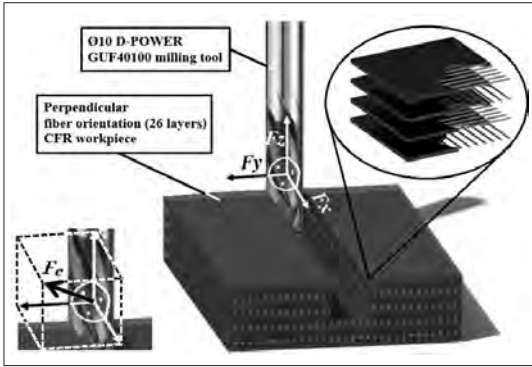


Figure 2. Layout of the cutting experiment, and the direction of the force components

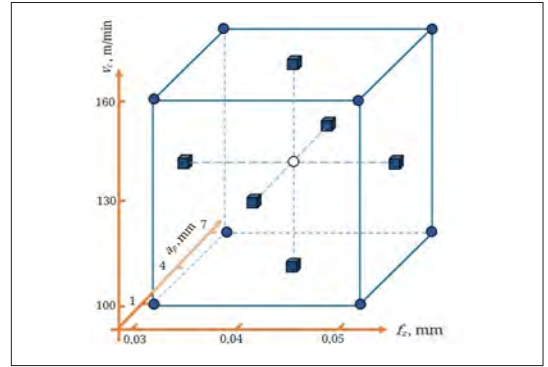


Figure 3. The points of experiment in the cutting parameter space

2.2. The measuring instruments used and the measured parameters

We performed the milling experiments on a Mazak Nexus 410A-II machining center. Force was measured with a piezoelectric KISTLER 9257b dynamometer. We measured the F_x , F_y and F_z force components. The range of the dynamometer is $F_x = F_y = -5...5$ kN, and $F_z = -5...10$ kN. The measured force components were analyzed with the Kistler DynoWare software. The tool and the workpiece are affected by the resultant force (Figure 1.), therefore we examined the resultant force (F_e):

$$F_e = \sqrt{F_x^2 + F_y^2 + F_z^2} \tag{1}$$

2.3. The Design of Experiments

We used the central composite design method in the milling experiments. Input variables (cutting speed and feed per tooth, depth of cut) were varied on three levels. We evaluated the data with the response surface methodology. The levels are equidistant from each other (Table 1., Figure 3.). The measured output variable is the resultant force (F_e). We sought to find a relationship between the independent input variables x_1 , x_2 , x_3 and the dependent output variable Y :

$$Y = \Omega(x_1, x_2, x_3) \tag{2}$$

Table 1. The values of input parameters

Process parameters		Level		
		-1	0	1
x_1	cutting speed – v_c , m/min	100	130	160
x_2	feed – f_s , mm	0.03	0.04	0.05
x_3	depth of cut – a_p , mm	1	4	7

where Ω is the response function, which can be written in the following general form:

$$Y = b_0 + b_1 \cdot x_1 + b_2 \cdot x_2 + b_3 \cdot x_3 + b_{11} \cdot x_1^2 + b_{22} \cdot x_2^2 + b_{33} \cdot x_3^2 + b_{12} \cdot x_1 \cdot x_2 + b_{13} \cdot x_1 \cdot x_3 + b_{23} \cdot x_2 \cdot x_3 + \epsilon \tag{3}$$

where b_0 , b_i and b_{ij} are the calculated coefficients, x_1 , x_2 and x_3 are the input variables and ϵ is the error. Model (3) takes into account input process parameters, their second-order components, and if they have a significant effect, then the cross-effects of the input process parameters as well.

2.4. The measurement points of the design of experiments

We set the cutting parameters and their level based on the literature and the recommendations of the tool catalogue (Table 1.).

Figure 3. shows the measurement points on the cutting parameter range based on Table 1. Based on the design of experiments, we milled the specimen at the factorial points and axis points of the cube once, and six times with the process parameters at the center of the cube.

The points of experiment and their parameters can be found in Table 2.

3. Results

3.1. The effect of cutting process parameters on the resultant force

Figure 4. shows the main effect plots obtained from the results.

The main effect plots show that increasing feed per tooth and increasing depth of cut increase the resultant force.

Table 2. The calculated and measured resultant forces in the 20 measurement points

Experimental runs	v_c m/min	f_z mm	a_p mm	F_e^e N (measured)	F_e^c N (calculated)
1.	100	0.03	1	26.57	22.83
2.	160	0.03	1	18.95	21.70
3.	130	0.04	1	21.03	26.07
4.	100	0.05	1	33.95	30.45
5.	160	0.05	1	31.17	29.32
6.	130	0.03	4	99.32	97.04
7.	100	0.04	4	117.31	123.17
8.	160	0.04	4	114.24	122.04
9.	130	0.04	4	133.70	122.61
10.	130	0.04	4	131.05	122.61
11.	130	0.04	4	127.07	122.61
12.	130	0.04	4	122.48	122.61
13.	130	0.04	4	118.16	122.61
14.	130	0.04	4	124.19	122.61
15.	130	0.05	4	142.72	148.18
16.	100	0.03	7	173.24	172.38
17.	160	0.03	7	174.36	171.25
18.	130	0.04	7	208.12	219.14
19.	100	0.05	7	267.26	267.03
20.	160	0.05	7	273.99	265.90

3.2. A predictive model to estimate the resultant cutting force

Table 3. shows which cutting parameters had a significant effect on the resultant force (the linear components of input process parameters re-main in the model irrespective of their significance).

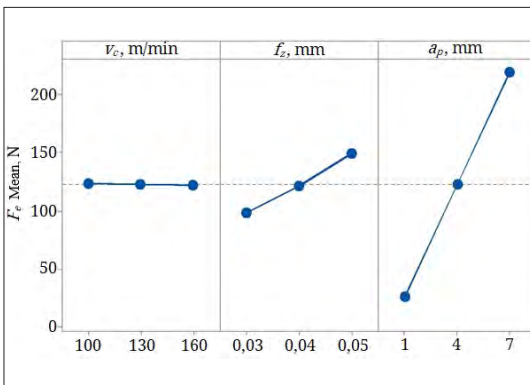
Table 3. The result of the significance test (✓ – the process parameter has a significant effect on the resultant force, ✗ – the process parameter does not affect the result-ant force)

Cutting parameters	
v_c	✓
f_z	✓
a_p	✓
v_c^2	✗
f_z^2	✗
a_p^2	✗
$v_c \cdot f_z$	✗
$v_c \cdot a_p$	✗
$f_z \cdot a_p$	✓

After the significance test, we built the following predictive model from the factors affecting the resultant cutting force:

$$F_e = 10,1 - 0,0188 \cdot v_c - 344 \cdot f_z + 3,17 \cdot a_p + 725,2 \cdot f_z \cdot a_p \tag{4}$$

Figure 5. shows the effects of process parameters on the resultant force graphically. It clearly shows that minimal cutting force is obtained when feed and depth of cut are lowest.



4. ábra. A forgácsolási folyamatváltozók hatása az eredő erőre

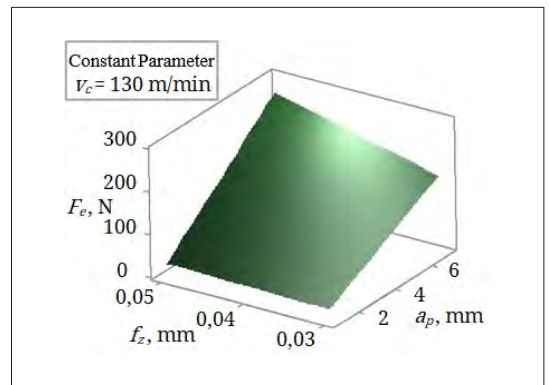


Figure 5. The graphical representation of the predictive model (4)

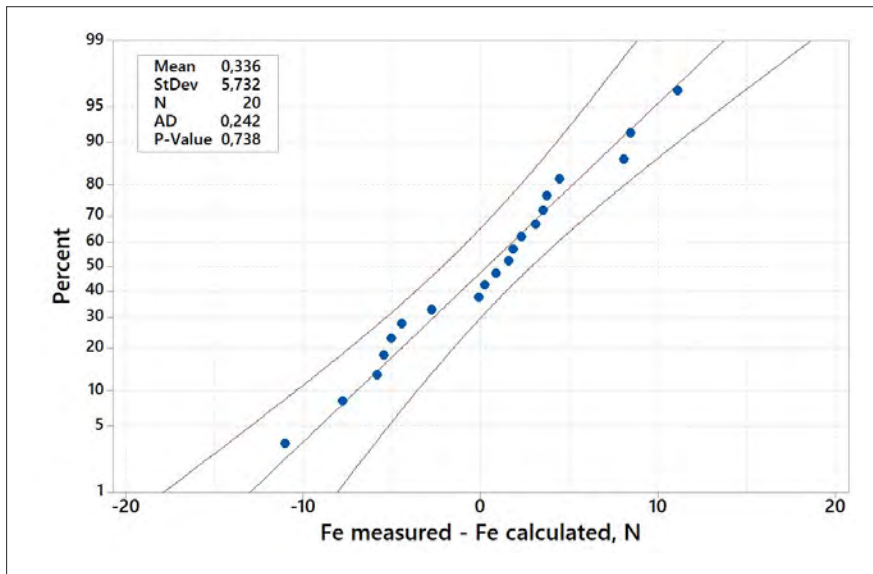


Figure 6. The residuals of measured and calculated results on the probability plots

The predictive model can be considered adequate in preliminary process planning if the expected value of the residuals (the difference between the measured and calculated values) are near zero and the standard deviation of the residuals is as low as possible. **Figure 6.** shows the differences of the measured and calculated results on a probability plots. It is clearly visible that in estimating the resultant force, the expected value of the errors is near zero, the distribution of the errors approximates normal distribution well and their standard distribution is $\pm 5,7$ N.

4. Conclusions

We investigated the milling of a carbon fiber reinforced composite with the central composite design method. We used three levels of the cutting process parameters (cutting speed, feed per tooth and depth of cut), measured the cutting force components and examined the resultant force. We analyzed the effect of the cutting process parameters on the examined characteristics with main effect plots and made a predictive model to estimate the resultant cutting force as it can help preliminary process planning. Based on our experiments, we can draw the following conclusions:

- cutting speed has the least (negligible) effect on the resultant cutting force;
- increasing feed and depth of cut increases the resultant cutting force;

- depth of cut has the greatest effect on the resultant cutting force;

We built a predictive model to estimate the resultant force in the examined range of cutting process parameters. The model can estimate the resultant force with a standard deviation of $\pm 5,7$ N.

Acknowledgements

The authors would like to thank KANDSI Kft. (AKO-BEZ) for providing the custom-made specimens, and GranTOOL Kft. for providing the tool for the tests. This project was supported by the New National Excellence Program (ÚNKP-2018-1-I) of the Ministry of Human Resources.

References

- [1] Hashish M., Kent W. A.: *Trimming of CFRP aircraft components*. In: WJTA-IMCA conference and Expo, 2013. September
- [2] Timmis A. J., Hodzic A., Koh L., Bonner M., Soutis C., Schäfer A. W., Dray L.: *Environmental impact assessment of aviation emission reduction through the implementation of composite materials*. The International Journal of Life Cycle Assessment, 20/2. (2015) 233–243. <https://doi.org/10.1007/s11367-014-0824-0>
- [3] Karataş M. A., Gökkaya H.: *A review on machinability of carbon fiber reinforced polymer (CFRP) and glass fiber reinforced polymer (GFRP) composite materials*. Defence Technology, 14/4. (2018) 318–326. <https://doi.org/10.1016/j.dt.2018.02.001>

- [4] Mathivanan N. R., Mahesh B. S., Shetty, H. A.: *An experimental investigation on the process parameters influencing machining forces during milling of carbon and glass fiber laminates*. Measurement, 91. (2016) 39–45. <https://doi.org/10.1016/j.measurement.2016.04.077>
- [5] Wang H., Sun J., Li J., Lu L., Li N.: *Evaluation of cutting force and cutting temperature in milling carbon fiber-reinforced polymer composites*. The International Journal of Advanced Manufacturing Technology, 82. (2016) 9–12. 1517–1525. <https://doi.org/10.1007/s00170-015-7479-2>
- [6] Çolak O., Sunar T.: *Cutting forces and 3D surface analysis of CFRP milling with PCD cutting tools*. Procedia CIRP, 45. (2016) 75–78. <https://doi.org/10.1016/j.procir.2016.03.091>
- [7] He Y., Qing H., Zhang S., Wang D., & Zhu S.: *The cutting force and defect analysis in milling of carbon fiber-reinforced polymer (CFRP) composite*. The International Journal of Advanced Manufacturing Technology, 93/5–8. (2017) 1829–1842. <https://doi.org/10.1007/s00170-017-0613-6>
- [8] Kiliçkap E., Yardımeden A., Çelik Y. H.: *Investigation of experimental study of end milling of CFRP composite*. Science and Engineering of Composite Materials, 22/1. (2015) 89–95. <https://doi.org/10.1515/secm-2013-0143>
- [9] Geier N., Szalay T.: *Optimisation of process parameters for the orbital and conventional drilling of uni-directional carbon fibre-reinforced polymers (UD-CFRP)*. Measurement, 110. (2017) 319–334. <https://doi.org/10.1016/j.measurement.2017.07.007>

Development of a Composite Material for Impact Load

Tünde Anna KOVÁCS,¹ Zoltán NYIKES,² Lucia FIGULI³

¹Óbuda University, Donát Bánki Mechanical and Safety Engineering, Department of Materials Technology, Budapest, Hungary, kovacs.tunde@bgk.uni-obuda.hu

²Óbuda University, Doctoral School on Safety and Security Sciences, Budapest, Hungary, nyikes.zoltan@phd.uni-obuda.hu

³University of Zilina, Faculty of Security Engineering, Department of Technical Sciences and Informatics, Zilina, Slovak Republic, lucia.figuli@fb.i.uniza.sk

Abstract

The goal of this work was to invent a high energy absorbing composite material. This composite needs to be able to attach on the building's surfaces and increase blast-resistance. In this innovation, the test samples were reinforced with aramidfiber, glass fiber and carbon fiber and tested by Charpy pendulum impact testing machine. During the tests, the aramid and glass fiber reinforced composites showed good resistance and high energy absorption against impact load.

Keywords: *composite, impact load, blast-resistant material.*

1. Introduction

In every century, we can find guns and fencing, in the countries affected by war or terrorism. With the development of materials science and technology, weapons and defence methods have developed too. In our modern times, we are threatened not only by more traditional conflict but also by terrorism.

Terror attacks are unexpected and unpredictable. The techniques and explosive materials used can cause catastrophic damage. To limit this damage (to human life, buildings, vehicles, etc.) we need to use shielding to defend potential targets or employ strong blast-resistant materials in the design of such targets [1–4].

Under dynamic loads, materials show brittle behaviour. The ceramic bricks used for building construction are hazardous during fracture as the pieces fall, causing more damage where they land. The materials of old buildings are not replaceable, but additional retro-fitting can increase resistance [5–9]. In this way, while our cityscape does not change, the structural security of buildings can be increased. The retro-fitting of walls requires suitable selection of materials.

The construction materials currently in use are suitable for thermal insulation but do not provide

protection or reinforcement of masonry under excessive dynamic loads. Additionally, most of the applied insulation materials are flammable.

The most important part of composite design is the determination of loads and, therefore, the determination of stresses [10–14]. On the basis of the determined loads, we can select the matrix and reinforcing materials and we can analysis their adequacy. Currently, there is a large number of matrix and reinforcing materials to choose from. These materials can be used to build a composite that is suitable for the specified loads. Several design systems can be used to design composites, which have a wide materials database and simplify both material selection and design.

2. Composite test samples manufacturing process

During our design tasks, we used three different kinds of fibers (carbon fiber, glass fiber, aramid fiber). The mechanical properties of these woven materials depends on the weave type, meaning the structure of the fibers, the properties also depend on the fibers direction. The materials used are shown in **Figures 1–3**.

The covering layer of the composite was made by the resin matrix (Araldite LY 1564) lamination

Table 1. Mechanical properties of the epoxy resin impregnated composites [2]

	Glass fiber weave	Carbon fiber	Aramid fiber weave
Impact strength (kJ/m ²)	weave	Aramid fiber	76
Density (kg/m ³)	weave	1500	1400

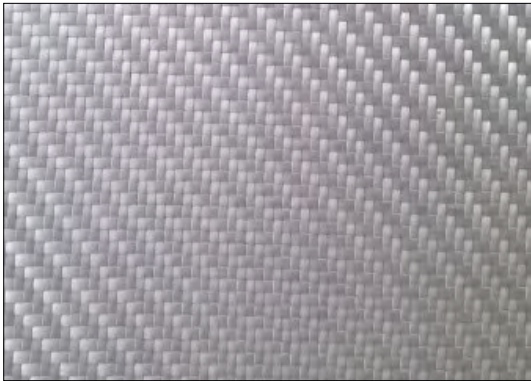


Figure 1. Glass fiber weave



Figure 2. Carbon fiber weave



Figure 3. Aramid fiber wave

process. **Table 1.** summarizes the mechanical properties of the materials used.

For the manufacturing of the composite lamination, single direction fiber structure materials were used. The test samples were made without a notch. The results of the Charpy impact tests are shown in **Table 1.** [2].

On the base of the literature data [2] we used 6 resin impregnated layers from the low strength aramid fiber and used 4 layers from the higher strength resin impregnated carbon and glass fiber to cover the samples.

The goal was to increase impact load resistance against impact loads of the traditional buildings walls by reinforced ceramic bricks. For the model tests we prepared an epoxy resin laminated fiber hybrid ceramic brick material, the layers are shown in **Figure 4.**

The mechanical properties of the used fiber reinforced materials as a function of the fiber direction, and layer numbers is shown in the **Table 2.**

The sandwich structured test sample was made with a vacuum infusion system. Cutting of the samples was performed after the solidification of the epoxy resin. On the basis of the samples anisotropy, the Charpy test impact load was positioned for the laminated surface (**Figure 5.**).

We simulated the dynamic load by Charpy impact test, the used test sample was without notch (**Figures 6–8.**).

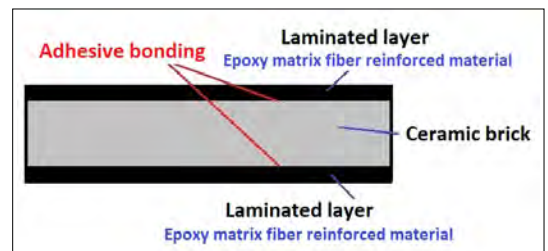


Figure 4. The sandwich panel layers

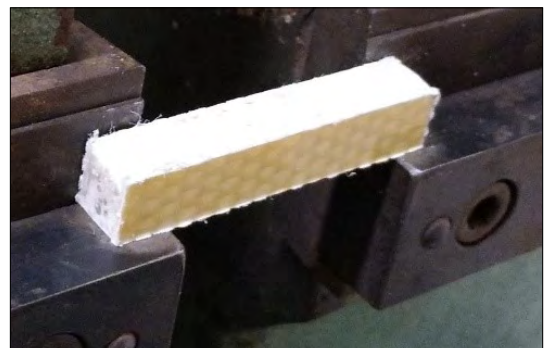


Figure 5. Test sample position during test

Table 2. The mechanical properties of the used composite materials mechanical properties

	Glass fiber	Carbon fiber	Aramid fiber
Weave (g/m ²)	390	480	220
Weaving type	2/2 Twill weave	2/2 Twill weave	1/1 Plain weave
Number of layers	4	4	6
Layer structure	(0 _{SZ}) ₄	(45 _{SZ}) ₄	(0 _{SZ}) ₆

**Figure 6.** Glass fiber weave and epoxy resin laminated test sample**Figure 7.** Carbon fiber weave and epoxy resin laminated test sample**Figure 8.** Aramid fiber weave and epoxy resin laminated test sample

3. Experiments

The test samples were tested by the Charpy impact instrument on the basis of MSZ EN ISO 179-1:2010 standard [4]. 1 kg load hammer and 10×10×55 mm size test samples were used for the first test.

The glass fiber weaved samples under 1 kg impact load showed high resistance, without breaking, the hammer rebounded, on the test sample surface, caused only small penetration (shown in **Figure 9**).

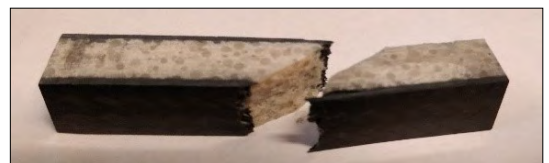
One side of the coating of the aramid fiber weave and epoxy resin laminated test sample flaked, and the ceramic brick split.

Carbon fiber weave and epoxy resin laminated test samples were broken (**Figure 10**), the composite is rigid.

In the case of the repeated test using a 30 kg load hammer, the result was unmeasurable. Even though visual assessment was possible.

Table 3. The results of the experiments

	Glass fiber weave	Carbon fiber weave	Aramid fiber weave
Impact energy (J)	7,3	5	6,9
Impact strength (kJ/m ²)	73	50	69

**Figure 9.** Glass fiber weave and epoxy resin laminated test sample after test, on the surface. Notice the impact formed notch**Figure 10.** Carbon fiber weave and epoxy resin laminated test sample after test

4. Conclusions

The glass and carbon fiber weave laminated test samples under a 30 kg impact load showed rigid behaviour, and they didn't shown toughness (Figure 12–13.). In the case of the aramid fiber weave and epoxy resin laminated test samples, the ceramic inner layer cracked but did not break, (Figure 14.).). One side of the composite the aramid layer became delaminated from the ceramic surface showing that the adhesive bonding was not enough strong.

The aramid fiber weave laminated test samples under 1 kg and 30 kg resisted the impact load without breaking. The glass fiber weave reinforced samples under 1 kg impact load, without modification but under 30 kg impact load, showed rigidity and breakage.

Our future aim is to test these test samples by impact load between 1 kg and 30 kg, to determine the load limit of the glass fiber weave reinforced samples.

It can be concluded that the aramid fiber weave lamination is suitable for dynamic load, but in the case of the sandwich structure used, the adhesive bonding was not strong enough between the aramid coating and the ceramic with the used epoxy resin.

Acknowledgement

The authors are grateful for the technical support during the test samples preparation to the associates of KANDSI Kft. (AKOBEZ)

References

- [1] Ashby M. F., Jones D. R. H.: *Engineering Materials 1. An Introduction to Properties, Applications and Design*. Third Edition, Elsevier Butterworth-Heinemann, Cambridge, UK P.K., 2005.
- [2] Szakali M., Szűcs E.: *The defence planning model formation and development / Védelmi tervezésmodellek kialakulása és fejlődése*. Hadmérnök, 12/1. (2017) 24–40. ISSN 1788-1919
- [3] Malick P. K.: *Fiber-reinforced composites*. Third edition. Taylor and Francis, Boca Raton, USA, 2008.
- [4] Ráthy I., Pinke P., Huszák Cs.: *PP mátrixú fröccsöntött kompozitok mechanikai vizsgálatai*. Acta Materialia Transylvanica, 1. (2018) 105–109. <https://doi.org/10.2478/amt-2018-0039>
- [5] Lange D.: *A review of blast loading and explosions in the context of multifunctional buildings*. Fire technology SP Technical Research Institut of Sweden 2013. ISSN 0284-5172
- [6] Gay E., Berthe L., Boustie M., Arrigoni M., Buzaud E.: *Effects of the shock duration on*

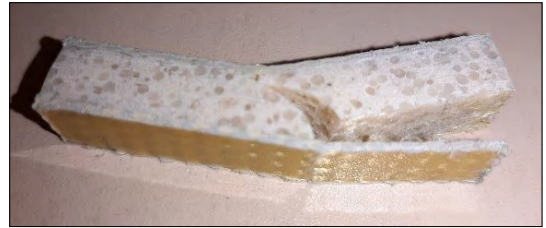


Figure 11. Aramid fiber weave and epoxy resin laminated test sample after test



Figure 12. Glass fiber weave and epoxy resin laminated test sample after test



Figure 13. Carbon fiber weave and epoxy resin laminated test sample after test



Figure 14. Aramid fiber weave and epoxy resin laminated test sample after test

- the response of CFRP composite laminates.* Journal of Physics D: Applied Physics, 2014
<https://doi.org/10.1088/0022-3727/47/45/455303>
- [7] Zvaková Z., Figuli L., Guttenová D.: *Analysis of blast load steel beam.* Juniorstav 2014, VUT Brno, ISBN 978-80-214-4851-3.
- [8] Figuli L., Jangl Š., Papán D.: *Modelling and Testing of Blast Effect On the Structures.* IOP Conference Series: Earth and Environmental Science, 44. (5), 052051
<https://doi.org/10.1088/1755-1315/44/5/052051>
- [9] Lu G., Yu T.: *Energy absorption of structures and materials.* Woodhead Publishing Limited, Cambridge, England 2000.
- [10] Qiao P., Yang M., Bobaru F.: *Impact Mechanics and High-Energy Absorbing Materials: Review.* Journal of Aerospace Engineering, 21/4. (2008) 235–248.
[https://doi.org/10.1061/\(ASCE\)0893-1321\(2008\)21:4\(235\)](https://doi.org/10.1061/(ASCE)0893-1321(2008)21:4(235))
- [11] Zhou H., Wang X., Ma G., Liu Z.: *On the effectiveness of blast mitigation with lightweight claddings.* Procedia Engineering, 210. (2017) 148–153.
<https://doi.org/10.1016/j.proeng.2017.11.060>
- [12] Figuli L., Štaffenová D.: *Practical Aspect of Methods Used for Blast Protection.* Key Engineering Materials, 755. (2017) 139–146.
<https://doi.org/10.4028/www.scientific.net/KEM.755.139>
- [13] Daruka N., Kugyela L.: *Ipari robbanóanyagok megjelenésének lehetőségei az improvizált robbanószerkezetek kialakításának tekintetében.* Robbantástechnika, 35. (2018) 155–174.
- [14] Galusca D. G., Galusca L., Tóth L.: *Analyses of Deformation of Fibre Reinforced Composites.* In: microCAD'98, M Section: International Computer Science Conference. Miskolci Egyetem, 1998.

Dynamic and High Temperature Quasi-static Examination of Tempered Glass

Borbála LEVELES,¹ Alexandra KEMÉNY,² Bálint KATONA³

University of Technology and Economics, Faculty of Mechanical Engineering, Department Materials Science and Engineering, Budapest, Hungary

¹ borbala.levelles@edu.bme.hu

² alexa@eik.bme.hu

³ katona@eik.bme.hu

Abstract

In everyday use glass materials cause a lot of damage or injuries when broken, as fracture mechanism and damage runoff cannot be predicted precisely. To gain knowledge on this issue, we studied the properties of tempered glass. The glass test samples were exposed to two types of destructive evaluations: normal and high temperature three-point bending and room temperature dynamic experiments with colliding small steel spheres. The evaluation showed that high temperature experiments are in correlation with sharp fracture edges, and dynamic impact creates shell featured circular crack propagation which prevents the spreading of the radial cracks, so the damage is concentrated to a small area.

Keywords: *tempered glass, quasi-static bending, fracture surface, dynamic.*

1. Introduction

Glasses are commonly used in the everyday life as building elements and objects. For safety reasons, it is worth examining the fracture mechanisms and the fracture surfaces of different glasses to reduce injury and the probability of accidents [1, 2]. In this research, the fracture properties of tempered glass were examined: which type of glass bears the highest mechanical loadings [3].

Glass as raw material has high compressive strength, however it is notably brittle, as no plastic deformation appears before breaking. This means that the fracture occurs without any detectable signal [4].

The solidification of amorphous, or non-crystalline materials are different from crystalline materials. While cooling, the glass becomes more and more viscous with decreasing temperature, but there is no definite temperature at which the liquid transforms to a solid [5–7].

When a non-crystalline material cools down from a high temperature, internal stress builds up inside the material, which is called thermal

stress. The cause of this behaviour is the difference in cooling rate and thermal contraction between the inner and outer regions. These stress values have the most influence on mechanical features. The glass tempering process implies deliberately generating internal stresses in the material. In soda-lime glasses residual stresses can be created by heating the glass up to 600°C, and then cooling down quickly to room temperature with an airstream. In this procedure the temperature of the surface cools more rapidly, and after dropping below the glass transition temperature it becomes rigid, while the interior remains warmer and cools down slower. In this case, the viscosity of the surface increases and is less susceptible to deformation, while the interior attempts to contract to a greater degree, so tension and compressive stress develops between the two surfaces (Figure 1.) [7].

Failure of tempered safety glass is the least dangerous, and despite the much greater force required to break, the material will fall apart into small but obtuse pieces, which can be held together in most cases by the middle foil between the

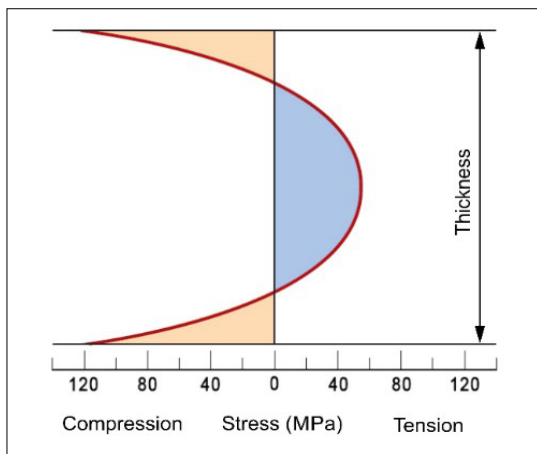


Figure 1. Residual stress-distribution in the cross-section of tempered glass on room temperature based on [7]

two layers [8]. This is significantly safer than untreated soda-lime glass, as the tempered glass can result much less physical injury [9, 10].

Quasi-static damage to brittle materials generally starts from a typically mirror-smooth small surface, and in the vicinity a veil surface is formed known as mist, followed by a hackle or needles spatially extending radially to the mirror-smooth surface [11–13].

There are typically two ways in which glass can be damaged by dynamic loads. Radial cracks may occur which, in the case of a cylindrical specimen, extend in the radial direction of the surface, splitting the surface into two or more parts [14]. These typically occur when any glass is damaged. Circular cracks, which usually stop radial cracks, result in a significantly smaller damage to the material. The latter is a characteristic failure mode of tempered glass [15, 16].

2. Materials and methods

The aim of this research was to estimate the damage and fracture processes caused by a certain mechanical load and heat by evaluating the fracture surface and breaking properties of the tempered glass.

For bending tests 5×15×100 mm bar shaped specimens were prepared from a soda-lime flat glass (Table 1.). The specimens were edge-polished, then tempered at 610°C for 2 hours and cooled in an airstream.

The glass samples were heated to three different temperatures (23°C, 300°C, 600°C) and a three-point bending test (3PB) was carried out with a

quasi-static load on an Instron 5965 Universal Material Testing Equipment at the loading rate of 1 mm/min.

Table 1. The composition of the glass material

	SiO ₂	Na ₂ O	CaO	MgO	Al ₂ O ₃
Quantity (%)	74	16	5	4	1

Beside the quasi-static examination, a dynamic load test was performed with a pneumatic shooter from 700 mm with a Ø6 mm steel ball at a velocity of 100 m/s.

These tests were performed on a windscreen made of 5 mm thick safety glass, laminated with a two-layer polyvinyl butyral (PVB) film. The overall dimensions of the windscreen are: 1000×1600 mm, supported by the two shorter edges. The untreated flat glass specimens were also 5 mm thick with a frame size of 200×200 mm, also supported on two edges.

After performing the experiments, the fractured surfaces were tested with an Olympus SZX16 stereomicroscope and a Zeiss EVO MA10 scanning electron microscope (SEM), in addition the dynamic penetration was recorded with a FASTCAM SA5 model 775K-C3 high-speed camera.

3. Results

The quasi-static measurements show, that tempered glass typically breaks without a precisely defined crack start point. The fractured samples at room temperature are not sharp, but the cracks spread in several directions (Figure 2.). Sharpness is defined as the planes of the line joining the vertex of the edge to the lower point of the adjacent two valleys <90°. It is important to notice, that the fracture appeared at 300°C testing temperature is starting from a small flat surface and spreading further in every direction (Figure 2. c, d). The specimen bent at 600°C no longer shows the characteristics like at lower temperatures and forms a sharp surface that is dangerous (Figure 2. e, f). The reason that the glasses were tempered at 610°C, which is very close to the temperature of 600°C, so the internal stresses during the elevated temperature measurement were reduced.

The three-point bending test results were processed to determine the flexural strength (1) and Young's modulus of the sample at different temperatures.

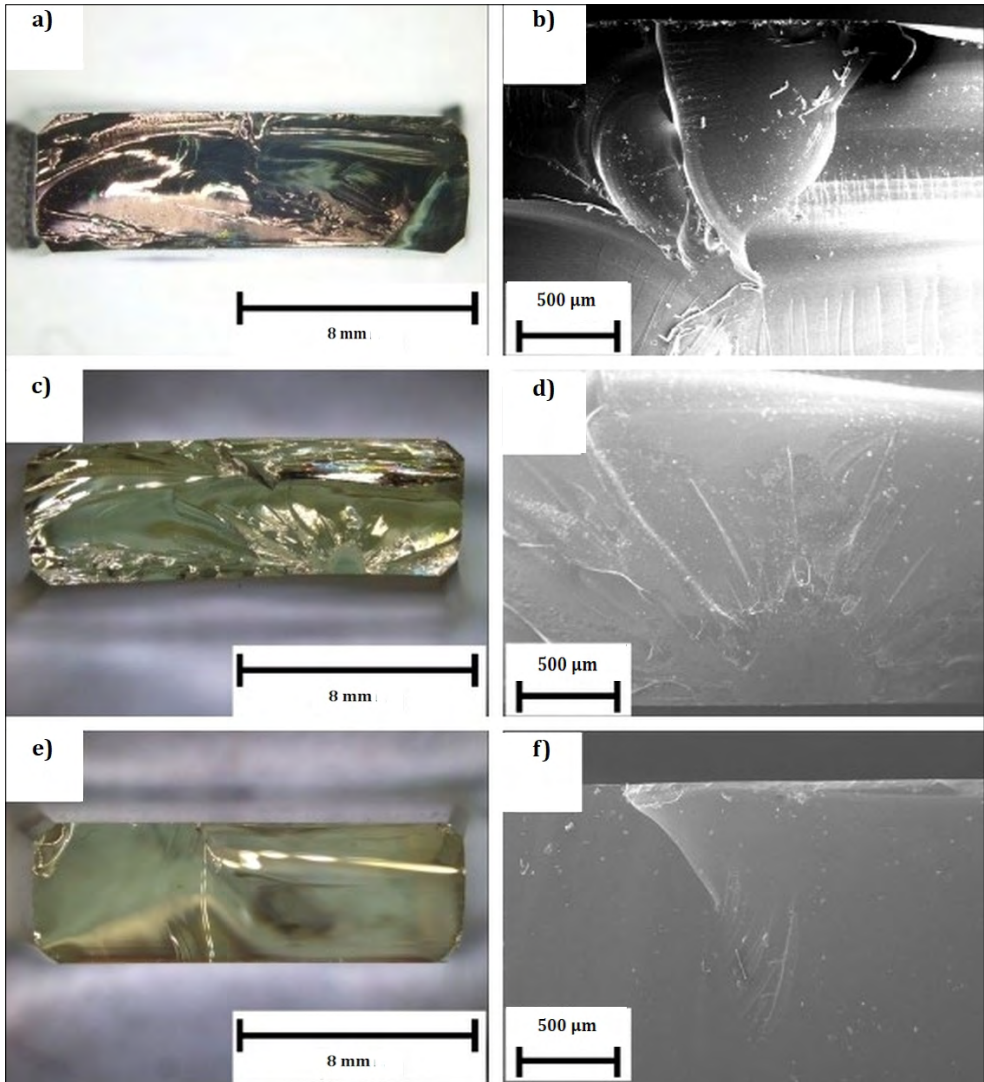


Figure 2. Stereomicroscopic (left) and SEM (right) images of the fractured surfaces formed by three-point bending (23 °C a, b; 300 °C c, d; 600 °C e, f)

$$R_{mh} = \frac{M}{K} = \frac{F_m L}{\frac{4}{ab^2}} = \frac{3F_m L}{2ab^2} \quad (1)$$

where:

- F_m – maximum force (N),
- L – support distance (mm),
- a – sample width (mm),
- b – sample length (mm).

Figure 3. shows their characteristics. It can be observed that both attributes decrease with increasing temperature. On this basis, it can be stated that the mechanical properties of the test

samples weaken, and their utility is limited in extreme conditions. This phenomenon can be explained by the fact that at 600°C it is already above the glass transition temperature of the test samples, namely its viscosity is significantly reduced.

During dynamic tests, the typical fracture pattern for safety glasses forms 0.100 ms after the impact occurs, and the cracks do not spread further (**Figure 4**). Fine glass powder appears at the point of collision, as the material is most damaged there. It can be observed that in the vicinity of the impact has circular, spiderweb like cracks which stops the further radial crack propagation, thus

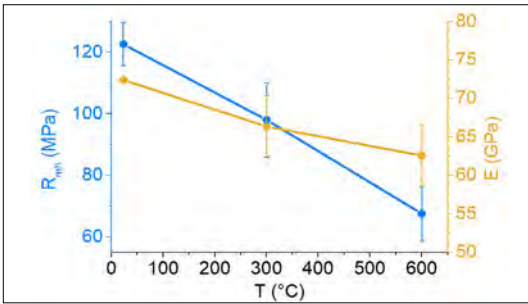


Figure 3. Temperature dependence of the bending strength and Young's modulus

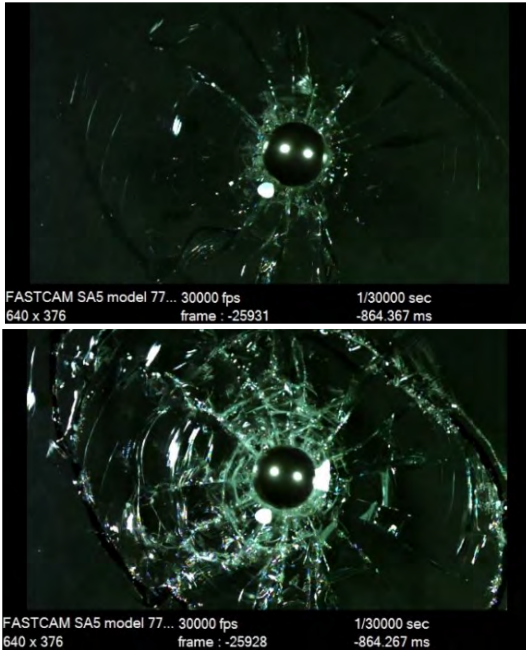


Figure 4. High speed camera recording of bullet impact at impression and 0.100 ms later

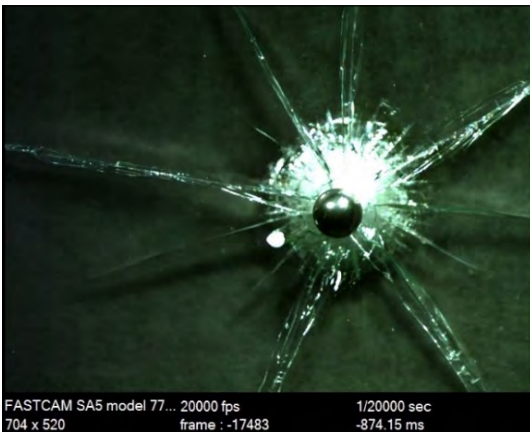


Figure 5. Soda-lime glass fracture due to dynamic load

the damage is limited to a small area. It is also important to note that only the outside of the wind-screen was examined, since the dynamic impact is not expected on the inside. During the tests, the inner glass layer was not damaged.

Dynamic examinations were also performed on non-tempered soda-lime glass samples as a reference (Figure 5.). It can be observed that more cracks radially spread and run toward the edge of the sample, when the glass plate is divided into different sized sharp parts.

4. Conclusions

At room temperature the tempered glasses broke into small pieces with smooth edges and branched cracks after the quasi-static bending. The formation of these edges, which are less dangerous and can result lighter damages, is related to the multiple cracks and small detachments due to the internal stresses. These cracks create a more complex but smoother surface due to the small folds. At 300°C, there is no significant difference between the fractures, however at 600°C, the fracture surface is less distributed, but the edges are sharp and therefore dangerous.

Dynamic tests have been used to observe the responses of tempered glass to high-speed point-to-point impact. Windscreens are also resistant to low-speed and high-speed impacts (such as rocks), whereby the fracture is concentrated to a small area. The energy absorbing capacity of the outer glass and the PVB layer is high, so the damage to the inner glass layer has not been reached during the examination.

In conclusion, tempered soda-lime glasses cannot be used safely at high temperatures, although its failure mechanisms at low temperatures are much safer than the breakage of untreated soda-lime glasses.

Acknowledgements

The publication reported herein has been supported by ETDB at BME.

References

- [1] Chen J. et al.: Experimental investigation on the radial and circular crack propagation of PVB laminated glass subject to dynamic out-of-plane loading. *Engineering Fracture Mechanics*, 112–113. (2013) 26–40. <https://doi.org/10.1016/j.engfrac-mech.2013.09.010>
- [2] Huang J. et al.: A study on correlation of pedestrian head injuries with physical parameters using in-depth traffic accident data and mathematical

- models. *Accident Analysis and Prevention*, 119. (2018) 91–103.
<https://doi.org/10.1016/j.oap.2018.07.012>
- [3] Xu J. et al.: Experimental study on mechanical behavior of PVB laminated glass under quasi-static and dynamic loadings. *Composites: Part B*, 42. (2011) 302–308.
<https://doi.org/10.1016/j.compositesb.2010.10.009>
- [4] Vogel W.: *Glass Chemistry*. Second Edition, Springer-Verlag Berlin, Heidelberg–Berlin, 1994.
- [5] Shackelford J. F., Doremus R. H.: *Ceramic and Glass Materials – Structure, Properties and Processing*. First Edition, Springer Science + Business Media LLC, New York, 2008.
<https://doi.org/10.1007/978-0-387-73362-3>
- [6] Callister W. D. Jr.: *Materials Science and Engineering – An Introduction*. Seventh Edition, John Wiley & Sons Inc, New York, 2007.
- [7] Kingery W. D., Bowen H. K., Uhlmann D. R.: *Introduction to Ceramics*. Second Edition, John Wiley & Sons, New York, 1976.
<https://doi.org/10.1149/1.2133296>
- [8] Nielsen J. H., Bjarrum M.: Deformations and strain energy in fragments of tempered glass: experimental and numerical investigation. *Glass Structures & Engineering*, 2. (2017) 133–146.
<https://doi.org/10.1007/s40940-017-0043-8>
- [9] Fennelly L. J.: *Effective Physical Security*. Fifth Edition, Butterworth-Heinemann, Oxford, 2017.
- [10] Yong Peng et al.: Investigation of the fracture behaviors of windshield laminated glass used in highspeed trains. *Composite Structures*, 207. (2019) 29–40.
<https://doi.org/10.1016/j.compstruct.2018.09.009>
- [11] Tandon R., Glass S. J.: Fracture initiation and fragmentation in chemically tempered glass. *Journal of the European Ceramic Society*, 35. (2015) 285–295.
<https://doi.org/10.1016/j.jeurceram-soc.2014.07.031>
- [12] Freiman, S. W., Wiederhorn, S. M., Mecholsky, J. J. Jr.: Environmentally enhanced fracture of glass: a historical perspective. *Journal of the American Ceramic Society*, 92/1. (2009) 1–112.
<https://doi.org/10.1111/j.1551-2916.2009.03097.x>
- [13] Bradt R. C.: The Fractography and Crack Patterns of Broken Glass. *Journal of Failure Analysis and Prevention*, 11. (2011) 79–96.
<https://doi.org/10.1007/s11668-011-9432-5>
- [14] ISO/TS 20746: Dentistry. Determination of the strength of dental amalgam by the Hertzian indentation strength (HIT) method, 2016.
- [15] Ahearn D. L. III et al.: Fracture patterns of impact resistant glass panel laminates with annealed and heat strengthened glass plates. *Ceramic Transactions Series*, 199. (2007) 383–396.
<https://doi.org/10.1002/9781118144152.ch31>
- [16] Knight C. G., Swain M. V., Chaudhri M. M.: Impact of small steel spheres on glass surfaces. *Journal of Materials Science*, 12. (1977) 1573–1586.
<https://doi.org/10.1007/BF00542808>

Role of the Features of Focused Laser Beam at Pulsed Laser Cutting

György MESZLÉNYI,¹ Enikő BITAY²

¹ Óbuda University, Budapest, Hungary, meszlenyi.gyorgy@kvk.uni-obuda.hu

² Sapientia Hungarian University of Transylvania, Faculty of Technical and Human Sciences Târgu Mureş, Department of Mechanical Engineering, Târgu Mureş, Romania, ebitay@ms.sapientia.ro

Abstract

In this article investigation of the roles of two important factors of focused laser beam, the focal spot diameter and the Rayleigh length as determining variables of the beam quality were made. The equations of these two factors are based on those most commonly used in the literature. The exchange between three different beam quality numbers were shown. It is proven on the basis of the scientific literature, that the beam quality degrades compared to the original data given by the factory of laser. The causes of the beam quality degradation are lens aberrations in the optical path of the given laser, and the shifting of the beam propagation ratio (M^2) to higher values. A new equation for estimation of the new, lowest value for M^2 factor is presented, based on the comparison of the laser cut material thickness to the depth of focus, which is two times the Rayleigh length.

Keywords: *laser cutting, laser beam, beam diameter, beam quality, beam propagation ratio (M^2), Rayleigh length.*

1. Introduction

In laser beam processing a special importance is given to the machining laser and within that to the cross section characteristics of the focused beam, the focal spot diameter, because the focused beam is that contactless tool which through energy transfer does the processing. Why is it important to know how large is the focal spot diameter? Because in laser cutting with a smaller focal spot diameter we get a smaller kerf, therefore there is less dross and a higher quality cutting requiring less post-production. Because of the narrower laser beam the heat affected zone is also smaller. The formulas for the focal point diameter are the same in much of the specialist literature, except that in order to reach a common format sometimes one has to double the radius to get the diameter and the data regarding the beam quality has to be calculated accordingly: by writing into the formula the M^2 beam quality factor which is the reciprocal of the K beam propagation factor (see no. 2.) [1], [2], [3], [4]:

$$d_{f0} = \frac{4\lambda f M^2}{\pi d_b} \quad (1)$$

Here λ is the wavelength of the laser, f is the focal distance of the lens that focuses the laser on the workpiece, M^2 is the beam quality factor which tells us which multiple of the ideal Gauss beam is the focal point diameter of the analysed beam, d_b is the diameter of the laser beam collimated close to the focusing lens. If we expand the laser beam collimated close to the focusing lens, the d_b beam diameter seen below will be multiplied with the beam expander factor, which is a number without measurement unit (B_e), it tells us how many times the beam diameter has increased compared to the unexpanded beam [1]:

$$d_{f0} = \frac{4\lambda f M^2}{\pi d_b B_e} \quad (2)$$

The Rayleigh length is a length, measured in the beam's own traveling direction, at which the surface of the laser spot doubles, its radius is multiplied by the square root of two, so the amount of

energy that goes to a unit of surface is half of that which is calculated in the focal point. Generally speaking a beam is considered to be focused within the double of the Rayleigh length, this is what we call depth of focus, so when we're cutting with laser, this is approximately the thickness of the material that the laser can cut. Its formula is very similar to that of the laser spot diameter, only here the focal distance of the focusing lens and the beam diameter before the lens are squared [1], [4]:

$$z_r = \pm \frac{4\lambda M^2 f^2}{\pi d_b^2 B_c^2} \tag{3}$$

The mentioned variables of the focused laser beam are represented in Figure 1. where the z coordinate is in the spreading direction of the laser beam, Θ the opening angle of the focused beam. Figure 1. was based on the unified characteristics of the figures in references [1] and [5] The following articles also discuss the beam quality: [6], [7], [8], [9].

2. Quantities of the beam quality

The beam quality appears in the definitions of the two most important characteristics of the beam cross section: the focal spot diameter and the Rayleigh length. It is important to know the different ways of defining the beam quality and also, how can we switch between them.

The beam parameter product (BPP) is an expression of the focusability of the laser beam which is given most often as the product of the beam waist radius within the resonator and the far field divergence angle, Θ_σ divided by four. Here Θ_σ : the opening angle of the asymptote cone that covers the expanding beam [10]:

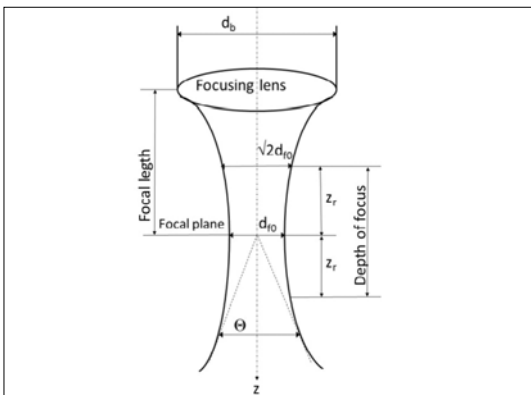


Figure 1. Representation of variables of the focused laser beam

$$BPP = \frac{d_{\sigma 0} \Theta_\sigma}{4} \tag{4}$$

Another definition is the beam quality factor, a measure that shows us how much the beam parameter product approaches the diffraction limit of an ideal Gauss-beam [10]:

$$M^2 = \frac{\pi d_{\sigma 0} \Theta_\sigma}{\lambda} \tag{5}$$

Yet another method is the K beam propagation factor which is the reciprocal of M^2 : [10].

$$K = \frac{1}{M^2} \tag{6}$$

For a non-ideal beam $M^2 > 1$, and $K < 1$. It follows from the above formulas that if one of the three variables that describe the beam quality is given, the others can be calculated, provided that we know the wavelength of the laser and we pay attention to the conversion of measurement units.

3. Effect of the possible changes in beam quality on the focal spot diameter and Rayleigh length

It should be clarified that the measuring of the beam quality is specified in standard ISO11146. For a correct measurement „the diameter of the laser beam $d(z)$ has to be measured on at least ten different spots in the vicinity of the focus, along the ray axis. Half of these spots must be within the Rayleigh length, the other half outside the double of the Rayleigh length” [11]. In order to measure the beam cross section in the type of impulse lasers discussed in this paper, simpler methods such as knife edge scanning or slit scanning cannot be used because the laser is not continuously on. Therefore we need a matrix sensor and because of the high sensitivity of the detector we also need several instances of beam attenuation in a way that does not influence the measurement results and does not distort the original beam that is to be measured [11].

The following is intended to present the effect which possible changes of beam quality can have on focal spot diameter and on Rayleigh length. This is a simplified model of the reality described above, which nevertheless can yield useful results. This approach can be analysed also because the modus structure of the analysed lasers is near TEM 00 which is close to the ideal Gauss-beam according to the support service. As such it is easier to analyse and approximate the possible

change of the focused beam cross section through these two variables. This analysis is also warranted by the fact that when we process something with a laser beam, we use the part of the beam that's close to the focal spot, so it is important to know where the focus is, what the size of the focal spot diameter is and that of the doubled Rayleigh length within which the laser can be used. Analysing the two variables described above has other advantages too. Based on these two variables the geometry of the focused laser beam can be described by equations: the beam diameter as a function of the z coordinate in the direction of the beam spreading, where z_0 is the z -coordinate of the focus plane [1]:

$$d_f(z) = d_{f0} \sqrt{1 + \left(\frac{z - z_0}{z_r}\right)^2} \quad (7)$$

Remembering the formulas for the focal spot diameter and the Rayleigh length, the question is: what gives the results in these formulas in each case? In both these formulas the same set of data appears (2 and 3). This analysis is linked to the cutting experiments described in our previous papers [12], [13], [14], [15], [16]:

- the wavelength: the changes in wavelength of the Nd:YAG laser used in our experiments are negligible.
- the focal distance of the focusing lens was constant: 50 mm.
- The diameter of the close collimated laser beam before the focusing lens is equal to the product of the unexpanded beam diameter d_b and the multiplier number of the beam expander (B_e): at a given beam expander state both are constant, the effect of the beam expander will be analysed later.
- The other parameters that appear in the formulas are constant.

Now let's analyse the cases of beam quality change that we found, these generally mean a degradation of the factory set beam quality, and as such an increase of the focal spot diameter and of the Rayleigh length:

There are five types of information that allow us to conclude that the beam quality is changing:

1. The LASAG KLS 246 FC's Nd:YAG laser developed for microprocessing is prone to thermal lensing: at a higher average power the middle of the crystal rod is warmer, it expands more than its outer surface, thus the two ends work as a lens with a curvature that changes as a

function of the average power. A similar effect has been described in one of the reference papers: [5]. According to the support service up to an average power of 5W it is $M^2 = 3$, at the maximum of 15W it is $M^2 = 5$, between those two values it changes in a linear fashion.

2. The zoom 8-step beam expander as an optical system consists of at least 3 lenses, because 2 lenses would be necessary for a Galilei-telescope type fixed beam expander. These systems too have image failure, let's take a look at the one that has the strongest effect: the spherical aberration. The essence of this is that the farther the analysed rings are from the optical axis in a radial direction, the closer the focus will get to the lens. The LASAG support service told us that at beam expander position nr. 1 we should remove the beam expander, since in this situation it only lets the collimated beam through, this is yet another proof of the fact that the beam expander causes a decrease in focusability.
3. According to Kaplan [1], with strong focusing and low F numbers the formulas for r_{f0} focus radius and z_r , are not true, corrective measures must be implemented (here: $F = f/d_b$):

$$r_{f0} = \frac{2\lambda F}{\pi K} + \frac{k_{sa} d_b}{2F^2} = \frac{2\lambda f}{\pi d_b K} + \frac{k_{sa} d_b^3}{2f^2} \quad (8)$$

The typical values for lenses with n refracting index and k_{sa} factors that correct lens aberrations, depending on the lens material, are the following:

ZnSe	$n = 2.40, k_{sa} = 0.0312$
GaAs	$n = 3.27, k_{sa} = 0.0139$

One thing surely follows from this equation: the value of r_{f0} , and with it that of d_{f0} and z_r , will increase, therefore the focusability of the lens will be worse. Here the K beam expanding factor and the correction appear separately, we would include these in the value of the M^2 factor because that seems to be more logical even if the author treats them separately. In the paper quoted in nr. 4 this correction is part of the M^2 factor. There are two reasons why we cannot count these two factors: the first one is that the author doesn't tell us where the limit of strong focusing is, obviously it means a large beam diameter before the lens and a lens with a small focal distance, we suspect that the maximal beam expander position and the 50 mm focusing lens is part of it. The second one is that we cannot identify the material of the lens,

therefore we don't know which corrective factor to use.

4. In Harp's paper [4]: „A Practical method for determining the beam profile near the focal spot” which was published in a prestigious Springer magazine the author analysed the beam quality of the IPG Photonics made 300 W, CW, Ytterbium fiber laser by creating welding seams on the material inclined in front of the focused laser beam. The initial beam quality factor was $M^2 = 1.04$. The laser beam exited from a 9 μm diameter fibre, after collimation its diameter was of 4.5 mm. They used a fivefold beam expander to get a smaller focal spot, following that they tried three different focusing lenses, with a focal distance of 150 mm, 100 mm, and 60 mm. The M^2 value given by the factory was first corrected because of an unnamed optical failure in the lenses: here too the author divides with the square of the lens' focal distance in the correction, the „a” factor is given by the welding experiment:

$$M^2 = M_0^2 + \frac{a}{f^2} \tag{9}$$

According to the diagram that sums up the results in the paper for a 60 mm focus lens, using the above correction the initial 1.05 value of M^2 increases to 2.5, if one includes the spherical aberration, the value will be approximately 6.

5. In Zimmermann' paper [3] an IPG YLR-200-SM single modus fibre laser is analysed, the author gives the unfocused beam diameter for the collimated beam, the theoretical focal spot diameter calculated from this, the Rayleigh length and the power density. But in reality the optical failures of the lens, most importantly the spherical aberration will increase the theoretically achievable focal spot size. The focal spot diameter increases in proportion to the cubic diameter of the beam before the focusing lens. The variables of the focused beam were measured with the knife edge scanning method defined in standards ISO 11145 and 11146. During the experiments they analysed the focus shift which occurred in the direction of the spreading and which depended on the laser power; its value was around 110 μm, exceeding the 89 μm Rayleigh length. This focus shift was caused by the warming up of the laser guiding optical elements and their sockets. Data for calculations: wavelength: 1070 nm, $M^2 < 1.1$; focal distance of the focusing lens: 50 mm, initial beam diameter: 6.5 mm [4]. An interesting aspect of the experi-

ment is that they used the beam expander first as an expander and thus the measured focal spot diameter was larger than the theoretical value (Table 1. row 3.), next they decreased the beam to half and so they got a focal spot diameter that was smaller than the theoretical value (Table 1. row 1.). The advantage of decreasing is that the Rayleigh length increased so a thicker material could be processed.

The degradation of the beam quality can be caused by the staining of the protective glass that's in front of the focusing lens that may be caused by the small droplets of material splashing from the workpiece, if we notice that, the protective glass must be changed.

Table 1. Comparison between the calculated theoretical values according to the paper and the measured results [3]

Beam diameter (mm)	3.25	6.5	13
Theoretical focused diameter (μm)	23	12	6
Theoretical Rayleigh-length (μm)	355	89	22
Measured focused diameter (μm)	20	14	9.4

4. Estimating the degradation of the M^2 factor in five previous experiments

Here we give a new method which allows for a lower approximation to the degradation of the M^2 factor based on the comparison between the processed material thickness and the Rayleigh length. During the five experiments we used a LASAG KLS 246 FC laser. According to the support service for this laser $M^2 (P_{average} = < 5W) = 3$ and $M^2 (P_{average} = 15W) = 5$ and between these two values it is linear. From this we can state the equation of the straight $y = 0,2x + 2$ if $5 < x < 15$, where y is the M^2 factor and x the $P_{average}$. In the table presenting the characteristics of the first three experimental processing (Table 2.) the M^2 factor can be calculated which gives values between 3.7 and 4.2. Thus the size of the focus spot and a first approximation of the Rayleigh length can be calculated. The double of the Rayleigh length was much less than the thickness of the cut material therefore we had to readjust the M^2 factor.

From the equation that gives Rayleigh length = half of the material thickness (v_a) rearranging (3) formula and stating a new equation (10) we calculated the estimated value of the new M^2 which turned to be around 7.

$$\frac{v_a}{2} \pi d_b^2 B_c^2 = M_{aj}^2 \tag{10}$$

Table 2. Values of M^2 factor and d_{f0} and z_r , both theoretical and readjusted based on the material thickness of the cut tube

	First experiment [8]	Second experiment [9]	Third experiment [10]
Material thickness (mm)	0.117	0.12	0.12
Operation	cutting	cutting	cutting
Average power	8...11.2 W	10-12 W	8.7 W
Medium average power	9.6 W	11 W	8.7 W
M^2 on medium average power based on data from the support service	3.9	4.2	3.7
d_{f0} (μm)	13.3	14.2	12.7
$\pm z_r$ (μm)	± 33.2	± 35.6	± 31.7
The z_{rnew} necessary because of the thickness of the cut wall (μm)	± 58.5	± 60	± 60
The new M^2 factor calculated from this	6.9	7.1	7.1
The new focal spot diameter calculated from this (μm)	23.4	24	24

Based on the new M^2 factor the focal spot diameter was recalculated which was around 20 micrometers, the interesting part of that is the fact that with a beam expander in the 8th position, that was the approximate size of the kerf (Table 2.). The results are represented in Figure 2.: both the focal spot diameter and the Rayleigh length increased.

Applying this line of thought to the sheet cutting experiment done with a 0.4 mm, beam expander in the 4th position, the value of the M^2 factor calculated from the equation based on the data given by the support service turned out to be between 3.8–4.8. The double of the Rayleigh length calculated from this data was still less than the material thickness. If we made the Rayleigh length equal to half of the material thickness, M^2 turned out to be 5.9 which is 1 less than what we get with the beam expander in the 8th position. (Table 3.). This result matches those of the previously presented analysis, obviously if the diameter of the beam that passes through the lens system decreases, if we apply a beam expander multiplier in the 4th instead of the 8th position, the spherical error decreases and thus the beam quality improves.

Table 3. Values of M^2 factor and d_{f0} and z_r , both theoretical and readjusted based on the material thickness of the cut tube

	Fourth experiment [11]	Fifth experiment [12]
Material thickness (mm)	0.4	0.4
Material geometry	sheet	sheet
Material quality	AISI 304L	AISI 304L
Operation	cutting	cutting
$P_{average}$	12.5....16.	9.2
Beam expander multiplier	4	4
Medium average power	14.25 W	9.2 W
M^2 on medium average power based on data from the support service	4.85	3.84
d_{f0} (μm)	32.87	26.02
$\pm z_r$ (μm)	± 164.3	± 130.12
The z_{rrij} necessary because of the thickness of the cut wall (μm)	± 200	± 200
The new M^2 factor calculated from this	5.9	5.9
The new focal spot diameter calculated from this (μm)	40	40

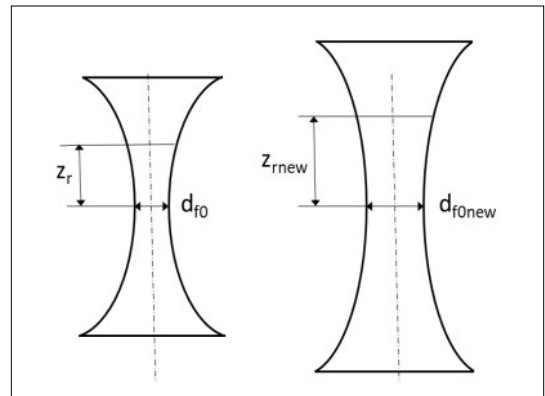


Figure 2. A representation of the theoretical values of the focal spot diameter and the Rayleigh distance, along with those calculated on the basis of the estimated M^2 factor

5. Conclusions

In this paper we analysed the effect of changes in the two important variables of a focused laser beam: the focal spot diameter and the Rayleigh length as variables that appear in the most wide-

spread formulas in the reference bibliography. We present the way these variables that express beam quality and are present in both formulas can be converted into each other and based on reference bibliography we prove that in comparison with the factory given values of these lasers the beam quality will be degraded due to the flaws in the lenses that are in the optical path of the laser beam, thus the value of the M^2 factor will increase. To estimate the lower limit of this increased M^2 variable we presented a new correlation which is based upon a coordination between the thickness of the cut material and the double of the Rayleigh length as the depth of focus.

References

- [1] Kaplan A. F. H.: *Theoretical Analysis of Laser Beam Cutting*. Shaker Verlag, Aachen, 2002. 12–14. ISBN 3-8322-0803-8
- [2] Paripás B., Szabó Sz., Kocsisné Baán M., Tolvaj B., Bencs P.: *Lézeresmérési és megmunkálási eljárások a gépészetben*. Nemzeti Tankönyvkiadó, 2009. 66–67.
- [3] Zimmermann M., Mys I., Schmidt M.: *Micro cutting of thin sheets with single mode fiber lasers*. Laser assisted net shape engineering 5. Proceedings of the LANE, 2007. 220–224.
- [4] Harp W. R., Paleocrassas A. G., Tu J. F.: *A Practical method for determining the beam profile near the focal spot*. The International Journal of Advanced Manufacturing Technology, 37. (2008) 1113–1119. <https://doi.org/10.1007/s00170-007-1067-z>
- [5] Wirth P.: *Introduction to Industrial Laser Materials Processing*. Hamburg, Germany, Rofin-Sinar Laser, 2000. 14–59.
- [6] Hemmerich M., Thiel C., Lupp F., Hanebuth H., Weber R., Graf T.: *Reduction of Focal Shift Effects in Industrial Laser Beam Welding by Means of Innovative Protection Glass Concept*. 8th International Conference on Photonic Technologies LANE 2014. Physics Procedia, 56. (2014) 681–688. <https://doi.org/10.1016/j.phpro.2014.08.161>
- [7] Rodrigues C., Vanhove H., Duflou J. R.: *Direct diode lasers for industrial laser cutting: a performance comparison with conventional fiber and CO₂ technologies*. 8th International Conference on Photonic Technologies LANE 2014. Physics Procedia 56. (2014) 901–908. <https://doi.org/10.1016/j.phpro.2014.08.109>
- [8] Thombansen U., Hermanns T., Stoyanov S.: *Setup and Maintenance of Manufacturing Quality in CO₂ Laser Cutting*. 2nd International Conference on Ramp-Up Management 2014 (ICRM). Procedia CIRP, 20. (2014) 98–102. <https://doi.org/10.1016/j.procir.2014.05.037>
- [9] Hashemi S. S., Sabouri S. G., Khorsandi A.: *In situ measurement of laser beam quality*. Applied Physics B, (2017) 123–233. <https://doi.org/10.1007/s00340-017-6811-y>
- [10] MSZ EN ISO 1145 Optika és fotonika. Lézerek és lézerberendezések. Szakszótár és jelképek (ISO 1145:2018)
- [11] Buza G.: *Lézersugaras technológiák I*. Edutus Főiskola, 2012. 24–29.
- [12] Meszlényi Gy., Dobránszky J., Puskás Zs.: *Laser cutting of high precision tubes*. Material Science Forum, 589. (2008) 427–431. <https://doi.org/10.4028/www.scientific.net/MSF.589.427>
- [13] Meszlényi Gy., Bella Sz., Nagy P., Dobránszky J.: *Laser beam cutting and welding of coronary stents*. BID-ISIM Welding and material testing, (2008) 14–11.
- [14] Meszlényi Gy., Izápy V.: *Optimization method of laser cutting parameters for high precision stainless steel tubes*. In: Proceedings of the SIP 2008, 26th International Conference Science in Practice Osijek, Horvátország, 2008. 95–97.
- [15] Meszlényi Gy., Dobránszky J., Dévényi L.: *Laser cutting of stainless steel thin sheets with pulsed Nd:YAG laser*. 6. In: Országos Gépészeti Konferencia, Gépészet 2008, Budapest. Magyarország, Budapesti Műszaki és Gazdaságtudományi Egyetem, 2008. 1–5.
- [16] Meszlényi Gy., Dobránszky J., Puskás Zs.: *Role of the laser focus position in the laser beam cutting of thin stainless steel sheets*. Material Science Forum, 659. (2010) 209–214.

Application of Additive Manufacturing for the Repair of Forging Dies

Sándor UZONYI

Flexman Robotics Ltd., Budapest, Hungary, us@flexmanrobotics.hu

Abstract

In this paper the investigated conditions and possibilities of repairing forging dies with high precision robotic MAG welding are presented. Different welding wire electrodes were examined and compared by their processability. Productivity, process stability, slag and fume formation were in the focus of investigation. Metallographic tests were carried out to validate the compliance of welded layers. Based on the performance of the wire electrodes, recommendations have been elaborated for the procedure specification and also for further investigation. Some robot cell layouts have been designed adapting to the special working environment and requirements of the welding procedure.

Keywords: : *additive manufacturing, wire arc additive manufacturing, robotic welding, hardfacing.*

1. Introduction

1.1. Purpose

Flexman Robotics Ltd's customers have been interested in robotising the repair welding of hot work tool steels in order to increase the accuracy of the welding material application, thus reducing welding and machining time and related costs. The goal of the research was to find suitable welding material and develop a related welding technology and robot system. For this purpose, experiments were carried out to evaluate the weldability of the tool steel to be repaired, while measuring the factors that mainly influence the usability of the examined welding materials and the reliability of the technology. Then, the hard layers were subjected to metallographic examination to validate the technology used.

1.2. Main characteristics of overlay welding

Overlay welding is a widely used technique for maintenance and repair tasks, as well as for the manufacture of products whose surface properties must be substantially different from those of the cross-section, this process is known as hardfacing. When overlay welding is used, typically the entire surface is welded in one or more layers, or when material deficiencies are replaced,

the surrounding area is partially or completely removed, and a much larger portion than the original discontinuity is being welded. In order to increase accuracy, a company carrying out hardfacing or overlay welding has a strong economic interest. Welding materials for hardfacing are very expensive, and the welded excess material must be subsequently removed by machining, which is also very costly since these materials are generally difficult to turn [1].

Precision is a connecting factor between conventional overlay welding and additive manufacturing, which usability we have previously analysed in detail [2]. Significant advances have been made in the field of wire and arc additive manufacturing (WAAM) in recent years. Practical applications are gaining ground and the number of high-precision tool repair companies is increasing [3–5].

1.3. Weldability examinations

The professional repair of tools exposed to wear and attrition can bring significant benefits, as beyond the original quality, careful selection of welding materials and technology can extend the life of the original. A tool can be repaired multiple times, so well-designed repair-overlay welding technology is very cost-effective [6].

Tool steels can be divided into two major groups in terms of welding: high-alloy and medium-alloy and non-alloy tool steels. Most of them remain soft, austenitic for a long period of time after cooling from the quenching temperature to the pre-heat temperature for about 30 minutes. Staying in this temperature range can work for several hours without the risk of cracking. This is a commonly used and highly reliable method for welding high or low alloy tool steels, however, such a high degree of preheating is not always permissible [1]. The examined tool steel is designated according to EN ISO 4957 as 55NiCrMoV7 (short code: 1.2714), a forging tool made of tool steel cannot be preheated to this high temperature range. A number of methods have been developed to determine preheating and the associated specific heat input, but due to the high carbon equivalents they may not be used, or only with special considerations. Several of these are hereby examined, however, only two will be presented: the Kasuya–Yurioka and the Béres methods.

1.3.1. The Kasuya–Yurioka-method

This method is one of the possible approximations for the calculation of the cooling time of high carbon steels to 50 % martensite. This method was refined by T. Kasuya and N. Yurioka [7] using the CEH carbon equivalent of Harden :

$$T_{50} = (T_m \cdot T_b)^{0.5} = \exp(5,3CE_H + 3,1CE_{III} - 2,03)$$

$$CE_H = C + \frac{Si}{24} + \frac{Mn}{6} + \frac{Cu}{15} + \frac{Ni}{12} + \frac{Cr}{8} + \frac{Mo}{4} + \Delta H$$

$$CE_{III} = C + \frac{Mn}{3,6} + \frac{Cu}{20} + \frac{Ni}{9} + \frac{Cr}{5} + \frac{Mo}{4}$$

$$T_m = \exp(10,6CE_H - 4,8)$$

$$T_b = \exp(6,2CE_{III} - 0,74)$$

where

- T_{50} - the cooling time needed for 50 % martensite,
- T_m - the cooling time needed for 100 % martensite,
- T_b - the cooling time needed for 0 % martensite,
- CE_H - carbon equivalent of Harden,
- CE_{III} - carbon equivalent of Yurioka, which is used to estimate the strength of the weld metal.

It is important to note that this is for approximation purposes only, since CE_H can be interpreted up to 0.3% carbon content, above this limit the relationship between carbon equivalent and carbon content is no longer linear. Using this re-

lationship, the critical cooling time for material 1.2741 results in 4 to 226 minutes, depending on the composition [7]. This large interval illustrates the relative accuracy of the calculation. Other widely used approximations, where the carbon equivalent of 1.2741 was outside the interpretation range, lead to similar results [8, 9].

1.3.2. The Béres method for high alloy steels

The best way to do this is to start from the CCT diagram of the material and weld it with so-called bainite preheating. In this case, the preheating temperature is the peak point of the bainite conversion curve and the preheating should be done slowly.

Based on this (Figure 1.) the decision was made to set the preheating temperature at 400–450 °C and the specimens were cooled down inside the oven [10].

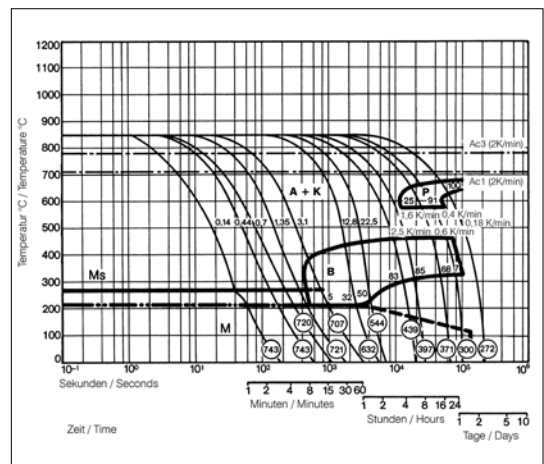


Figure 1. Relevant part of the CCT diagram for tool steel 1.2741 (vertical axis: temperature (°C), horizontal axis: time (s) [10]

1.4. The welding materials used

Four type of welding materials were used for the experiments, which differed significantly in their composition and processing properties. All wires were flux-cored and had a larger diameter than usual in robotic welding, since the typical wire diameter for robotic welding is 1.0 mm, the main properties of the used wired are listed in Table 1.

The development of the welding technology also required the inspection and revision of the technology window provided by the manufacturers.

Table 1. Summary of welding materials

Wire	Base	Alloying elements	Diameter
H1	Fe	Cr-Mo-C	1.2 mm
H2	Fe	Mo-Cr-C	1.2 mm
H3	Fe	Nb-Cr-C	1.6 mm
H4	Ni	Cr-Mo-W	1.6 mm

2. Welding experiments

To test the wires, 6 mm thick overlay welding was performed on a 100×100×250 mm specimen, twice for each. For the welding process a Yamaha EA1400 robot and an M21 type gas mixture were applied. Two samples of each were prepared. Meanwhile the processability was examined and later samples from these specimens for metallographic examination were machined..

2.1. Evaluation of processability

When evaluating processability, there are several aspects that are difficult to quantify. The features considered as important were evaluated using a scoring method established by me and summarized in tabular form. During the scoring process, the properties of the welding materials from one to four, with 1 being the worst and 4 being the best were rated. The properties and their evaluation criteria are as follows, the evaluation and comparison is summarized in **Table 2.**:

- Stability of the arc (I.): is it possible to find settings in the current-voltage technology-window specified by the manufacturer that provides a stable, well-focused and controllable arc?
- Spattering (II.): the rate of spattering with the most stable curve and the size of the droplets flying away. Fewer and smaller spattering is more beneficial.
- Shape of the bead (III.): the contact angle of the reinforcement of the weld, is there a risk of discontinuity during the welding of the next row, how smooth or wavy the surface will be after welding? Welds with wide and small contact angles are desirable.
- Productivity (IV.): time spent welding the specimen. The most productive procedure will be more favourable.
- Slag (V.): amount of slag formed after welding and its adhesion to the surface. Slim, easy to remove and meltable slag is more favourable.
- Fume (VI.): the wire that can be welded with less fume and soot formation is more favourable.

Table 2. Comparison of the used wires

Wire	I.	II.	III.	IV.	V.	VI.	Σ
H1	2	3	2	2	3	3	15
H2	1	2	3	3	4	3	15
H3	4	4	4	4	1	1	18
H4	4	3	4	3	4	2	20

2.2. Verification of the adequacy of the technology

The specimens were first subjected to a visual testing (VT), and after cooling, if possible, a regular penetration test (PT) was carried out. The specimens that did not pass these tests were no longer subjected to the micro-, macro-structure and hardness tests (HV). The results are summarized in **Table 3.**

Table 3. Summary of the evaluation of the welded specimens; OK = acceptable, NO = not acceptable, – = not tested (the samples marks are the same as the wire used for its manufacturing process)

Sample	VT	PT	Mikro	Makro	HV	Σ
H1	OK	OK	OK	OK	OK	OK
H2	NO	OK	–	–	–	NO
H3	–	–	OK	NO	OK	OK
H4	NO	NO	–	–	–	NO

In the case of H2 welding material, significant current fluctuations occurred during welding, which resulted in large fusion defects. The welds that were not affected by these phenomena haven't cracked.

In the case of welding material H4, the wire that worked properly during the setup produced a significant porosity of the weld metal. In the case of welding material H3, the slag layer was so thick and adherent that it was not possible to remove it, and large slag inclusions remained between the layers. In the H1 sample evenly distributed micro-slag inclusions can be observed on the cross-sections; however they do not significantly affect the functioning of the tool, their size and extent are acceptable.

3. Designing the robot cell

The following aspects had to be considered when designing possible robot cell variants:

- Reach: The robot must reach the work piece so that no singular arm position is formed during welding.

- Access: defined jointly by the robot and the welding torch. The internal wiring design is advantageous.
 - Heat load: a key issue due to the high preheating temperature. A design that is more heat resistant or has a lower heat load is preferred.
- Each robot cell was designed so that all of them have two workstations. This allows the preparation of the pieces to be welded at the same cell.

3.1. Extended reach robot

A large part of the robotic arm is located away from the welding area, so the radiant heat of the work piece is less stressful and the robot can also reach large tools. The disadvantage of this design is that the robot arm, for a general welding robot, is less universal, so if an existing task is eliminated, it will be harder to find a new one for this exact design. An external wired welding torch does not provide as good access as it can be with mounted on integrated wired robots (Figure 2).

3.2. Robot with floor mounted track

The YR MH2010 has an extended work area, and is an internally wired welding robot, suitable for any welding task (Figure 3). With the TSL 1000 floor mounted track, the robot's working space can be greatly increased, and the reach is improved not only in quantity but also in quality by making it easier to avoid singular arm positions.

3.3. Gantry robot

The biggest advantage of the Gantry robotic arm, which is mounted on a two-axis, upper travel track, is that its working area is very large, which means that it reaches every point of a large forging tool with a constant confidence (Figure 4.).

4. Summary

The optimal welding material can only be selected through field abrasion tests. The H1 welding material can be released without restrictions for these advanced tests. Despite the excellent workability of the H3 welding material, it is unlikely to work if slag inclusions cannot be satisfactorily eliminated in further experiments. Feed problems with H2 wire can be eliminated with a knurled roller and higher clamping force, further investigations are recommended. It could be also useful also repeating the tests with a new dose of H4 wire.

The design of the robot cell must be determined jointly with the customer, as operational conditions and financial capabilities may override

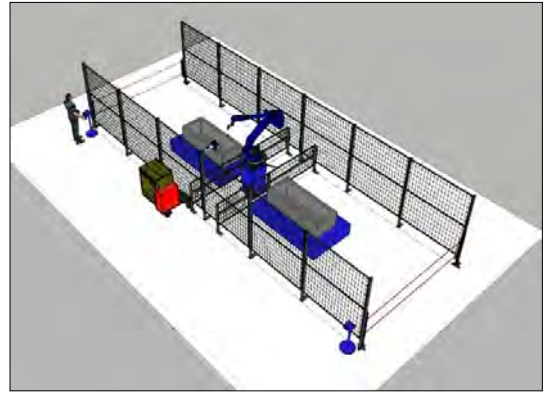


Figure 2. Robot cell with extended reach robot

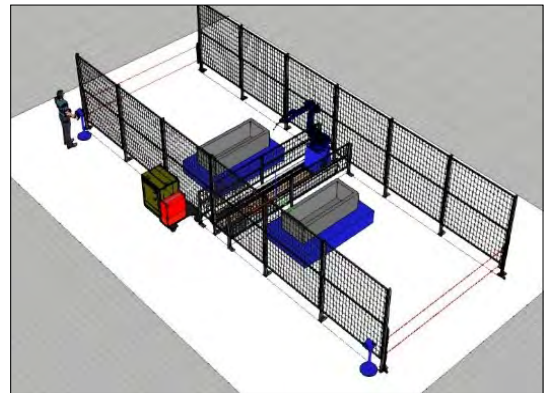


Figure 3. Robot cell with floor mounted track

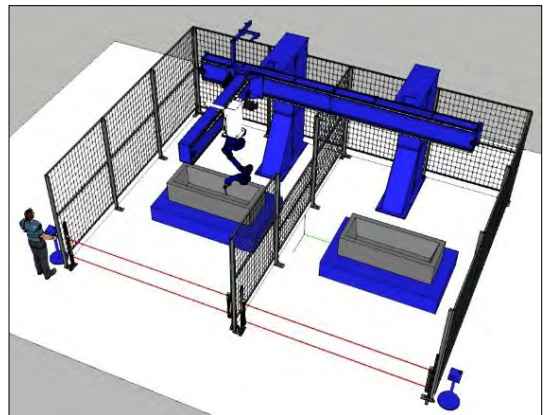
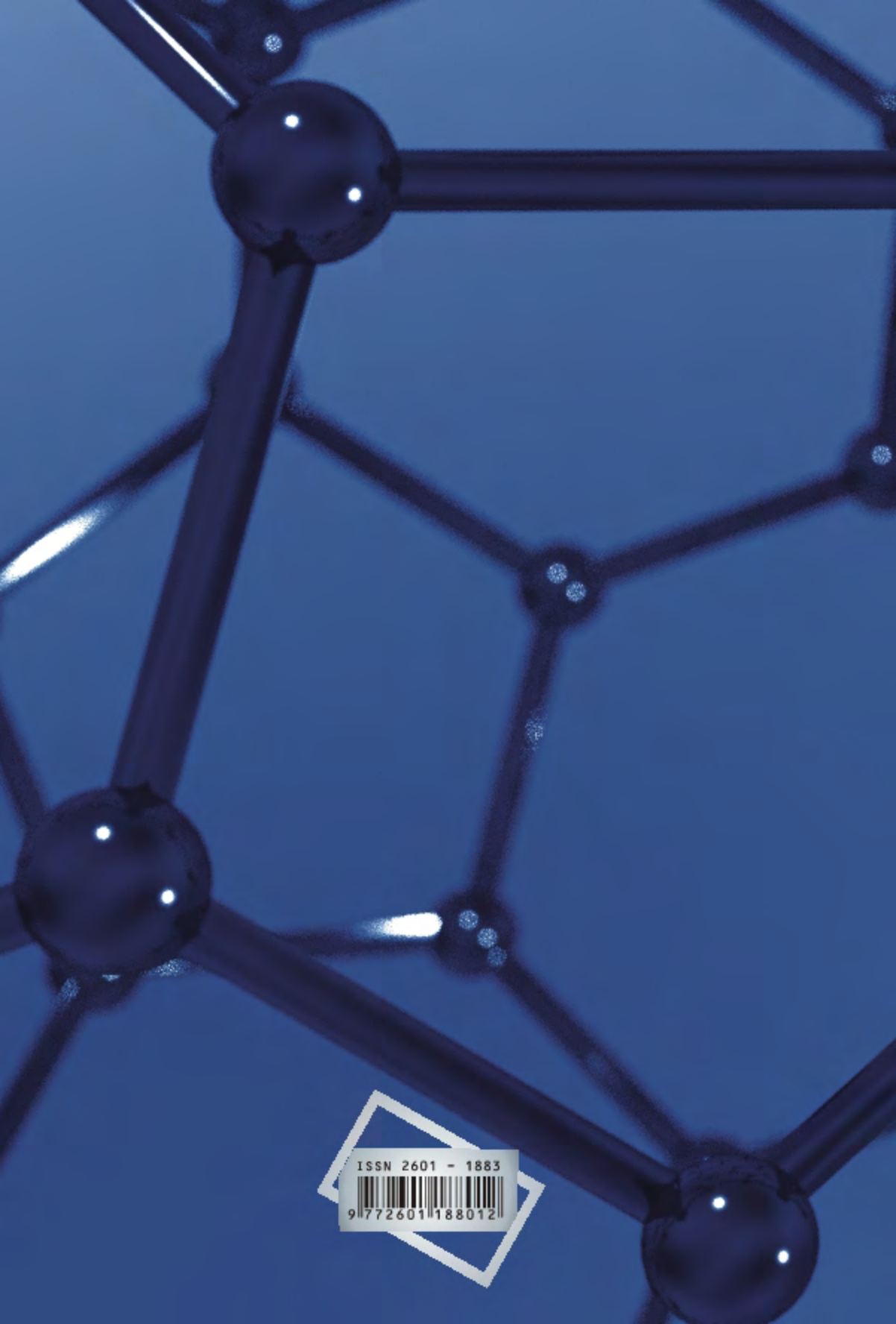


Figure 4. Robot cell with a two-axis upper travel track

other considerations. From the point of view of robot programming and access, the upper travel track cell with a Gantry robot is the best design, but also the heat load of the robot is the highest in this case; it is therefore necessary to consider what additional protection the equipment can withstand.

References

- [1] Béres L.: *Javító- és felrakóhegesztések*. In: Hegesztési zsebkönyv. (Szerk.: Gáti J.). Cokom Mérnökiroda Kft., Miskolc, 2003. 539–557.
- [2] Uzonyi S., Asztalos L., Farkas A., Dobránszky J.: *Additív hegesztéses gyártás jelene és jövője*. Hegesztéstechnika, 28. (2017) 89–92.
- [3] Ding D. et al.: *Wire-feed additive manufacturing of metal components: technologies, developments and future interests*. The International Journal of Advanced Manufacturing Technology, 81/1–4. (2015) 465–481.
<https://doi.org/10.1007/s00170-015-7077-3>
- [4] Wang F. et al.: *Microstructure and Mechanical Properties of Wire and Arc Additive Manufactured Ti-6Al-4V*. Metallurgical and Materials Transactions A, 44/2. (2013) 968–977.
<https://doi.org/10.1007/s11661-012-1444-6>
- [5] Ding D. et al.: *A multi-bead overlapping model for robotic wire and arc additive manufacturing (WAAM)*. Robotics and Computer-Integrated Manufacturing, 31. (2015) 101–110.
<https://doi.org/10.1016/j.rcim.2014.08.008>
- [6] Ali Y. et al.: *Wire arc additive manufacturing of hot work tool steel with CMT process*. Journal of Materials Processing Technology, 269. (2019) 109–116.
<https://doi.org/10.1016/j.jmatprotec.2019.01.034>
- [7] Kasuya T., Yurioka N.: *Determination of Necessary Preheat Temperature to Avoid Cold Cracking under Varying Ambient Temperature*. ISIJ International, 35/10. (1995) 1183–1189.
<https://doi.org/10.2355/isijinternational.35.1183>
- [8] Bauer F., Béres L., Buray Z., Szita L.: *A legfeljebb közepesen ötvözött edzhető acélok*. In: A hegesztés anyagismerete és a hegesztéstechnológia alapjai. Budapesti Műszaki Egyetem Mérnöki Továbbképző Intézet, Budapest, 1995. 54–64.
- [9] Béres L.: *Determination of an optimized Interpass Temperature for the Welding of Martensitic Stainless Steels*. The International Journal for the Joining of Materials, 9/1. (1997) 16–19.
- [10] Bauer F., Béres L., Buray Z., Szita L.: *Erősen ötvözött edzhető acélok előmelegítési hőmérsékletének meghatározása*. In: A hegesztés anyagismerete és a hegesztéstechnológia alapjai. Budapesti Műszaki Egyetem Mérnöki Továbbképző Intézet, Budapest, 1995. 64–68.



ISSN 2601 - 1883



9 772601 188012